Thermal Expansion and Magnetostriction of the Partially Frustrated Heavy-Fermion Metal $CePd_{1-x}Ni_xAl$ at Low Temperatures

Zur Erlangung des akademischen Grades eines

DOKTORS DER NATURWISSENSCHAFTEN (Dr. rer. nat.)

von der KIT-Fakultät für Physik des
Karlsruher Instituts für Technologie (KIT)

genehmigte

DISSERTATION

von

M. Sc. Sebastian Kuntz
aus Pirmasens

Tag der mündlichen Prüfung: 21.12.2018

Referent: Prof. Dr. H. v. Löhneysen
Korreferent: Prof. Dr. M. Le Tacon

Contents

Chapter 1

Introduction

In solid state physics the Fermi-liquid theory is one of the most important concepts to describe the nature of correlated many-body fermion systems. It not only explains the behavior of simple metals, like copper or gold, at low temperatures correctly, but also more complicated systems as $CePd_2Si_2$ [1] or $CeCu_5Au$ [2]. In the latter, the interplay between the local Kondo effect [3] and the intersite Ruderman-Kittel-Kasuya-Yosida (RKKY) interaction [4, 5, 6] leads to the development of a so-called heavy-fermion liquid formed by strongly correlated quasiparticles with an extremely enhanced effective mass. As different scenarios can lead to deviations from the predictions of the Fermi-liquid theory and create exotic new states of matter, e.g., the high-temperature superconductivity in cuprates [7] and iron-based [8] superconductors or multiple quantum phase transitions in $CeCu_{6-x}Au_x$ [9], they have become of great interest in the field of strongly correlated electron systems.
In many of these materials competing interactions lead to magnetic ground states that can be tuned through continuous zero-temperature phase transitions by non-thermal control parameters like pressure or magnetic field. Close to these so-called quantum phase transitions quantum fluctuations dominate the system on all length and time scales leading to an accumulation of entropy and deviations from the Fermi-liquid theory in the critical regime above the so-called quantum critical point (QCP) at $T = 0$, the point in phase space, where the transition actually occurs.
Another possibility to achieve deviations from the Fermi-liquid behavior is to introduce frustration to magnetic systems. If the constraints acting on the magnetic system by competing interactions cannot be simultaneously satisfied, magnetic order is prevented by strongly fluctuating correlated moments with an extremely enhanced ground state entropy [10]. This situation of highly correlated moments leads to exotic new states of matter as fluid-like spin liquids [11, 10], spin glasses [12], or spin ice [13].

CePdAl is one of the scarce examples combining the physics of a magnetic heavy-fermion metal with the properties of a geometrically frustrated spin system [14, 15, 16]. In this compound, the Ising-like nearly localized cerium $4f$ moments occupy the corners of equilateral triangles arranged in a distorted kagome lattice, rendering them frustrated. Though this hinders one third of them to participate in the antiferromagnetic order below $T_N = 2.7\,\mathrm{K}$, thermodynamic measurements have found no clue of an enhanced ground state entropy at lowest temperatures indicative of a classical spin liquid [17, 18]. Hence, this makes CePdAl a promising candidate for a so-called quantum spin liquid, a heavily entangled phase in which the ground-state degeneracy is lifted by quantum fluctuations. As the thermal expansion of a solid is related to the pressure derivative of its entropy, it is an ideal probe to track the evolution of phase transitions at very low temperatures. Together with the magnetostriction, related to the pressure dependence of the magnetization, high-precision dilatometry is a powerful tool to study the thermodynamic properties of any magnetic system.

In this thesis single crystals of $CePd_{1-x}Ni_xAl$ with $x = 0$, 0.05, 0.10, 0.12 and 0.14 are investigated with thermal-expansion, magnetostriction and specific-heat measurements between temperatures $T = 20\,\mathrm{mK}$ and $T = 10\,\mathrm{K}$, and in magnetic fields up to $\mu_0 H = 14\,\mathrm{T}$. We will study in detail the evolution of the interplay between antiferromagnetism, Kondo effect and geometric frustration under chemical, hydrostatic and uniaxial pressure.
In chapter 2 a short introduction to quantum criticality and the interplay between Kondo effect and Ruderman-Kittel-Kasuya-Yosida (RKKY) interaction is given, together with the basic concepts of (geometric) frustration. Moreover the current state of research on CePdAl is summarized.
Chapter 3 gives an overview about thermodynamics of stress and strain and their relation to high-precision dilatometry as thermodynamical probe of different energy scales in $CePd_{1-x}Ni_xAl$. Furthermore, the experimental setup of the dilatometer in a ^{3}He-^{4}He-dilution refrigerator for the data acquisition is explained.
Chapter 4 presents previous results for pure CePdAl together with those of the comprehensive investigations of the present thesis. Besides the evolution of the different antiferromagnetic phases their uniaxial and hydrostatic stress and strain dependences are taken into consideration.
In chapter 5 the evolution and suppression of the magnetic order by increasing Ni substitution is investigated.
Chapter 6 compares the results of all investigated samples and discusses the effect of magnetic field, chemical pressure and disorder induced by Ni substitution as well as the uniaxial pressure behavior on the criticality at zero field and close to the respective critical fields.
Chapter 7 will give a conclusion of the results together with a short summary.

Chapter 2

Background

2.1 Quantum Criticality

Phase transitions separate different macroscopic states of matter in the phase space from each other. In condensed matter, they generally appear in dependence of external control parameters as temperature T, pressure p, magnetic field H, or chemical composition. They are classified by the lowest derivative of the thermodynamic potential that is discontinuous at the transition. At second order or continuous phase transitions thermodynamic quantities as the entropy S, volume V or magnetization M exhibit a continuous change. If they occur at finite temperatures, the macroscopic order is destroyed by thermal fluctuations, which show – due to the diverging coherence length – classical critical behavior. In addition to temperature, the macroscopic order can also be suppressed by non-thermal control parameters (see figure 2.1). At the point where the transition temperature T_c reaches zero, the transition is driven by quantum fluctuations, having their origin in the Heisenberg uncertainty principle. At a second-order transition the correlation length ξ and correlation time τ are infinite and fluctuations dominate on all length and time scales. At any finite T_c, the quantum energy of a fluctuation, $E_q = \hbar/\tau$ becomes negligible compared to the thermal energy $E = k_\mathrm{B} \cdot T_c$ because of critical slowing down. When the system is tuned to $T_c = 0$, however, $E_q > k_\mathrm{B} \cdot T_c$ is obeyed for longer and longer times as T is reduced towards zero. The system becomes scale-invariant in both space and time [19]. Although quantum-critical points (QCPs) strictly occur at zero temperature, outside any possible experimental observation, the impact of these fluctuations fundamentally change the behavior at finite temperatures. In this quantum critical regime, metals exhibit strong deviations from the usually expected Fermi-liquid (FL) behavior. In discontinuous or first-order transitions the evolution of critical fluctuations is disrupted due to the sudden onset of long-range order.

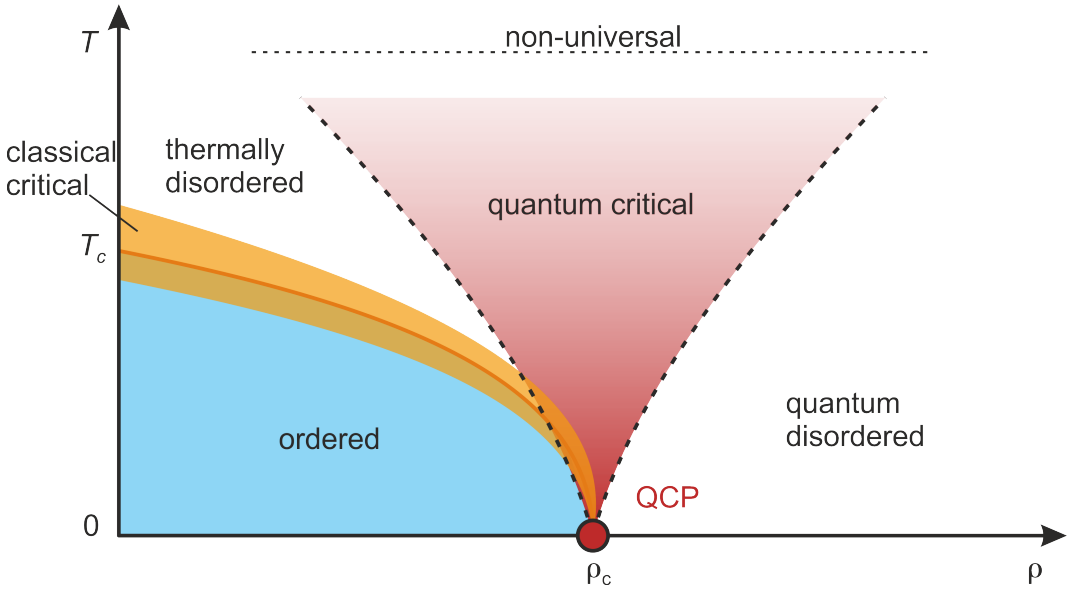

Figure 2.1: Phase diagram close to a quantum critical point (QCP) as a function of temperature T and a non-thermal control parameter ρ. The phase boundary separates a long-range ordered state for $\rho < \rho_c$ from a thermally disordered phase. At finite temperatures the boundary is accompanied by classical critical fluctuations (orange region). With decreasing transition temperature T_c, the ordered phase disappears at $\rho = \rho_c$. As at $T_c \to 0$, the phase transition is mainly driven by quantum fluctuations, the onset of the phase boundary is called quantum-critical point (QCP). At higher temperatures above the QCP a wide phase space is characterized by an unconventional critical behavior. This quantum critical regime gives rise to unusual physical properties which are the topic of this work (reproduced from [20]).

From a thermodynamic point of view, QCPs are characterized by degenerate ground states giving rise to an accumulation of entropy at very low but finite temperatures [21, 22]. The resulting high instability renders these systems particularly sensitive to small changes of the control parameters, disorder, or the formation of new ordered states. In fact, the strongly increased number of degrees of freedom combined with the appearance of quantum-critical fluctuations are believed to be the origin of many unusual phases. The unconventional superconductors found in the vicinity of magnetically ordered states are prominent examples (see figure 2.2).

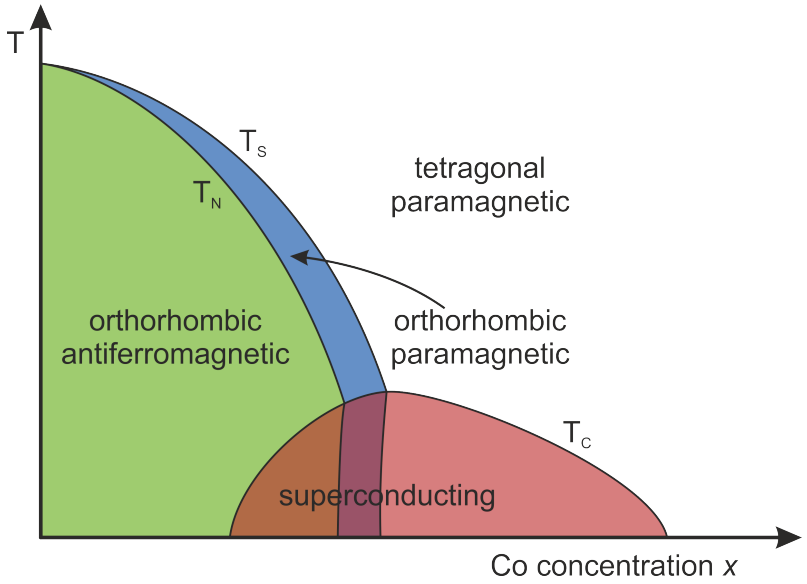

Figure 2.2: Schematic phase diagram of the unconventional superconductor $Ba(Fe_{1-x}Co_x)_2As_2$. By substitution of Fe by Co as non-thermal control parameter the antiferromagnetic order can be suppressed. The presumed QCP is shielded by a dome-shaped superconducting phase with an usually high transition temperature. As its maximum is located close to the extrapolated endpoint of the antiferromagnetic phase it is generally assumed that the related quantum-critical fluctuations and the accumulated entropy are the source of the unconventional superconductivity (reproduced from [23]).

2.1.1 Kondo Effect and RKKY Interaction

Prominent examples for quantum criticality can be found among heavy-fermion systems. These systems consist of $4f$ or $5f$ elements which form a periodic lattice immersed into a metallic matrix. Here, the local Kondo interaction between the f electrons and the conduction band leads to a screening of the magnetic moments of the f electrons while the Ruderman-Kittel-Kasuya-Yosida (RKKY) interaction between the f moments favors long-range magnetic order. As the f electron clouds behave as periodic scattering centers for the conduction electrons, a Fermi liquid develops at low temperature with strongly correlated, heavy quasiparticles. The balance between Kondo and RKKY interaction determines the ground state of these systems. A first qualitative understanding of this behavior was given by Doniach [24] in his famous diagram of the Kondo and RKKY energy scales T_{K} and T_{RKKY} (see figure 2.3). Kondo and RKKY interactions depend on the strength of the exchange interaction J between local moments and conduction electrons and the (unrenormalized) density of states at the Fermi level $N(E_{\mathrm{F}})$:

$$T_{\mathrm{K}} \propto e^{-\frac{1}{J \cdot N(E_{\mathrm{F}})}} \qquad \text{and} \qquad T_{\mathrm{RKKY}} \propto J^2 \cdot N(E_{\mathrm{F}}) \tag{2.1}$$

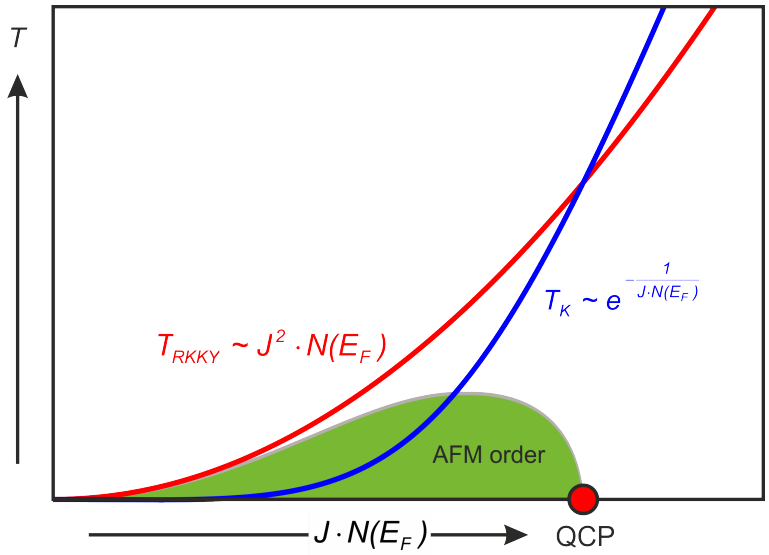

Figure 2.3: Doniach's diagram of heavy-fermion systems. The exchange interaction J and $N(E_{\mathrm{F}})$ strongly depend on the unit-cell volume. At small $J \cdot N(E_{\mathrm{F}})$ the RKKY interaction dominates and the system adopts a magnetic ground state. Due to the exponential increase of the Kondo temperature with increasing $J \cdot N(E_{\mathrm{F}})$, T_{K} exceeds T_{RKKY} and the screening of the magnetic moments suppresses the long-range magnetic order. At the quantum critical point, both ground states are of the same energy and the entropy of the system is strongly enhanced at finite but low temperatures.

As the energy scale of the Kondo effect, the Kondo temperature T_K, exhibits an exponential dependence, the RKKY interaction dominates at small $J \cdot N(E_F)$ and a long-range magnetic order develops. With increasing $J \cdot N(E_F)$, however, T_K becomes larger than T_{RKKY} and the system forms a paramagnetic heavy-Fermi liquid (Kondo-lattice state). Both energy scales can easily be controlled by tiny changes of the unit-cell volume by applying moderate pressures. To avoid the experimental constraints of pressure cells or to apply negative pressure the crystal volume is often changed by replacing atoms of the metallic matrix with smaller or larger isoelectronic elements. The application of this chemical pressure introduces, however, site disorder and might therefore change the physical properties. As in the heavy-fermion compounds different phases occur in a narrow pressure and temperature range, these systems have become a showcase for the investigation of quantum-critical behavior.

2.1.2 Geometric Frustration

A physical system is called frustrated if not all constraints imposed by different kinds of interactions can be equally satisfied and hence their contributions to the potential energy cannot be simultaneously minimized. As a consequence it can adopt a manifold of different degenerate ground states leading to a strongly enhanced entropy [25]. The frustration hinders the system to undergo a transition to a long-range ordered state [20]. In this sense, such systems can be regarded as being located at a quantum-critical point. If the magnetic moments in these systems are large and not Ising-like, classical thermal fluctuations dominate and their high entropy is frozen in at low temperatures. In Ising-like systems, on the other hand, the quantum fluctuations at low temperatures allow these systems to avoid the instability by the emergence of a new highly entangled phase, the so-called *quantum-spin liquid* [10]. Here, the quantum fluctuations lift the ground-state degeneracy by developing unusual ground states. [20].

There exist different routes that lead to frustration, the best known is the geometric frustration. A simplified model for such a system is the equilateral triangle of three antiferromagnetically (AF) coupled Ising spins (see fig. 2.4). The AF coupling between the spins leads to a sixfold degenerate ground state, as not all of the three spins can be simultaneously aligned antiparallelly to each other.

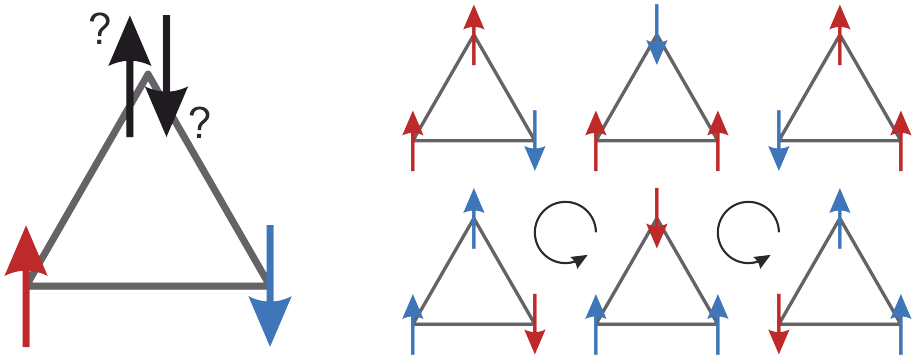

Figure 2.4: Frustration on an equilateral triangular lattice in an antiferromagnetically coupled Ising system. The AF coupling between the spins leads to a sixfold degenerate ground state as not all of the three spins can be antiparallel to each other.

Experimentally, the degree of frustration is usually quantified by the so-called frustration parameter, the ratio between the Curie-Weiss temperature Θ_{CW} and the Néel temperature T_N, $f = |\Theta_{CW}|/T_N$, as it relates the strength of the exchange interaction ($\propto \Theta_{CW}$) to the magnetic ordering temperature T_N. Conventionally, a system is called frustrated, if $f > 5$. A system without any long-range order down to $T = 0$ leads to a divergence of f. The frustration in geometric frustrated materials can be controlled by breaking their crystal symmetry, by polarizing or screening their magnetic moments. Thus pressure or magnetic fields can be used as control parameters to tune these systems away from the QCP.

2.2 CePdAl - a Frustrated Heavy-Fermion Metal

CePdAl is one of the rare examples of a magnetic heavy-fermion (HF) metal with geometric frustration. Usually, the itinerant magnetic order of metals lifts any geometric frustration. In CePdAl, however, the magnetic moments are formed by the nearly localized $4f$ electrons of the Ce ions. Therefore, in addition to the geometric frustration, CePdAl is in close proximity to a magnetic QCP due to the interplay between the Kondo effect and RKKY interaction. CePdAl crystallizes in the ZrNiAl structure (space group $P\bar{6}2m$) with the cerium atoms occupying the Zr sites in a distorted kagome lattice in the hexagonal ab plane (see figure 2.5) [14, 15, 16]. While the Ce and Al sites are crystallographically equivalent, Pd occupies two different sites forming alternating Ce-Pd and Al-Pd layers.

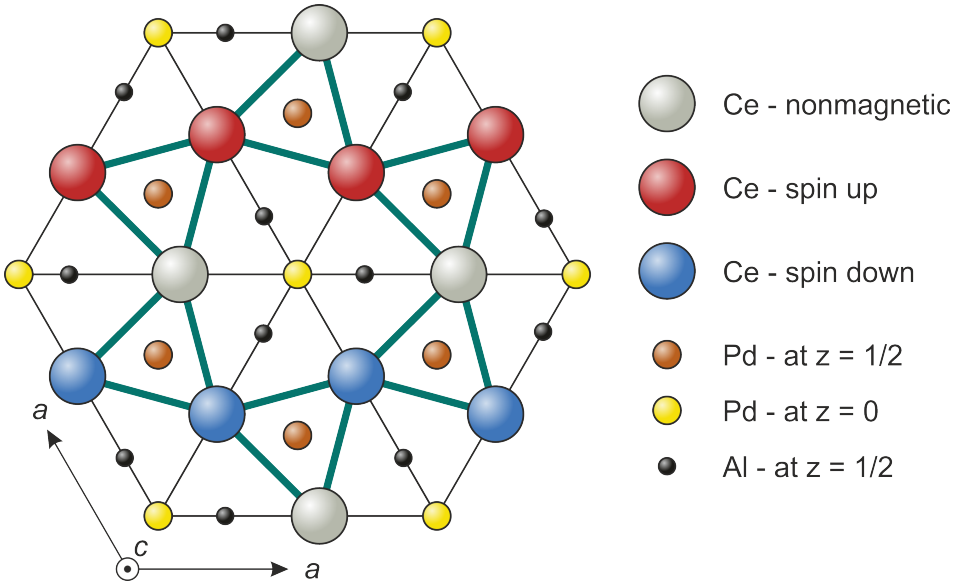

Figure 2.5: Schematic view of the *ab* plane of the ZrNiAl structure in CePdAl. The big spheres indicate the positions of the cerium atoms in a distorted kagome lattice (bold green lines). There exist two crystallographically inequivalent Pd sites (medium-sized spheres) with the yellow Pd atoms in the Ce plane at $z = 0$ and the orange Pd atoms in z direction between the Ce planes at $z = 1/2$. The small black spheres represent the Al sites at $z = 1/2$. In the partial magnetic order the magnetic Cerium atoms (red spheres for spin up, blue spheres for spin down) form corrugated chains in the *ab* plane that are separated by geometrically frustrated cerium atoms (grey spheres).

CePdAl orders antiferromagnetically at the Néel temperature $T_N \approx 2.7\,\mathrm{K}$. The magnetic structure was determined in detail by neutron diffraction measurements on single and polycrystals [16, 26, 27]. Below T_N, two-thirds of the Cerium moments form sine-like modulated antiferromagnetic chains along the c axis that are ferromagnetically coupled to the next nearest chains along the a axis. The resulting corrugated ac planes are separated from each other by planes of the remaining magnetic moments that do not participate in the long-range magnetic order. Neutron diffraction as well as ^{27}Al NMR measurements show that these one-third of the magnetic moments are frustrated down to at least 30 mK [16, 28]. The antiferromagnetic order is incommensurate along the c axis with an ordering vector of $Q_{AF} \approx (0.5\ 0\ \tau)$ and $\tau \approx 0.354$ at T_N. Presumably due to the frustration, τ is slightly temperature dependent. Below T_N, it decreases with decreasing temperature and locks in at $T \approx 1.9\,\mathrm{K}$ to $\tau \approx 0.351$ [16, 29, 26]. Magnetic-susceptibility measurements show a strong magnetic anisotropy of $\chi_c/\chi_a \approx 15$ at $T = 5\,\mathrm{K}$ that is attributed to crystal-electric-field effects [30]. Thus, CePdAl can be regarded as an effective spin 1/2 Ising system with the easy axis aligned along the c direction (see figure 2.6 for the magnetic structure).

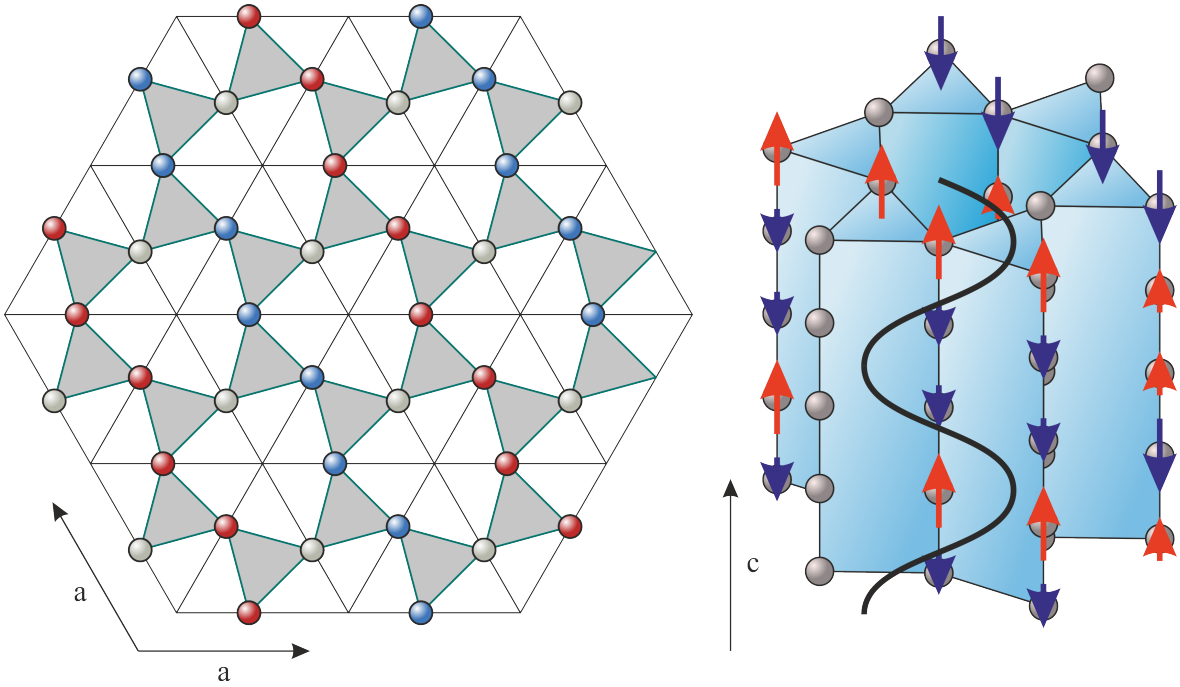

Figure 2.6: Magnetic structure of CePdAl of the *ab* plane and along the *c* direction. Blue spheres and arrows indicate magnetic moments with spin down (parallel to the *c* direction), red spheres and arrows moments with spin up. Grey spheres do not participate in the magnetic order. The sine wave along the *c* direction represents the modulation τ of the magnetic ordering vector. For simplicity in this schematic representation its value was set to $\tau = 1/3$ though the magnetic order is incommensurate along the *c* axis.

Núñez-Regueiro *et al.* have derived a theoretical model to explain the magnetic structure in CePdAl that includes the competition between Kondo screening and short-range exchange interaction [31]. In their work, they consider nearest-neighbor interaction J_1 and next-nearest neighbor interaction J_2 between the cerium magnetic moments in the *ab* plane. The Hamiltonian then yields

$$H = \sum_i \Delta_i(T)|\mu_i|^2 - \frac{1}{2}\sum_{i \neq j} J_{ij}\vec{\mu}_i\vec{\mu}_j \tag{2.2}$$

with the energy difference $\Delta_i(T)$ between the Ce Kondo state with $\mu_i = 0$ and the magnetic state with $\mu_i \neq 0$. Figure 2.7 shows the assumed interactions and the resulting phase diagram. For a certain configuration set of exchange interaction strengths J_1 and J_2 they were able to derive the experimentally observed magnetic structure of CePdAl [31].

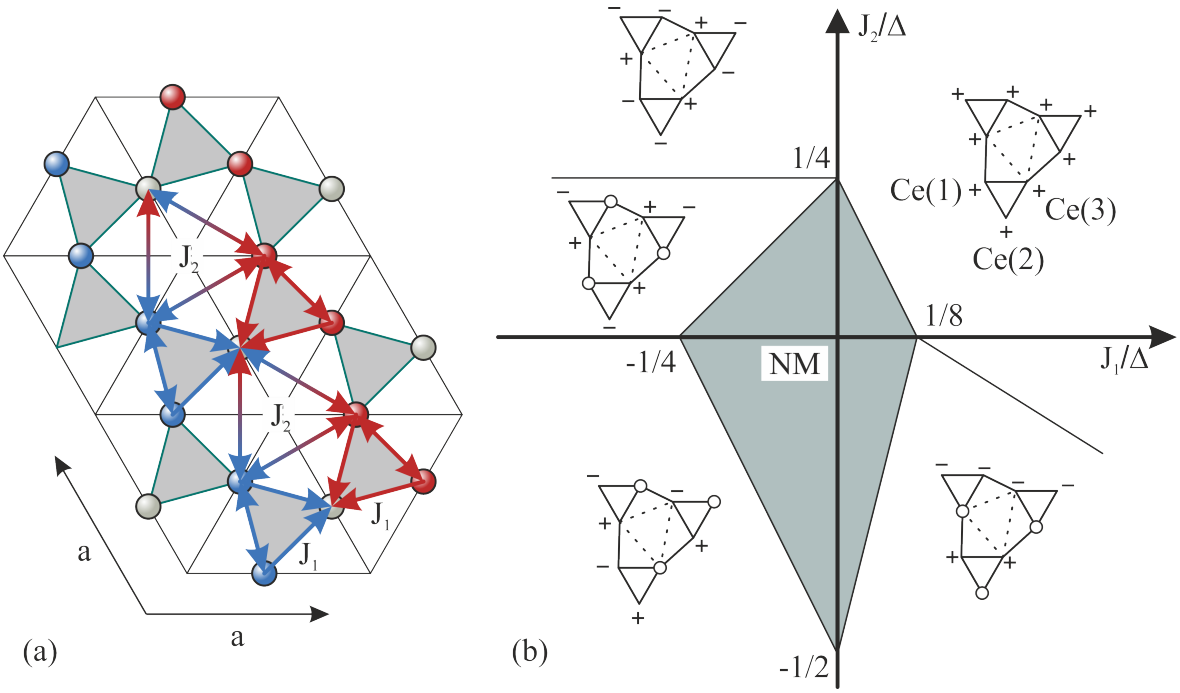

Figure 2.7: Theoretical model (a) and phase diagram (b) for the magnetic structure of CePdAl by Núñez-Regueiro *et al.* [31].
(a) The exchange interactions J_1 between nearest-neighbor Ce ions are ferromagentic and those between the next-nearest-neighbor Ce ions J_2 are antiferromagnetic. The equally strong interactions lead to frustration of one third of the Ce moments (grey). Red spheres represent spin up, blue spheres spin down. (b) Phase diagram for the magnetic structure as a function of J_1/Δ and J_2/Δ. The grey area indicates a paramagnetic Kondo state. The observed magnetic structure is derived for the parameter set in the lower right panel. Reproduced from [31].

Apart from the unusual magnetic order, CePdAl exhibits the typical properties of HF systems. Measurements of the electronic specific heat reveal an enhanced Sommerfeld coefficient of $\gamma \approx 270\,\mathrm{mJ/mol\,K^2}$ which is typical for moderate HF compounds [14]. Resistivity measurements show a logarithmic increase of the resistivity towards lower temperatures and an extremum of the thermopower which are both hallmarks for a pronounced Kondo effect. The Kondo temperature obtained from the temperature dependence of the entropy amounts to $T_\mathrm{K} \approx 6\,\mathrm{K}$ [14, 15].

As in other HF compounds, the antiferromagnetic order can be suppressed by magnetic fields and pressure. By applying a magnetic field parallel to the easy axis, CePdAl exhibits several metamagnetic phase transitions before at $\mu_0 H \approx 4\,\mathrm{T}$ the long-range magnetic order vanishes and the system enters the paramagnetic field-polarized Fermi-

liquid state [17, 32, 18, 33]. While the magnetic field weakens both the AF order as well as the Kondo effect, pressure can be used to change the balance between Kondo and RKKY interaction. Measurements under quasi-hydrostatic pressure indicate that CePdAl can be tuned to the magnetic QCP at a critical pressure of roughly $p_c \approx 1\,\mathrm{GPa}$ [34, 35, 36]. In a similar way, chemical pressure was used to reach this QCP by replacing Pd by isovalent but smaller Ni ions. In $CePd_{1-x}Ni_xAl$, the magnetic ordering temperature T_N decreases linearly with the Ni concentration x up to a concentration of about $x \approx 0.14$ where the magnetic order vanishes and non-Fermi-liquid (nFL) behavior was observed [17, 37]. Along the substitution series the crystal structure of $CePd_{1-x}Ni_xAl$ does not change and the lattice constants decrease linearly with increasing Ni content for $0 \leq x \leq 0.16$ [38].

CePdAl offers the unique possibility to study in detail the interplay between geometric frustration and the competition between Kondo and RKKY interaction. These two approaches give two fundamental different routes towards quantum criticality. The geometric frustration is based on frustrated magnetic interactions between well-localized moments in a specific crystal symmetry, whereas the Kondo effect is a local interaction that tends to delocalize and "switch off" the magnetic moments.

Recently, it was suggested that the abundance of quantum fluctuations caused, e. g., by magnetic frustration, has to be considered to drive strongly correlated HF systems such as $CeCu_{6-x}Au_x$ and $YbRh_2Si_2$ towards a QCP. This has led to an extended Doniach diagram in which the frustration appears as a second tuning parameter [20, 39, 40, 41, 42]. Although different theoretical versions of this global phase diagram of HF systems have been published there are only very few systems which allow to address this topic from an experimental side. In fact, CePdAl is the only example of a HF system where a geometric frustration could unambiguously be identified. The methods discussed in this work will include structural control parameters as hydrostatic and uniaxial pressure as well as chemical pressure and chemical site disorder. In addition magnetic fields have been used to lift the frustration and to suppress the magnetic order and the Kondo effect.

Chapter 3

Methods

3.1 Dilatometry

3.1.1 On Stress and Strain

The stress on a surface element δA of a body generated by an external force $\vec{p}\delta A$ can be described in terms of a second-rank tensor, the so called *stress tensor* $\boldsymbol{\sigma}$. If $\vec{l}$ is the unit vector perpendicular to the surface element at a certain point, then, as $\delta A \to 0$, $\boldsymbol{\sigma}$ gives the stress at that point with the components

$$p_i = \sigma_{ij} l_i \qquad (i, j = 1, 2, 3). \tag{3.1}$$

Considering a cube with edges along the axes of a Cartesian coordinate system, the components of $\boldsymbol{\sigma}$ with $i = j$ correspond to the normal forces acting on the cube's faces and are called *uniaxial pressures*. The components with $i \neq j$ are the shear components and are called *simple shear stresses* [43]. Generally, stresses are classified in uniaxial and biaxial stresses, and hydrostatic pressure. A specific subset of the biaxial stresses are the *pure shear stresses*. In contrast to the simple shear stresses, they are only produced by a combination of normal stress components. Pure shear stresses are linearly independent of the hydrostatic pressure. For a homogenous material the application of a pure shear stress leads to a deformation without a change of the volume provided that the compressibility is isotropic. For a continuum they are, apart from a rotation, equivalent to simple shear stresses. In the following, examples of the different stress are given in terms of the stress tensor $\boldsymbol{\sigma}$ and illustrated in figure 3.1.

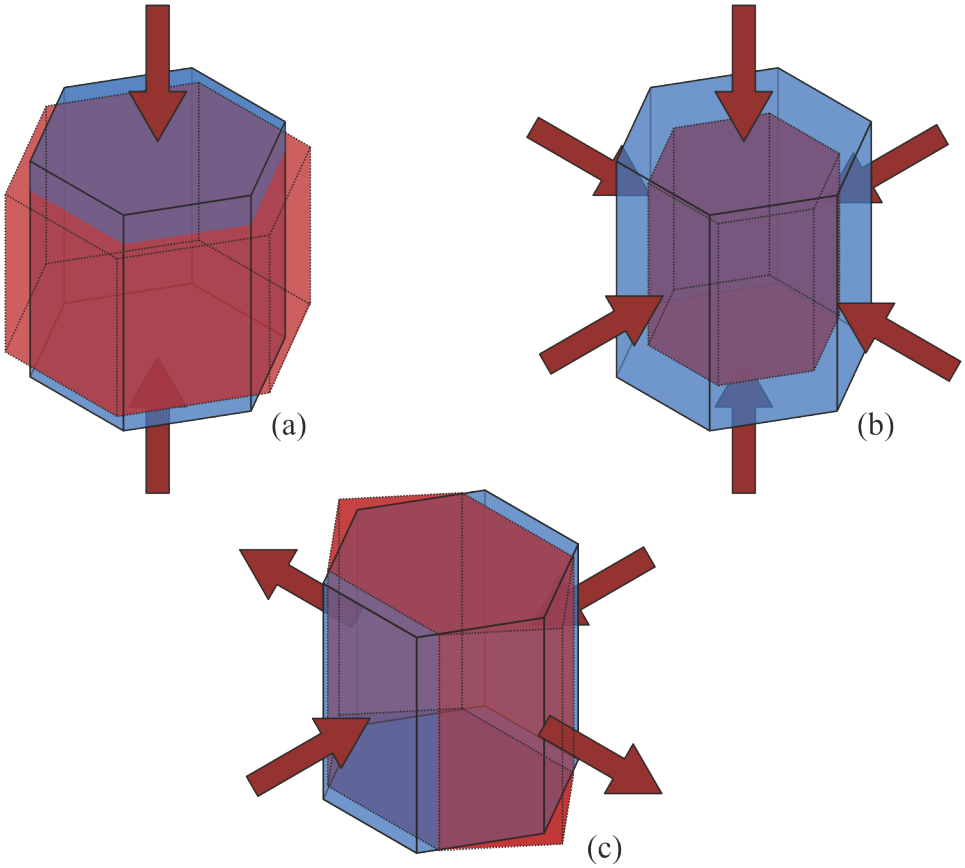

Figure 3.1: (a)-(c): Visual representations of different stresses. (a) shows uniaxial pressure along the z-direction of a Cartesian coordinate system. Due to the Poisson effect the body is deformed in all directions. (b) illustrates the effect of hydrostatic pressure, where the absolute values along all directions are the same, the resulting distortion can be different. (c) shows a particular case of pure shear stress. Despite the distortion, the volume of the hexagon is approximately conserved. This is an important difference to uniaxial pressure shown in (a).

- Uniaxial stress:

$$\boldsymbol{\sigma} = \begin{pmatrix} \sigma_{11} & 0 & 0 \\ 0 & 0 & 0 \\ 0 & 0 & 0 \end{pmatrix} \quad \text{or} \quad \boldsymbol{\sigma} = \begin{pmatrix} 0 & 0 & 0 \\ 0 & \sigma_{22} & 0 \\ 0 & 0 & 0 \end{pmatrix} \quad \text{or} \quad \boldsymbol{\sigma} = \begin{pmatrix} 0 & 0 & 0 \\ 0 & 0 & 0 \\ 0 & 0 & \sigma_{33} \end{pmatrix} \tag{3.2}$$

- Biaxial stress:

$$\boldsymbol{\sigma} = \begin{pmatrix} \sigma_{11} & 0 & 0 \\ 0 & \sigma_{22} & 0 \\ 0 & 0 & 0 \end{pmatrix} \quad \text{or} \quad \boldsymbol{\sigma} = \begin{pmatrix} 0 & 0 & 0 \\ 0 & \sigma_{22} & 0 \\ 0 & 0 & \sigma_{33} \end{pmatrix} \quad \text{or} \quad \boldsymbol{\sigma} = \begin{pmatrix} \sigma_{11} & 0 & 0 \\ 0 & 0 & 0 \\ 0 & 0 & \sigma_{33} \end{pmatrix} \tag{3.3}$$

- hydrostatic pressure:

$$\boldsymbol{\sigma} = \begin{pmatrix} -\sigma & 0 & 0 \\ 0 & -\sigma & 0 \\ 0 & 0 & -\sigma \end{pmatrix} \tag{3.4}$$

- pure shear stress:

$$\boldsymbol{\sigma} = \begin{pmatrix} -\sigma & 0 & 0 \\ 0 & \sigma & 0 \\ 0 & 0 & 0 \end{pmatrix} \quad \text{or} \quad \boldsymbol{\sigma} = \begin{pmatrix} 0 & 0 & 0 \\ 0 & -\sigma & 0 \\ 0 & 0 & \sigma \end{pmatrix} \quad \text{or} \quad \boldsymbol{\sigma} = \begin{pmatrix} \sigma & 0 & 0 \\ 0 & 0 & 0 \\ 0 & 0 & -\sigma \end{pmatrix} \tag{3.5}$$

As stress acts as an external force on the crystal, for a physical interpretation the reaction of the crystal to that force, i. e., the resultant deformation has to be considered. The resulting deformation is usually discussed in terms of the related strain tensor. If a point x_j in a deformed body is displaced by u_i, then one can define the strain as a second-rank tensor $\boldsymbol{e}$ with the components

$$e_{ij} = \frac{\partial u_i}{\partial x_j} \qquad (i, j = 1, 2, 3) \tag{3.6}$$

as a representation of the displacement. The components of $\boldsymbol{e}$ define different kinds of spatial changes:

- e_{ii} represents an expansion per unit length parallel to the i-axis
- e_{ij} represents a rotation about the k-axis towards the i-axis of a line element parallel to the j-axis

The *strain tensor* $\boldsymbol{\epsilon}$ can then be constructed using the elements of $\boldsymbol{e}$.

$$\boldsymbol{\epsilon} = \begin{pmatrix} \epsilon_{11} & \epsilon_{12} & \epsilon_{31} \\ \epsilon_{12} & \epsilon_{22} & \epsilon_{23} \\ \epsilon_{31} & \epsilon_{23} & \epsilon_{33} \end{pmatrix} = \begin{pmatrix} e_{11} & \frac{1}{2}(e_{12} + e_{21}) & \frac{1}{2}(e_{13} + e_{31}) \\ \frac{1}{2}(e_{12} + e_{21}) & e_{22} & \frac{1}{2}(e_{23} + e_{32}) \\ \frac{1}{2}(e_{13} + e_{31}) & \frac{1}{2}(e_{23} + e_{32}) & e_{33} \end{pmatrix} \tag{3.7}$$

The ϵ_{ij} connect the position vector of a point x_j to its displacement u_i induced by strain. The elements on the main axis are called *tensile strains* (when $\epsilon > 0$) or *compressive strains* (when $\epsilon > 0$), the other ones *shear strains* [43]. Special cases, as uniaxial pressure, hydrostatic pressure, etc., shown for the stress tensor can equivalently be applied to the strain tensor. Both stress and strain tensors are not crystal properties themselves, therefore they do not have to be conform to the crystal symmetry as long as they are generated by external forces.

3.1.2 Dilatometry as Thermodynamic Probe

As temperature changes, any solid undergoes a characteristic volume change whose determination is a powerful tool to gain insight into the pressure dependence of thermodynamic properties. The volume thermal expansion coefficient α_{V} is defined as the relative change of the system's volume V with temperature T at constant pressure p

$$\alpha_V = \frac{1}{V}\left(\frac{\mathrm{d}V}{\mathrm{d}T}\right)_p . \tag{3.8}$$

In anisotropic systems, the thermal expansion differs along the different crystallographic directions, wherefore α_V is usually replaced by the linear thermal-expansion coefficients

$$\alpha_{ij} = \frac{\partial \epsilon_{ij}}{\partial T} \tag{3.9}$$

as derivatives of the strain tensor $\boldsymbol{\epsilon}$ with respect to temperature. As $\boldsymbol{\epsilon}$ is the aforementioned symmetrical second-rank tensor, this also holds for $\boldsymbol{\alpha}$. Notably, since the temperature T is a scalar, the thermal expansion cannot break the crystal-lattice symmetry. In contrast to the strain generated by external pressure, the strain produced by thermal excitations has to be conform with the crystal symmetry (Neumann's Principle) [43]. As a result the number of independent α_{ij} is limited. In the case of a hexagonal crystal symmetry, that underlies all samples covered in this work, only two of the coefficients are independent. $\boldsymbol{\alpha}$ then changes to

$$\boldsymbol{\alpha}_{\mathrm{hex}} = \begin{pmatrix} \alpha_a & 0 & 0 \\ 0 & \alpha_a & 0 \\ 0 & 0 & \alpha_c \end{pmatrix} \tag{3.10}$$

with a and c denoting the hexagonal lattice parameters. As the infinitesimal volume strain, produced by thermal expansion, is equal to the trace of the strain tensor ($\epsilon_V = \mathrm{d}V/V = \mathrm{Tr}(\epsilon_{ij}) = \epsilon_a + \epsilon_a + \epsilon_c = 2\epsilon_a + \epsilon_c$), the volume-thermal expansion coefficient for a hexagonal crystal symmetry becomes

$$\alpha_V = \frac{\partial \epsilon_V}{\partial T} = \mathrm{Tr}(\alpha_{ij}) . \tag{3.11}$$

Length changes of a crystal are related to their thermodynamic potential by the elastic energy. As they tend to minimize the Gibbs free energy $G(p,T) = U + pV - TS - \mu_0 HM$, any physical property originating, e.g., from lattice vibrations, itinerant electrons, magnetic ions, etc., can be probed by measuring the related volume or length changes. At constant pressure, an infinitesimal change of G is given by

$$\mathrm{d}G = -S\mathrm{d}T + V\sum_{\lambda} \epsilon_\lambda \sigma_\lambda \quad \text{with } \lambda = i,j \tag{3.12}$$

with the external stress σ_{ij} conjugated to the internal strain ϵ_{ij}. The second term describes changes of the elastic energy. By using the Maxwell relation for pressure and temperature

$$\frac{\partial^2 G}{\partial T \partial p} = -\left(\frac{\partial S}{\partial p}\right)_T = \left(\frac{\partial V}{\partial T}\right)_p \tag{3.13}$$

on the Gibbs free energy, one can relate the thermal expansion coefficients α_{ij} to the stress dependence of the entropy S in their direction:

$$\alpha_{ij} = \frac{1}{V}\frac{\partial^2 G}{\partial T \partial \sigma_{ij}} = -\frac{1}{V}\frac{\partial S}{\partial \sigma_{ij}}\,. \tag{3.14}$$

Hence, this allows to probe any change in any physical quantity that contributes to a system's entropy and is sensitive to uniaxial pressure. The uniaxial pressures span a Cartesian coordinate system. Therefore, the total entropy can be calculated by summing over all contributions:

$$\mathrm{d}S = \sum_{\lambda} \frac{\partial S}{\partial \sigma_i}\mathrm{d}\sigma_i\,. \tag{3.15}$$

By considering this sum as the scalar product between $\mathrm{d}\vec{\sigma}$ and the entropy's gradient $\vec{\nabla} = (\partial S/\partial\sigma_1, \partial S/\partial\sigma_2, \partial S/\partial\sigma_3)$ one can determine the entropy's stress dependence along a unit vector $\hat{u}$:

$$\frac{\partial S}{\partial \vec{\sigma}_u} = \vec{\nabla} S\hat{u} = \sum_{i=1}^{3} \frac{\partial S}{\partial \sigma_i}\hat{u}_i = -V\sum_{i=1}^{3} \alpha_i \hat{u}_i\,. \tag{3.16}$$

On the one hand, this provides the possibility to determine the change in the entropy $\partial S/\partial\vec{\sigma}_u$ for arbitrary combinations of uniaxial pressures. On the other hand, it yields the combination of uniaxial pressures leading to the steepest increase of the entropy at a given configuration. As the entropy at finite, albeit arbitrarily low temperatures becomes maximal at a QCP this can be used to find the optimal stress combination to tune the system towards the QCP.

Similar to the thermal expansion, a change of the applied magnetic field can lead to a dilatation of a crystal. As all main interactions between the atomic magnetic moments (e.g., exchange, or dipole-dipole interactions) depend strongly on atomic distances, the expansion of a magnetic system is strongly affected by its magnetic state [44]. In compounds with magnetically ordered moments the magnetic interaction energy adds to the total free energy of the system and causes magnetic stress. This stress can be considered similarly to the one created by thermal excitations, with the difference that it additionally depends on the magnetic-field direction. In contrast to the

temperature, the magnetic field is able to break the crystal symmetry. Therefore, the magnetostriction coefficient is not a second-rank but a third-rank tensor connecting the absolute value and direction of the applied magnetic field to the dilatation of the crystal:

$$\lambda_{ijk} = \left(\frac{\partial \sigma_{ij}}{\partial(\mu_0 H_k)} \right)_{p,T} . \tag{3.17}$$

Analogously to the thermal expansion, the magnetostriction is a second order derivative of the Gibbs free energy G. Again using the Maxwell relations, one can relate the magnetostriction coefficient λ_{ijk} at constant pressure p and temperature T to the pressure dependence of the magnetization at constant temperature T and magnetic field H:

$$\frac{\partial^2 G}{\partial(\mu_0 H)\partial p} = -\left(\frac{\partial M}{\partial p} \right)_{(T,H)} = \left(\frac{\partial V}{\partial(\mu_0 H)} \right)_{(T,p)} \tag{3.18}$$

$$\lambda_{ijk} = \frac{1}{V} \left(\frac{\partial^2 G}{\partial \sigma_{ij} \partial(\mu_0 H_k)} \right)_T = -\frac{1}{V} \left(\frac{\partial M}{\partial \sigma_{ij}} \right)_{(T,H_k)} \tag{3.19}$$

In order to obtain a more convenient expression of the thermal expansion and magnetostriction, the strain tensors are simplified by a principal-axis transformation and the subscripts $i = j$ are abbreviated with i (Voigt notation). The direction of the magnetic field is omitted and stated in the accompanying text. In conclusion, one obtains the following expressions:

$$\textbf{thermal expansion}: \qquad \alpha_i = \frac{1}{L_i} \left(\frac{\partial L_i}{\partial T} \right)_{(\boldsymbol{\sigma},H)} = -\frac{1}{V} \left(\frac{\partial S}{\partial \sigma_i} \right)_{(T,H)} \tag{3.20}$$

$$\textbf{magnetostriction}: \qquad \lambda_i = \frac{1}{L_i} \left(\frac{\partial L_i}{\partial(\mu_0 H)} \right)_{(\boldsymbol{\sigma},T)} = -\frac{1}{V} \left(\frac{\partial M}{\partial \sigma_i} \right)_{(T,H)} \tag{3.21}$$

If the temperature is decreased towards zero, the thermal expansion vanishes because the entropy has to approach zero due to the third law of thermodynamics. Likewise, the magnetostriction becomes constant because:

$$\frac{\partial \lambda_i}{\partial T} \propto \frac{\partial^2 S}{\partial(\mu_0 H)\partial \sigma_i}. \tag{3.22}$$

In addition, the magnetostriction disappears at zero magnetic field if the magnetization vanishes at $H \to 0$. Consequently, the measurement of the thermal expansion and magnetostriction at very low temperatures and small magnetic fields requires an extremely high resolution.

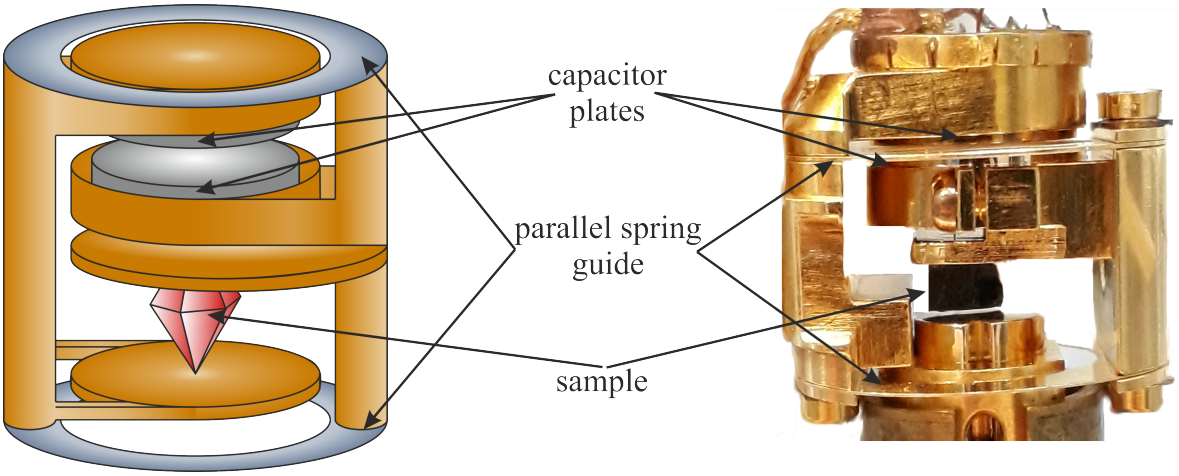

Figure 3.2: Schematic sketch and photograph of the used dilatometer. A change of the sample length moves the right side and lower capacitor plate of the dilatometer up or down. The two annular springs ensure a parallel translation of the capacitor plates. The dilatation is in this way directly transferred to the distance d between the two plates and the capacitance changes as $C \propto \frac{1}{d} \propto \frac{1}{\Delta L}$.

The state-of-the-art technique to monitor such tiny length changes is the high-precision capacitance dilatometry where the expansion or contraction ΔL of a sample is directly transferred to the distance d between two capacitor plates and therefore directly related to the capacitance C. To realize this experimentally, the sample is clamped between a fixed piston and a movable capacitor plate, which is mounted to a parallel-spring suspension. This parallel-spring guide is needed to keep the capacitor plates parallel to each other and enable hereby small distances between the plates without touching. In addition, the springs ensure a nearly frictionless movement of the plate. At low temperatures the thermal expansion of the dilatometer itself is very small and the measurements can easily be calibrated by it. The length change ΔL of the sample then is given by

$$\Delta L = -\Delta d = -\epsilon_0 \epsilon_r \frac{A}{\Delta C} \tag{3.23}$$

with ϵ_0 being the vacuum permittivity, ϵ_r the medium's permittivity, and A the size of the capacitor's plates. Since C is proportional to d^{-1}, the resolution increases with decreasing d. As in our temperature range the relative length changes $\Delta L/L$ are far below 10^{-3} we normalize the absolute length change by a fixed sample length $L_{(0,i)}$, usually taken at room temperature. The dilatometer and springs used for this work [see fig. 3.2] are made from a gilded 98 %-copper 2 %−beryllium alloy (Cu:Be), which results in a good compromise between elasticity and stability and is nonmagnetic down to lowest temperatures. Due to its compact design it can be tilted with respect to the magnetic-field direction which allows measurements of the thermal expansion or magne-

tostriction parallel or perpendicular to the applied field. As mentioned previously, the resolution increases by choosing a small distance between the capacitor plates, wherefore the plates have to be evenly polished and aligned as parallel as possible. With a gap of $d \approx 20\,\mu$m we typically achieve a resolution of $\Delta L \approx 10^{-13}\,$m or $\Delta L/L \approx 10^{-10}$ for sample sizes of about 1 mm. The sample is aligned in the dilatometer with respect to the field direction and is clamped by a small piston, which can be moved to adjust the capacitance at room temperature. It can be fixed by a small screw. By using pistons of different lengths, samples in the range of $\approx 10\,\mu$m up to 10 mm can be measured.

The dilatometer is mounted in an Oxford Instruments MX400 ^{3}He-^{4}He-dilution refrigerator with a superconducting Nb_3Sn magnet, that allows measurements between $T = 10\,$mK and $T = 10\,$K in magnetic fields up to $\mu_0 H = 14\,$T ($\mu_0 H = 16\,$T with lambda-stage). The dilatometer is connected to the mixing chamber by copper-covered glass-fiber plates and positioned in the middle of the magnet. These glass-fiber plates have been dimensioned in such a way that the temperature of the sample can be continuously changed between 20 mK and 3 K without evaporating the ^{3}He-^{4}He mixture. Measurements for $T \geq 3\,$K are performed by removing a part of the mixture from the system to avoid overpressure and to obtain an optimal thermal contact to the $1--$K pot which then provides the necessary cooling power for the experiment. The temperature is measured by a magnetic-field calibrated ruthenium-oxide thermometer chip using a Lakeshore 370 AC resistance bridge in a four-terminal setup. A strain gauge driven by a Keithley 2400 SourceMeter is used as a heater to control the temperature of the experiment. The capacitance is measured in a three-terminal setup by an Andeen–Hagerling AH 2550 capacitance bridge with an applied voltage of $U = 1.5 - 15\,$V with a frequency of $f = 1\,$kHz and an integration time of $t = 9\,$s. The coaxial cables for the capacitance measurements between the $4--$K stage and the mixing chamber are made of a niobium core and a stainless steel shield to minimize the heat input, as superconducting electrons do not transport heat and stainless steel is a bad thermal conductor. Between the mixing chamber and the dilatometer gilded copper coaxial cables are used. The connections for the temperature measurement and heater control between the 4 K–stage and the top of the cryostat are made from twisted pairs of Cu:Be to reduce the heat input and picking-up of electrical noise. They are lead out of the cryostat by PI filters and a shielded outbreak box. Between the $4--$K stage and the mixing chamber superconducting niobium titanium twisted pairs are used. The experiment itself is connected to the mixing chamber via twisted pairs made of copper. As during this work big parts of the wiring were renewed but not changed, a more detailed description is already given in [45].

3.1.3 Grüneisen Ratio as a Hallmark for Quantum Criticality

The Grüneisen ratio Γ is named after Eduard Grüneisen who discovered that the thermal expansion α_i of a solid material divided by its specific heat C is approximately constant [46, 47]. Originally, it was used to estimate the pressure (or volume) dependence of phonon frequencies. More generally, it is defined as the normalized stress dependence of the characteristic energy scale E^*, e.g. $E^*(T_\mathrm{K})$, of a system:

$$\Gamma_{\sigma_i} = \frac{1}{E^*}\frac{\partial E^*}{\partial \sigma_i}. \tag{3.24}$$

Γ is often also related to the strain dependence and then called Grüneisen parameter:

$$\Gamma_{\epsilon_i} = -\frac{1}{E^*}\frac{\partial E^*}{\partial \epsilon_i}. \tag{3.25}$$

If a system is dominated by a single pressure (or strain) dependent characteristic energy scale $E^*(\sigma_i)$, the Grüneisen ratio can be obtained from thermal expansion and specific-heat measurements. In this case, the entropy is given by $S = f[k_B T/E^*(p)]$. According to the Maxwell relations, α_i and C/T are partial derivatives of S to stress and temperature, respectively, and Γ is defined by their ratio:

$$\Gamma_{\sigma_i} = V_m\frac{\alpha_i}{C} = -\left.\frac{\partial S}{\partial \sigma_i}\right|_T \left(T\left.\frac{\partial S}{\partial T}\right|_{\sigma_i}\right)^{-1} = \frac{1}{E^*}\frac{\partial E^*}{\partial \sigma_i} \tag{3.26}$$

$$\Gamma_{\epsilon_i} = V_m\sum_{j=1}^{3} c_{ij}\frac{\alpha_j}{C} \tag{3.27}$$

with c_{ij} being the elastic constants and V_m the molar volume. Γ can also be related to the hydrostatic pressure or volume dependence of E^* by using the isothermal bulk modulus B_T.

$$\Gamma_p = V_m\frac{\alpha_V}{C} \tag{3.28}$$

$$\Gamma_V = V_m B_T \cdot \frac{\alpha_V}{C} \tag{3.29}$$

Although the thermal expansion and specific heat are strongly temperature dependent quantities, the Grüneisen ratio is usually constant if a single E^* dominates. There is, however, one important exception: At a QCP, the characteristic energy scale of the system vanishes by definition and, consequently, Γ diverges when the QCP is approached. In addition, Γ changes its sign if the system is tuned through the QCP by varying a nonthermal control parameter like stress. This sign change and the divergence of Γ are characteristic features of quantum-critical systems and therefore taken as hallmarks of QCPs [48].

If a system is controlled by several characteristic energy scales E_n^* the entropy is the sum over all their contributions $S = \sum S_n(k_B T/E_n^*)$. In this case, the ratio between thermal expansion and specific heat is no longer constant and does not allow to simply determine the individual Grüneisen ratios of the different E_n^*. An exception are continuous phase transition as here the noncritical background can be subtracted with the so-called Ehrenfest relation.

3.1.4 Ehrenfest Relations and Clausius-Clapeyron Equations

The Ehrenfest relations and Clausius-Clapeyron equations allow to estimate the uniaxial stress dependence of second-order and first-order phase transitions, respectively. At second-order phase transitions the entropy and volume of a system continuously change as function of pressure and temperature while their derivatives, e.g., the thermal expansion and the specific heat, reveal abrupt changes. The entropy change can then be written as:

$$\Delta\, S|_{T_c} = 0 = \Delta\, \frac{\partial S}{\partial \sigma_i}\bigg|_{T_c} d\sigma_i + \Delta\, \frac{\partial S}{\partial T}\bigg|_{T_c,\sigma_i} dT. \tag{3.30}$$

Δ stands for the difference between the values just above and below the phase transition temperature T_c. Using again the Maxwell relation, we obtain the Ehrenfest relation [49]:

$$\frac{\mathrm{d}T_c}{\mathrm{d}\sigma_i} = V_m T_c\, \frac{\Delta\alpha_i}{\Delta C}\bigg|_{T_c}. \tag{3.31}$$

This relation is closely related to the Grüneisen ratio. In fact, it can be understood as the Grüneisen ratio of the upcoming low-temperature phase with T_c as characteristic energy scale. Therefore, in a more general way, the Ehrenfest relation can be used to determine the noncritical background even if the transition is characterized by strong, critical fluctuations as shown by Pippard [50].

At a first-order transition the Gibbs free energy remains continuous, but S and V are discontinuous. As a consequence the Ehrenfest relation is no longer applicable, but a similar approach as above can be used to obtain the so-called Clausius-Clapeyron equation of the stress dependence of T_c:

$$\frac{\mathrm{d}T_c}{\mathrm{d}\sigma_i} = V_m \frac{\Delta L_i/L_i}{\Delta S}. \tag{3.32}$$

and if T is replaced by H, the stress dependence of the critical field H_c

$$\frac{\mathrm{d}\mu_0 H_c}{\mathrm{d}\sigma_i} = V_m \frac{\Delta L_i/L_i}{\Delta M}. \tag{3.33}$$

3.2 Samples

The partial antiferromagnetic order in CePdAl can either be suppressed by applying hydrostatic pressure [34, 35, 36] or by substituting palladium by smaller, isovalent nickel ions to introduce chemical pressure [17, 37, 38]. To get insight into the interplay between the geometric frustration and the Kondo effect and their influence on the quantum-critical behavior we have measured the thermal expansion and magnetostriction of $CePd_{1-x}Ni_xAl$ single crystals with Ni content of $0 \leq x \leq 0.144$. The single crystals were grown by Veronika Fritsch using the Czochralski method [51]. The samples have been previously investigated with thermodynamic and neutron scattering measurements [37, 27]. These measurements show that the magnetic order is suppressed with increasing x. The sample with the highest Ni concentration is close to a chemical-pressure-induced QCP at $x_c \approx 0.15$ [37]. Up to this Ni content, the magnetic structure remains unchanged whereas the ordered moment decreases linearly with x and is reduced for $x = 0.135$ to 1/10 of its value for $x = 0$ [27]. The nickel content of the single crystals was determined by atomic absorption spectroscopy (AAS). The homogeneity of the samples was checked by energy dispersive X-ray spectroscopy (EDXS) [see [37]].

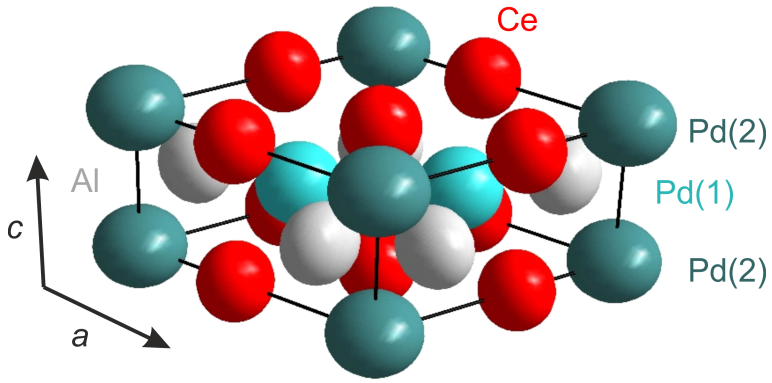

Figure 3.3: Unit cell of CePdAl. The red spheres indicate the position of the cerium atoms, the grey ones the position of the aluminum atoms. There exist two different palladium sites, the Pd(1) (open cyan spheres) forming *a*-*b* AlPd layers and the Pd(2) site (dark cyan spheres) of the CePd layers.

In this work, additional, detailed single-crystal x-ray diffraction (SC XRD) measurements have been performed by Michael Merz (IFP, KIT Karlsruhe) on a STOE *Imaging Plate Diffraction System (IPDS 2T)* to determine the nickel distribution over the nonequivalent Pd(1) and Pd(2) sites [see fig. 3.3]. As the measurements were done in transmission, several small single-crystalline pieces with typical dimensions of about $d \approx 50 - 100\,\mu$m have been cleaved from the samples measured in the dilatometer. For $x = 0.10$ (sample B) and $x < 0.14$ two different pieces of crystals were investigated [see tab. 3.1]. The x dependence of the lattice parameters, shown in fig. 3.4(a) and (b), agrees with earlier studies [38]. The Ni occupation at both Pd sites grows linearly with increasing x [see fig. 3.4(c)] as expected. However, the Pd(2) site of the Ce-Pd layer is clearly favored with a Ni concentration four times higher than that of the Pd(1) site. This appears reasonable because the Pd(2)-site coordination polyhedron is smaller than that of the Pd(1) site. Although the cleaved pieces exhibit sharp Bragg peaks with a very low mosaic spread, typical for high quality single crystals, the Ni concentrations of the samples with $x > 0.05$ significantly deviate from the Ni content determined with AAS and EDXS [see tab. 3.1]. This leads to the conclusion that at higher x, the Ni ions are no longer homogeneously distributed in the bigger crystals measured in the dilatometer. One of the $x = 0.144$ samples [sample $x < 0.14$ in tab. 3.1] showed in all single-crystal x-ray diffraction measurements a clearly lower Ni content though both samples are out of the same batch. Also our thermodynamic measurements presented in chapter 6 clearly point to a (lower) Ni content between $x = 0.10$ and $x = 0.14$. Therefore, in the following this sample will be referred to as $x < 0.14$, the other one as $x = 0.14$. Table 3.1 gives an overview on the investigated samples.

The different thermal expansion and magnetostriction measurements of the $CePd_{1-x}Ni_xAl$ crystals and the discussion of the results will be presented in chapter 5. The samples there will be named: $x = 0.05$, $x = 0.10\,$A, $x = 0.10\,$B, $x < 0.14$ and $x = 0.14$.

Table 3.1: Overview of investigated samples.

x content AAS	x content SC XRD	x at Pd(1)	x at Pd(2)	l_a (mm)	l_c (mm)
0	0	0	0	3.908	4.166
0.05	0.053	0.008	0.143	2.331	2.686
0.10 (sample A)	0.094	0.043	0.196	3.017	0.840
0.10 (sample B)	0.093	0.045	0.189	-	0.446
	0.131	0.072	0.25	-	0.446
0.144 ($x < 0.14$)	0.078	0.067	0.10	2.546	1.903
	0.11	0.032	0.266	2.546	1.903
0.144 ($x = 0.14$)	0.134	0.053	0.295	1.056	0.675

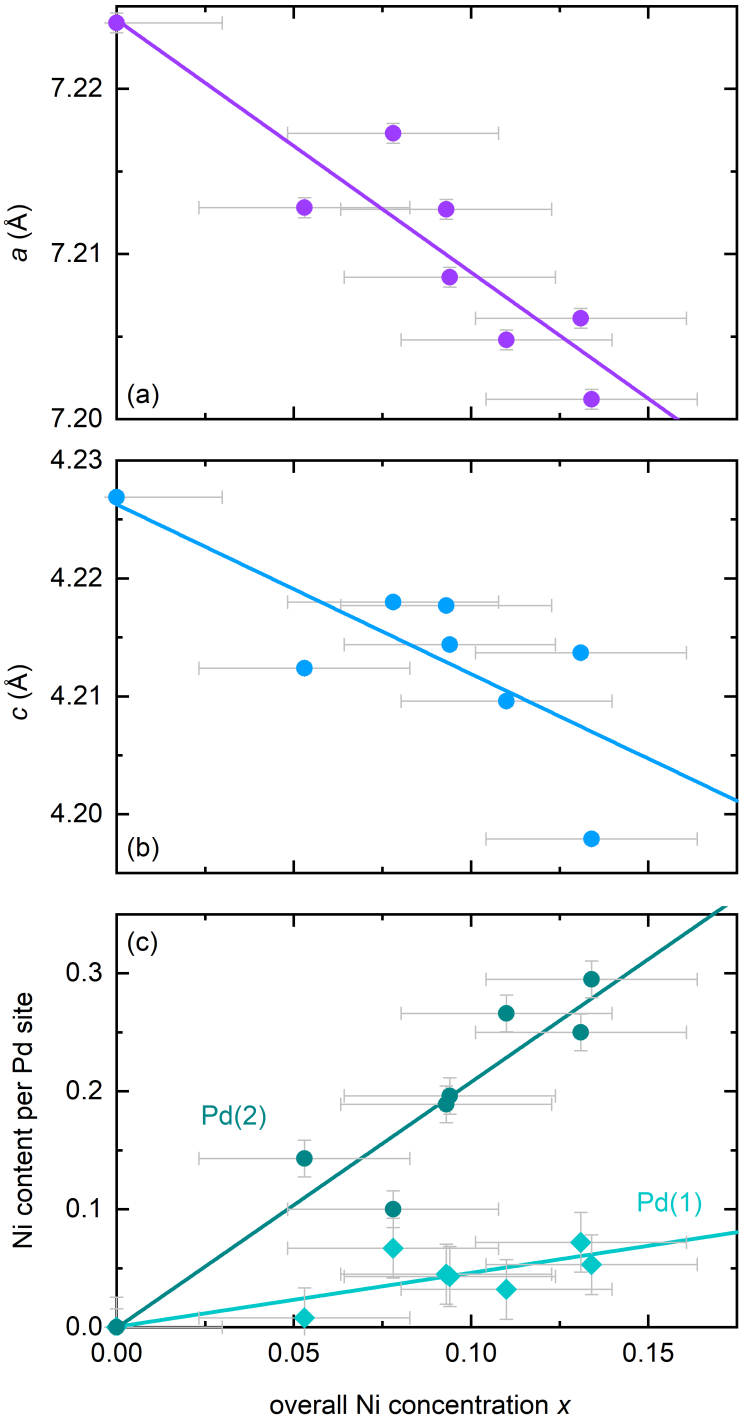

Figure 3.4: (a) a-axis and (b) c-axis lattice parameter of $CePd_{1-x}Ni_xAl$ as a function of the Ni content x.
(c) The Ni concentration of the Pd(1) and Pd(2) site as a function of the overall Ni content x.
Lines are linear fits to the data.

Chapter 4

CePdAl

4.1 Previous Thermodynamic Measurements

The magnetic-phase diagram of CePdAl has been investigated in detail by specific heat, magnetization, and magnetostriction measurements [18]. Figure 4.1(a) shows the temperature dependence of the $4f$ contribution to the specific heat C_{4f}/T in applied magnetic fields parallel to the c axis of up to $\mu_0 H = 14\,\mathrm{T}$. At $H = 0$, the transition to long-range antiferromagnetic order is clearly visible as a sharp λ-like anomaly at $T_\mathrm{N} = 2.7\,\mathrm{K}$. Above T_N, C_{4f}/T exhibits a pronounced tail, typical for critical fluctuations. Its wide temperature range of more than $2 \cdot T_\mathrm{N}$ indicates that these fluctuations are strongly enhanced by geometric frustration. With increasing magnetic field, the transition broadens and shifts to lower temperatures. Between $\mu_0 H_{c1} \approx 3.2\,\mathrm{T}$ and $\mu_0 H_{c2} \approx 3.35\,\mathrm{T}$, the anomaly vanishes and reappears at $H \geq H_{c2}$ as a sharp feature until the critical field is reached at $\mu_0 H_{c3} \approx 4.1\,\mathrm{T}$. By further increase of the magnetic field a Schottky-anomaly arises due to the field-splitting of the Ce^{3+} ground-state doublet, and shifts to higher temperatures [see the inset of fig. 4.1(a)]. In this field range the magnetic $4f$ moments are ferromagnetically polarized along the field direction.

Figure 4.1(b) shows the T dependence of the magnetization M divided by $\mu_0 H$ for different magnetic fields. The strongly enhanced critical fluctuations responsible for the extended tail of C_{4f}/T produce in M pronounced maxima. The data show that up to $\mu_0 H = 4\,\mathrm{T}$ these maxima appear at temperatures T_S clearly above the transition temperatures T_N derived from the specific heat measurements [see the arrows in fig. 4.1(b)]. According to the Maxwell relations, a maximum of $M(T)$ is equivalent to a maximum of the entropy S as a function of the magnetic field. As mentioned in chapter 2.1, such an entropy accumulation arises usually while crossing a phase boundary in dependence of a non-thermal control parameter.

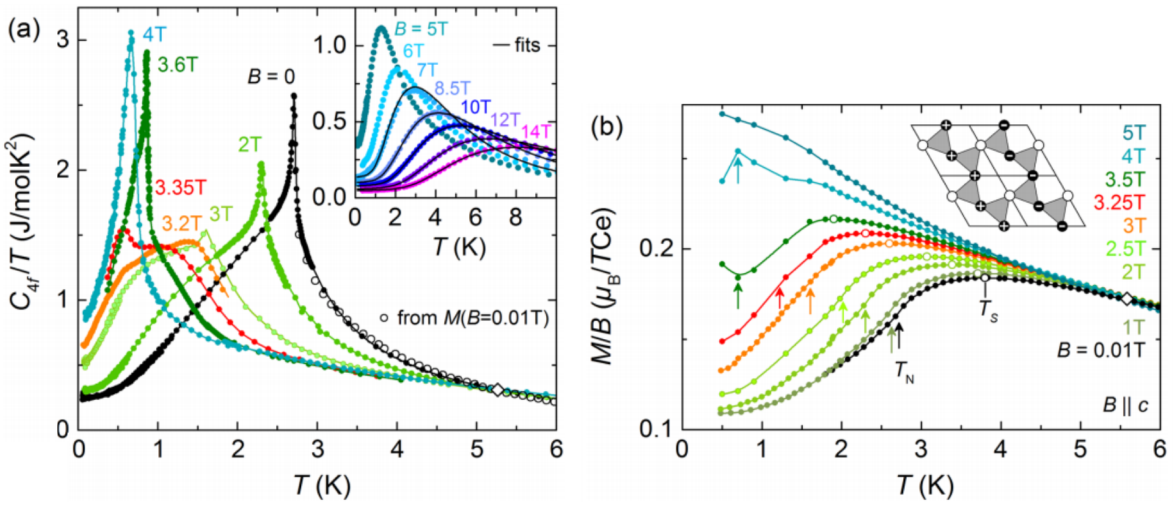

Figure 4.1: (a) $4f$ contribution to the specific heat C_{4f}/T vs temperature for magnetic fields $\mu_0 H$ between 0 and 14 T parallel to the c axis. The inset shows the Schottky anomaly at higher fields.
(b) Magnetization per Ce atom and field $M/\mu_0 H$ for different magnetic fields $\mu_0 H$ between 0 and 5 T likewise parallel to the c axis. The open symbols indicate the temperature T_S of the entropy maximum $S(B)$ while the arrows indicate the transition temperature T_N derived from the specific-heat measurements. Figure taken from [18].

The temperature of the entropy maxima T_S, thus, roughly represents the temperature where the system would order without frustration. The significant difference of T_N and T_S is a clear sign for the frustration of the system and can be taken as measure to quantify the degree of frustration [18]:

$$f_S = \frac{T_S}{T_\mathrm{N}} \tag{4.1}$$

The advantage of this definition of the frustration parameter over the one presented in 2.1.2 is that it can be used to characterize the frustration in magnetic fields as long as M does not saturate at high H. In CePdAl, f_S compares, however, the temperature of the entropy maximum that is produced by all moments with the ordering temperature of the moments that are not frustrated. The values of f_S are, hence, comparatively small to the one presented in 2.1.2. If only the frustrated moments would be considered, f_S would amount to more than 90.

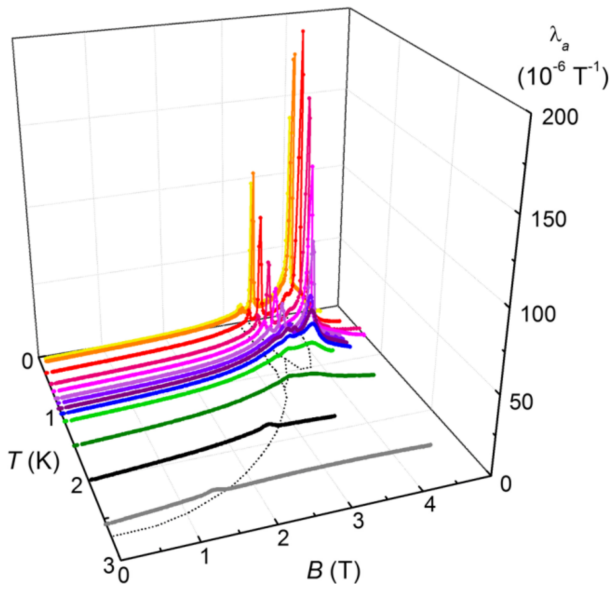

Figure 4.2: Field dependent magnetostriction coefficient λ_a of the a axis for magnetic fields along the c-axis for temperatures $T < T_{\mathrm{N}}$. The $\mu_0 H$-T phase diagram is shown as dashed lines below the data. Figure taken from [18].

To characterize the metamagnetic transitions found in C_{4f}/T and M, the low-temperature part of the phase diagram was studied with magnetostriction measurements. Figure 4.2 shows the magnetostriction coefficient of the a axis λ_a for magnetic fields along c at different constant temperatures. At $T < 0.8\,\mathrm{K}$, there are three sharp peaks visible that are indicative for first-order transitions. The positions of the phase transitions found in the different measurements have been summarized in the phase diagram depicted in 4.3(a). Starting at small fields, three different antiferromagnetic phases could be identified: at $\mu_0 H < 3.25\,\mathrm{T}$, the most extended AF_1 phase, in the field range $\mu_0 H_{c1} \leq \mu_0 H \leq \mu_0 H_{c2} = 3.4\,\mathrm{T}$ the narrow AF_2 phase, and, finally, the dome-like shaped AF_3 phase at $\mu_0 H_{c2} \leq \mu_0 H \leq \mu_0 H_{c3} = 4.1\,\mathrm{T}$. The phase boundaries between the AF_1 and AF_2 phases and those of the AF_3 phase are first-order transitions. Because of the high magnetic anisotropy, the Ising character of the magnetic moments is preserved in the entire field range and spin-flop transitions are not possible.

The field-dependent entropy is displayed in fig. 4.3(b) at different constant temperatures. In the entire field range, S approaches zero as the temperature is lowered, ruling out any frozen-in entropy of a classical spin liquid. For $T < 3.7\,\mathrm{K}$ a pronounced maximum develops that follows roughly the outer phase boundary of the AF_1 phase. Below $T < 2\,\mathrm{K}$ the position of the maximum remains nearly unchanged approximately at the T_N maximum of the dome-shaped AF_3 phase, giving rise to the assumption that the system escapes from the instability by adopting this long-range ordered state.

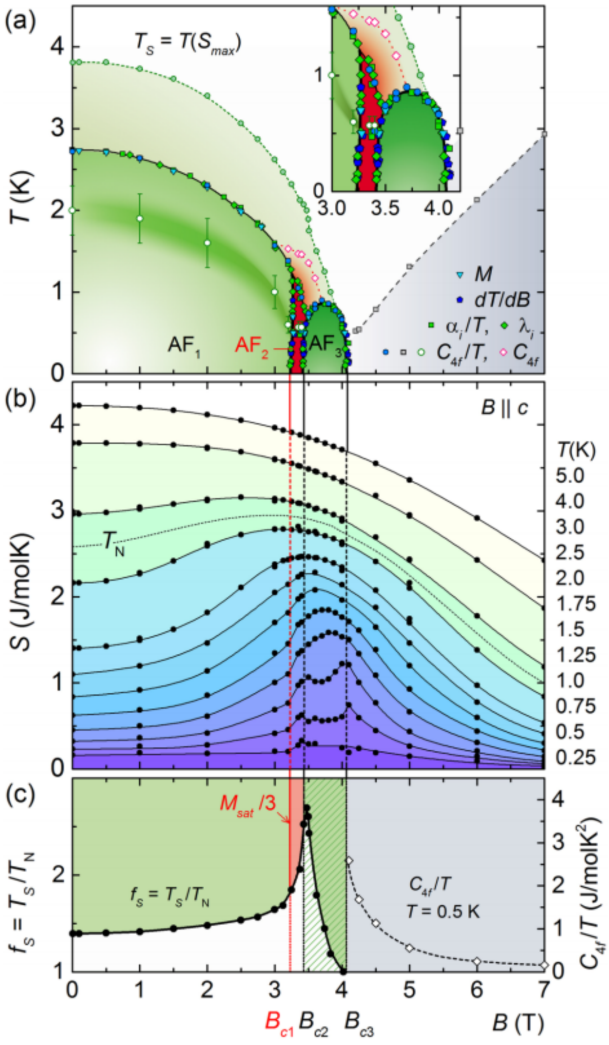

Figure 4.3: (a) Magnetic phase diagram of CePdAl for fields along the c direction derived from various measurement methods as indicated in the legend. The subscripts i for α_i and λ_i indicate the different measurement directions ($||a$ or $||c$). The open circles represent the shoulder visible in C_{4f}/T [see fig. 4.1(a)], the gray squares are the maxima of the Schottky anomalies, and the red open diamonds indicate the maxima of C_{4f}. The inset shows an enlarged view of the AF_2 and AF_3 phases.
(b) Entropy vs. $\mu_0 H$ at different fixed temperatures. The vertical dashed lines indicate the positions of the magnetic phase boundaries.
(c) Frustration parameter $f_S = T_S/T_N$ vs $\mu_0 H$. For $H > H_{c3}$, C_{4f}/T at $T = 0.5\,\mathrm{K}$ is plotted against $\mu_0 H$.
Figure taken from [18].

The critical field of the Kondo effect H_K was estimated from the field-dependent shift of the Schottky-anomaly observed in the specific heat [see the inset of fig. 4.1(b)]. It is with $\mu_0 H_K \approx 2.5\,\mathrm{T}$ close to the transition between AF_1 and AF_2 phase where the entropy maximum starts to evolve. In addition, the magnetization reaches at H_{c1} one third of its saturated moment $M_{sat} \approx 1.6\,\mu_B/\mathrm{Ce}$ [18]. This has given rise to the assumption that at small fields the frustrated moments are shielded by the Kondo effect. By approaching H_K, this selective Kondo screening is removed and the frustrated moments begin to destabilize the magnetic order. This leads to the metamagnetic transition at H_{c1} and the evolution of the AF_2 phase. Interestingly, this phase is characterized by strongly broadened transition anomalies, typical for systems with inherent disorder and short coherence lengths. This assumption seems to be supported by the frustration parameter f_S, which is plotted in fig. 4.3(c). By approaching H_{c1}, f_S increases slowly, shoots up in the AF_2 phase and, finally, drops to 1 in the AF_3 phase. Beyond H_{c3}, no clear signs of a frustration could be observed.

4.2 Thermal expansion and magnetostriction of CePdAl

To study the uniaxial-stress dependence of the characteristic energy scales of CePdAl, additional thermal expansion and magnetostriction measurements have been carried out in this work. Those results will be discussed in the following. The CePdAl single crystal that has been investigated in this work is identical to that studied in [18]. The sample was grown by the Czochralski method by V. Fritsch [51].

In fig. 4.4(a) the linear-thermal expansion coefficient of the a axis divided by T is compared with the specific heat C_{4f}/T at zero magnetic field. α_a/T is positive in the whole temperature range and rises slowly as the transition temperature is approached. As already pointed out by Grüneisen, both quantities exhibit a similar T dependence with a clearly visible transition anomaly at T_N and an extended tail at higher T due to the critical fluctuations enhanced by the frustration. The ratio between α_a/T and C_{4f}/T is essentially the aforementioned Grüneisen ratio $\Gamma_{\sigma_i} = V_m \frac{\alpha_i}{C}$ which is expected to be constant if a single E^* dominates. As directly visible in fig. 4.4(a), Γ_{σ_a} cannot have the same value on both sides of the transition, as for lower T, α_a/T lies above and for higher T beneath C_{4f}/T. The calculated Γ_{σ_a} is plotted in fig. 4.4(b). It clearly is not constant, but monotonically increases towards lower temperatures. Surprisingly, the well-defined transition anomaly, visible in α_a/T and C_{4f}/T, nearly disappears in Γ_{σ_a}, apart from a negligibly small slope change at T_N. The slope change occurs approximately in the temperature range where α_a/T and C_{4f}/T exhibit a shoulder below T_N.

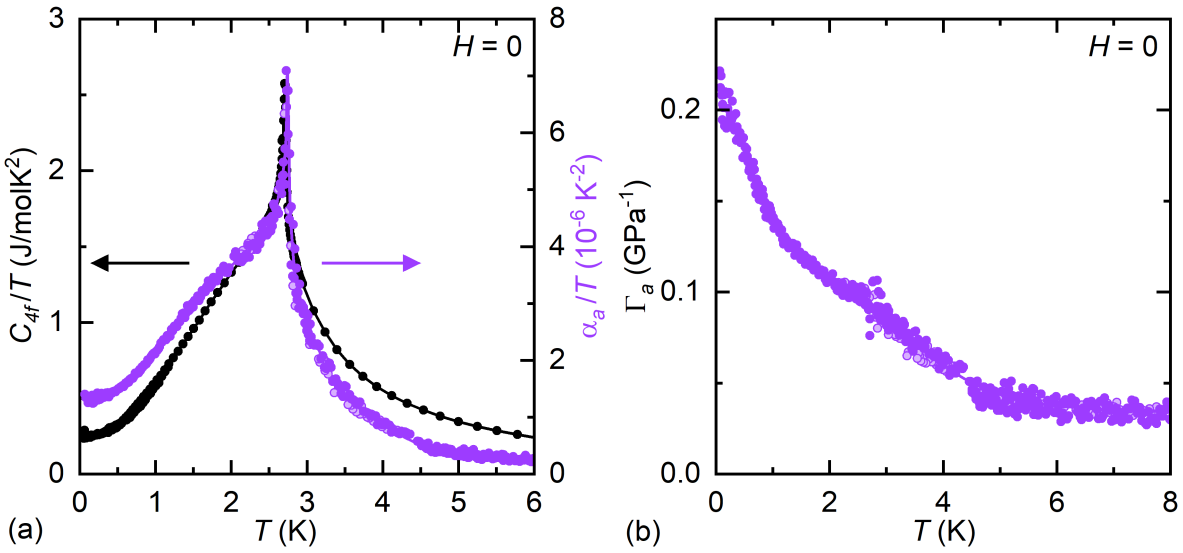

Figure 4.4: (a) Comparison of the AF-transition anomaly in the specific heat C_{4f}/T (black dots) and thermal expansion along the a axis α_a/T (purple dots) in zero field to demonstrate the calculation of the Grüneisen ratio Γ_{σ_a}.
(b) The corresponding Grüneisen ratio Γ_{σ_a} as function of temperature. The transition is hardly visible.
Full symbols indicate measurements during heating, open symbols during cooling the sample. The specific-heat data are taken from [37]

The increase of Γ_{σ_a} towards lower temperatures can have two different origins: It is either the onset of a divergence of Γ_{σ_a} for $T \to 0$ and would then indicate the proximity to a QCP with a vanishing E^*, or it is caused by a crossover from one to an other dominant energy scale. To clarify this, one can use the anisotropic stress dependence of E^*. This anisotropy is specific for the underlying interactions. For a single E^* the quotient of the Grüneisen ratios along different axes should be constant:

$$\frac{\Gamma_{\sigma_i}}{\Gamma_{\sigma_j}} = \frac{\alpha_i}{\alpha_j} = \frac{\partial E^*}{\partial p_i}\left(\frac{\partial E^*}{\partial p_j}\right)^{-1} = \text{const.} \tag{4.2}$$

Figure 4.5(a) shows the linear thermal-expansion coefficients α_a/T (purple) and α_c/T (blue) for both crystallographic directions at $H = 0$. At $T < 0.6\,\text{K}$, α_a/T and α_c/T scale on top of each other by a constant factor of $\alpha_c/\alpha_a \approx -6.1$ which indicates that at low temperatures a single E^* starts to dominate the system. In this respect, the increase of $|\Gamma_{a,c}|$ might reflect first signs of quantum-critical behavior.

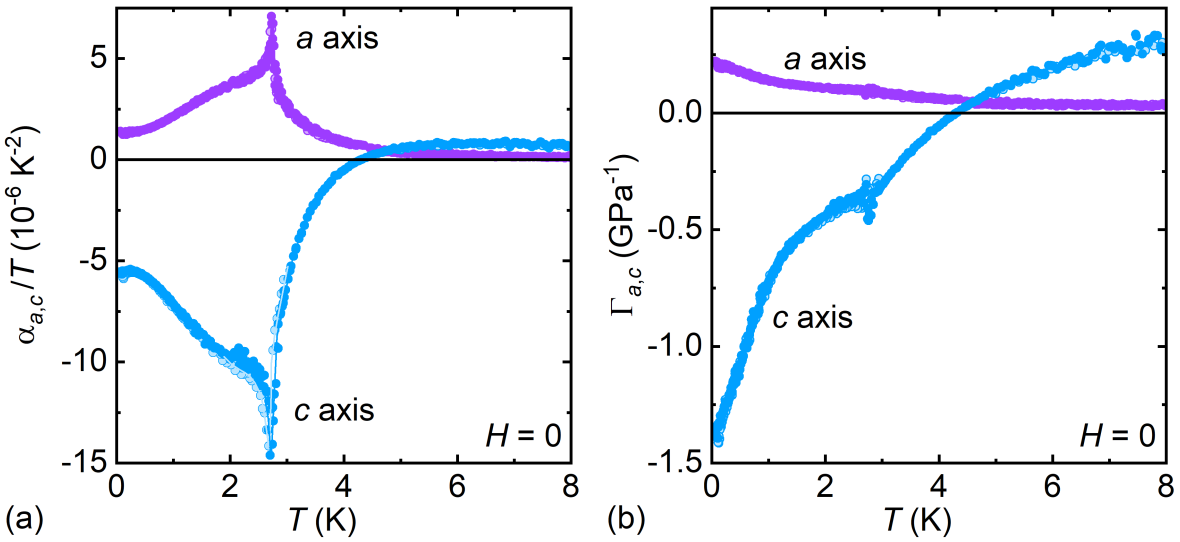

Figure 4.5: (a) Temperature dependence of the thermal expansion parameters α_a/T (purple dots) and α_c/T (blue dots) for both crystallographic directions in zero field. (b) The corresponding Grüneisen ratios Γ_{σ_a} (purple dots) and Γ_{σ_c} (blue dots) vs. temperature. In both cases the transition anomaly is hardly visible anymore. Full symbols indicate measurements during heating, open symbols during cooling the sample. The specific-heat data are taken from [37]

The thermal-expansion data plotted in fig. 4.5(a) clearly exhibit a change of the anisotropy when the partial antiferromagnetic order of the AF_1 phase sets in. With decreasing T, α_c/T is in the beginning positive and changes its sign at $T \approx 4.5\,\mathrm{K}$. This change indicates the different stress dependencies of the underlying E^*s: at higher T, the system is controlled by the Kondo effect $E^* \propto T_K$ which has, as a local interaction, a more isotropic, positive pressure dependence along both axes. In the antiferromagnetic phase, on the other hand, $E^* \propto T_\mathrm{N}$ increases for stress along the a and decreases for stress along the c axis. While such sign changes are frequently observed at phase transitions, they usually appear exactly at the transition temperature. In CePdAl, however, α_c changes its sign far above T_N. As $\alpha_c \propto -\frac{\partial S}{\partial \sigma_c}$, this again points to a maximum of S as function of a nonthermal control parameter, here given by σ_c, that develops far above T_N and corresponds to the S maximum as a function of the magnetic field.

Together with the absence of a clear transition signature in Γ_{σ_a} and Γ_{σ_c} [see fig. 4.5(b)], this conveys the impression that the transition extends over a wide temperature range. The critical fluctuations start at high temperature leading to a smooth crossover in the anisotropy of $\partial S/\partial \sigma_i$ from a Kondo dominated to an antiferromagnetically ordered state. The continuous change of Γ_{σ_i} down to the lowest measured temperature of $T = 20\,\mathrm{mK}$ indicates that even here the evolution towards the ordered state is still in

progress. To our knowledge, this is the first time that such a retarded evolution of a phase transition could be observed. In view of the geometric frustration of CePdAl, this seems to be a particular feature of partial order in frustrated materials.

4.3 CePdAl in Magnetic Field

In the following, we will discus the field dependence of the thermal expansion in CePdAl. For clarity, the discussion will in the beginning focus on measurements along the a axis that have been measured during cooling the sample at constant magnetic fields along the c axis.

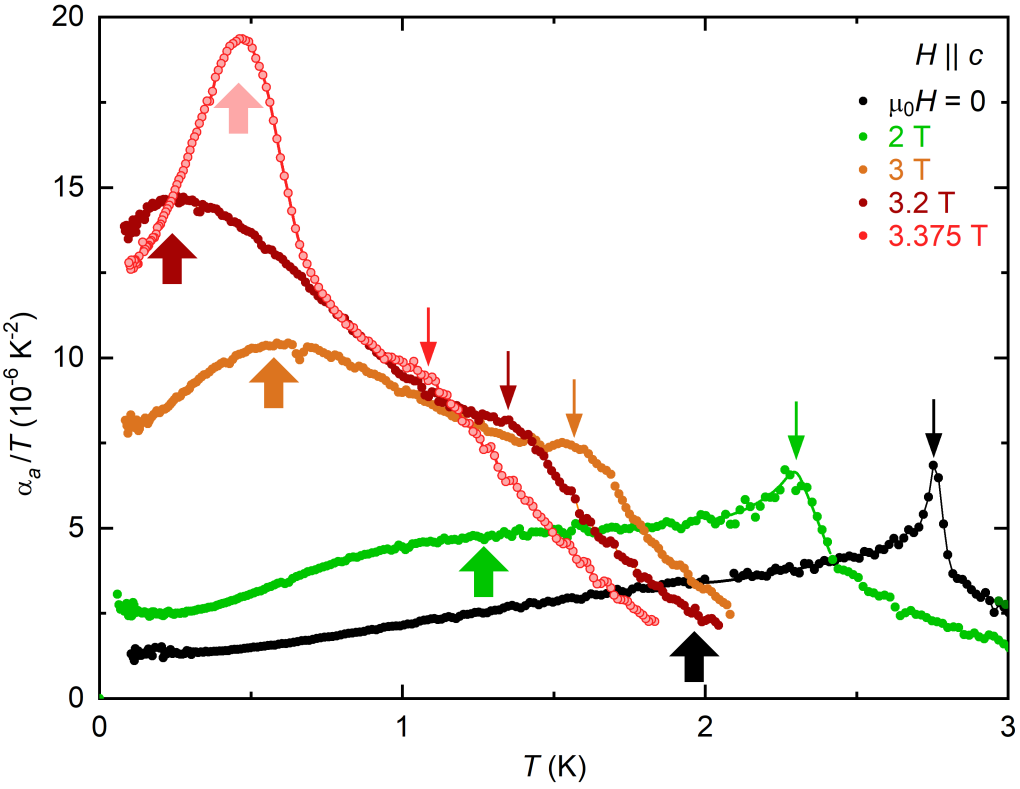

Figure 4.6: Thermal expansion along the a axis α_a/T vs. T at different magnetic fields between $H = 0$ and $\mu_0 H = 3.375\,\mathrm{T}$ applied along the c direction. The small, colored arrows indicate the transition temperatures. At increasing H, a second anomaly appears, marked by big colored arrows. At $\mu_0 H = 3.375\,\mathrm{T}$, in the AF_2 phase, this anomaly gets replaced by a large peak. Lines are guides to the eye.

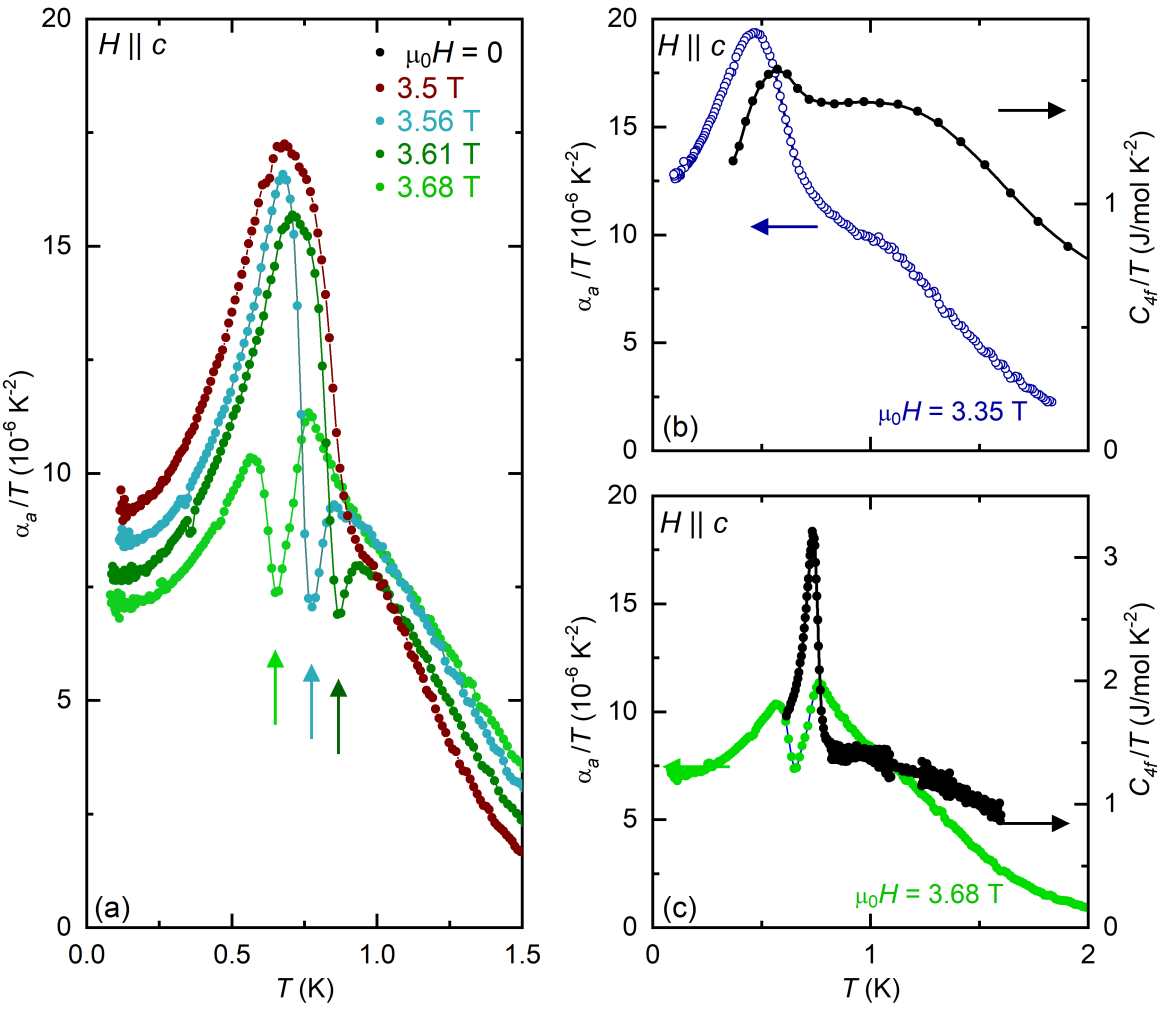

Figure 4.7: (a) Thermal expansion along the a axis α_a/T vs. T in different magnetic fields between $\mu_0 H = 3.5\,\mathrm{T}$ and $\mu_0 H = 3.68\,\mathrm{T}$ applied along the c direction. The small, colored arrows indicate the phase transition to the AF_3 phase. Comparison of α_a/T with C_{4f}/T at (b) $\mu_0 H = 3.35\,\mathrm{T}$ and (c) $\mu_0 H = 3.68\,\mathrm{T}$. Lines are guides to the eye. The specific-heat data are taken from [18].

Figure 4.6 shows the temperature dependence α_a/T along the a axis between $H = 0$ and $\mu_0 H = 3.375\,\mathrm{T}$. With increasing H the transition shifts to lower temperatures and gets broadened. Simultaneously, a second anomaly appears just below T_N which is likewise shifted to lower T, but gets more pronounced at higher H, until it finally dominates the thermal expansion at $\mu_0 H = 3.2\,\mathrm{T}$. This anomaly corresponds to a shoulder of the specif-heat coefficient C_{4f}/T shown in fig. 4.1(a). Its larger size in α_i/T points to a strongly enhanced sensitivity to pressure. At the phase boundary $\mu_0 H_{c2} \approx 3.25\,\mathrm{T}$, this anomaly is replaced by an even larger peak which stays roughly at $T \approx 0.5\,\mathrm{K}$. At

higher fields $3.5\,\mathrm{T} < \mu_0 H < 3.7\,\mathrm{T}$, a sharp dip appears that moves to lower T with increasing H [see fig. 4.7(a)]. This dip represents the discontinuous phase boundary to the AF_3 phase which has in this field range a negative stress dependence along the a axis. Figures 4.7(b) and (c) show a comparison of α_a/T with C_{4f}/T. The transition to the AF_3 phase is clearly visible in both thermodynamic probes.

At higher magnetic fields, beyond the upper critical field H_{c3}, the thermal expansion exhibits, like the specific heat, a Schottky anomaly that is shifted linearly with H to higher temperatures[see fig. 4.8]. This anomaly is caused by the Zeeman splitting of the Ce^{3+} ground-state doublet, as mentioned previously. At temperatures below it, the Kondo screening is suppressed and the magnetic moments are ferromagnetically polarized along the field direction.

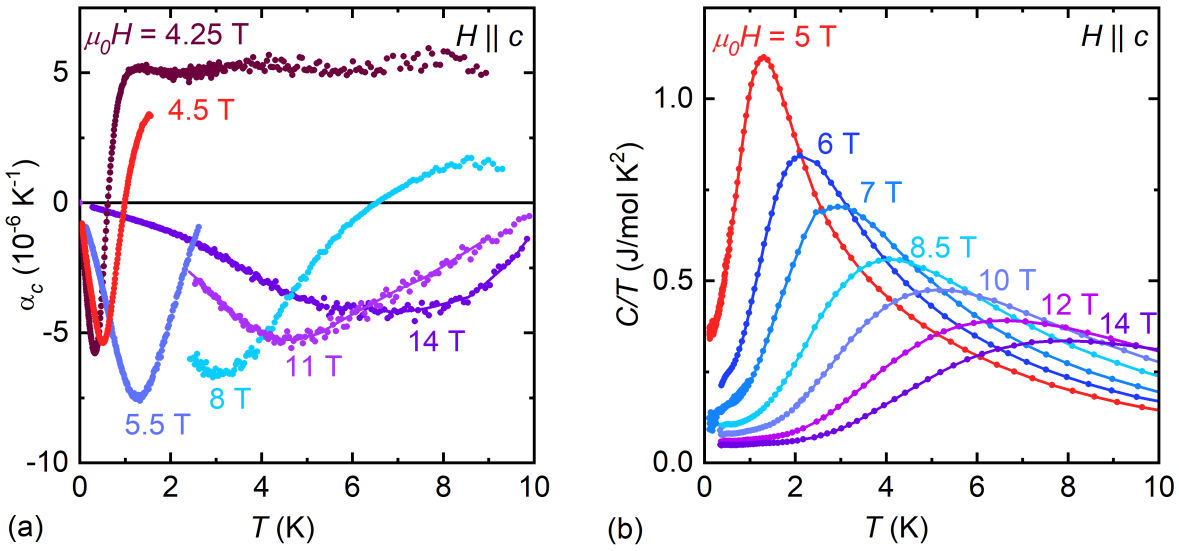

Figure 4.8: (a) The linear thermal-expansion coefficient along the c axis α_c and (b) the specific heat C/T vs. T in high magnetic fields up to $\mu_0 H = 14\,\mathrm{T}$ applied along the c direction. Both quantities exhibit a field dependent Schottky anomaly due to the Zeeman splitting of the Ce^{3+} ground-state doublet. The specific-heat data are taken from [18].

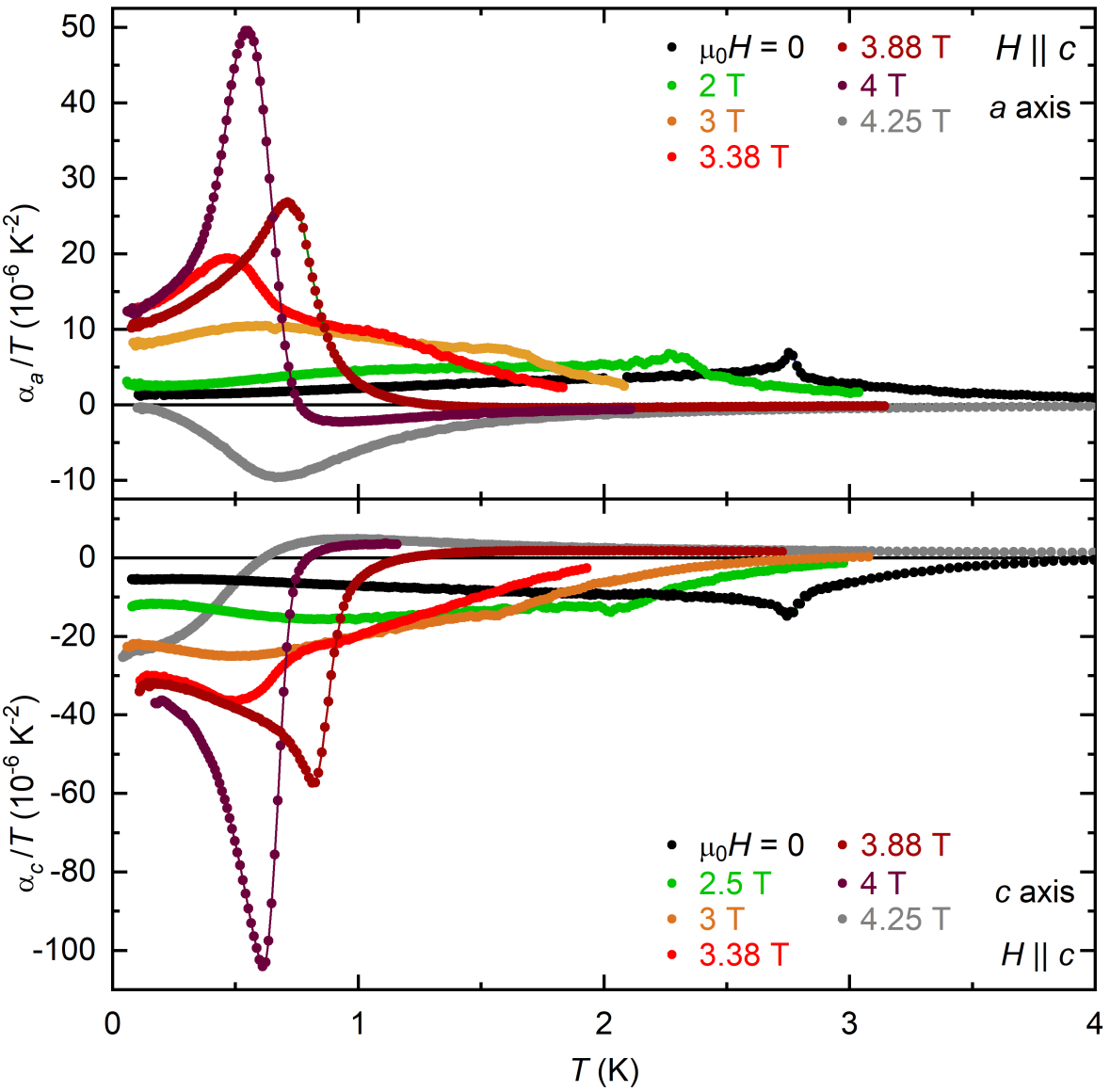

Figure 4.9: Summary of the thermal expansion along the a axis and the c axis in fields between $H = 0$ and $\mu_0 H = 4.25\,\mathrm{T}$ applied along the c direction. Lines are guides to the eye.

In fig. 4.9 the thermal-expansion measurements of CePdAl are summarized for both crystallographic directions in the field range $0 \leq \mu_0 H \leq 4.25\,\mathrm{T}$. For clarity only data obtained during heating the sample are shown. Up to $\mu_0 H = 3.38\,\mathrm{T}$, the thermal expansion parallel to the a axis stays positive in the temperature range shown here. In the field range of the AF_3, however, it starts to change its sign above T_N and for fields above $\mu_0 H = 4\,\mathrm{T}$, when the AF order is suppressed completely, it is negative up to

4 K. On the first sight, the T dependence of α_c/T seems to mirror that of α_a/T. But in contrast to the a direction, α_c/T is positive for higher temperatures and negative at low temperatures for all fields.

In conclusion, the stress anisotropy of CePdAl changes when the partial AF order evolves with decreasing T at $H = 0$ and again when the ordered state and the frustration is suppressed at $H > H_{c3}$. This again indicates that in the related field and temperature ranges, CePdAl is controlled by different E^*s.

A similar, but not equivalent change in the system's anisotropy can be observed in the magnetostriction. Figure 4.10 shows the field dependence of λ_a and λ_c for fields in c direction at a temperature of $T = 0.1$ K. The first-order metamagnetic transitions between the AF_1, AF_2, and AF_3 phases as well as the suppression of the magnetic order for fields at $\mu_0 H \gtrsim \mu_0 H_{c3} \approx 4.1$ T can be seen in the three pronounced peaks in both directions. At higher H, λ_a and λ_c both asymptotically approach constant values. The change from the partially ordered to the field-polarized state leads again to a significant change of the stress dependent anisotropy of M because $\lambda_i = -V_m \partial M/\partial \sigma_i$. In the AF order, roughly $\partial M/\partial \sigma_c \approx -\partial M/\partial \sigma_a$. In contrast to that, the magnetization of the field-polarized state depends only on uniaxial stress along the c direction. At the metamagnetic transitions, small, but significant hystereses can be observed that are typical for first-order transitions.

The thermal expansion data exhibit likewise differences between measurements taken during heating and cooling the sample (see fig 4.11). These hystereses appear, however, even in the temperature and field range where the phase transitions are apparently continuous. An example for this behavior is given at $H = 0$ in fig 4.11(a). For comparison below that figure, the field-dependent component of the magnetic-ordering vector τ along the reciprocal c axis is plotted in the same temperature range. As mentioned above, CePdAl exhibits an unusual temperature dependence of its magnetic structure below T_N, within the AF ordered phase. The hysteresis around the phase transition that can be clearly seen in α_c/T terminates exactly at the temperature where the magnetic structure locks in and τ reaches a constant value. In addition, the hysteresis in the thermal expansion along the c axis is much more pronounced than that along the a axis [see 4.4(a)]. It seems, therefore, that these hystereses of α_i are caused by the temperature dependent variation of the magnetic structure along the c axis and that they cannot serve as evidence against a second-order transition.

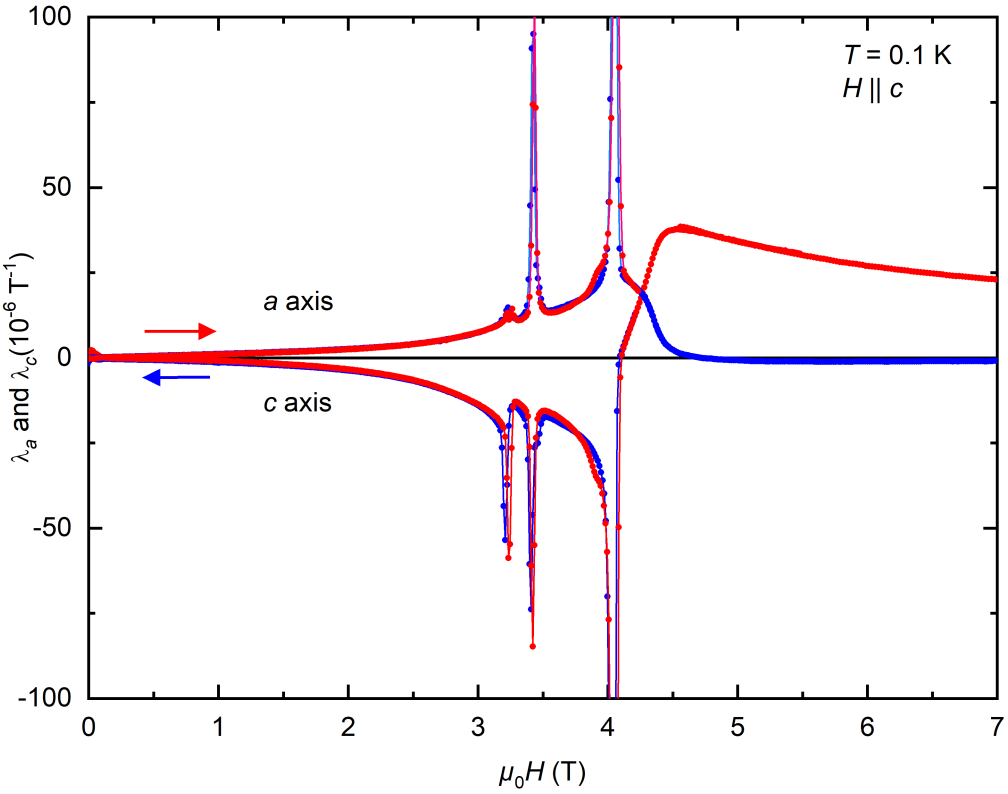

Figure 4.10: Magnetic field dependence of the magnetostriction coefficients λ_a and λ_c along the a and c axis, respectively, for field applied in c direction at constant temperature of $T = 0.1\,\mathrm{K}$. Red data points are measured with increasing and blue data points with decreasing magnetic field. Lines are guides to the eye.

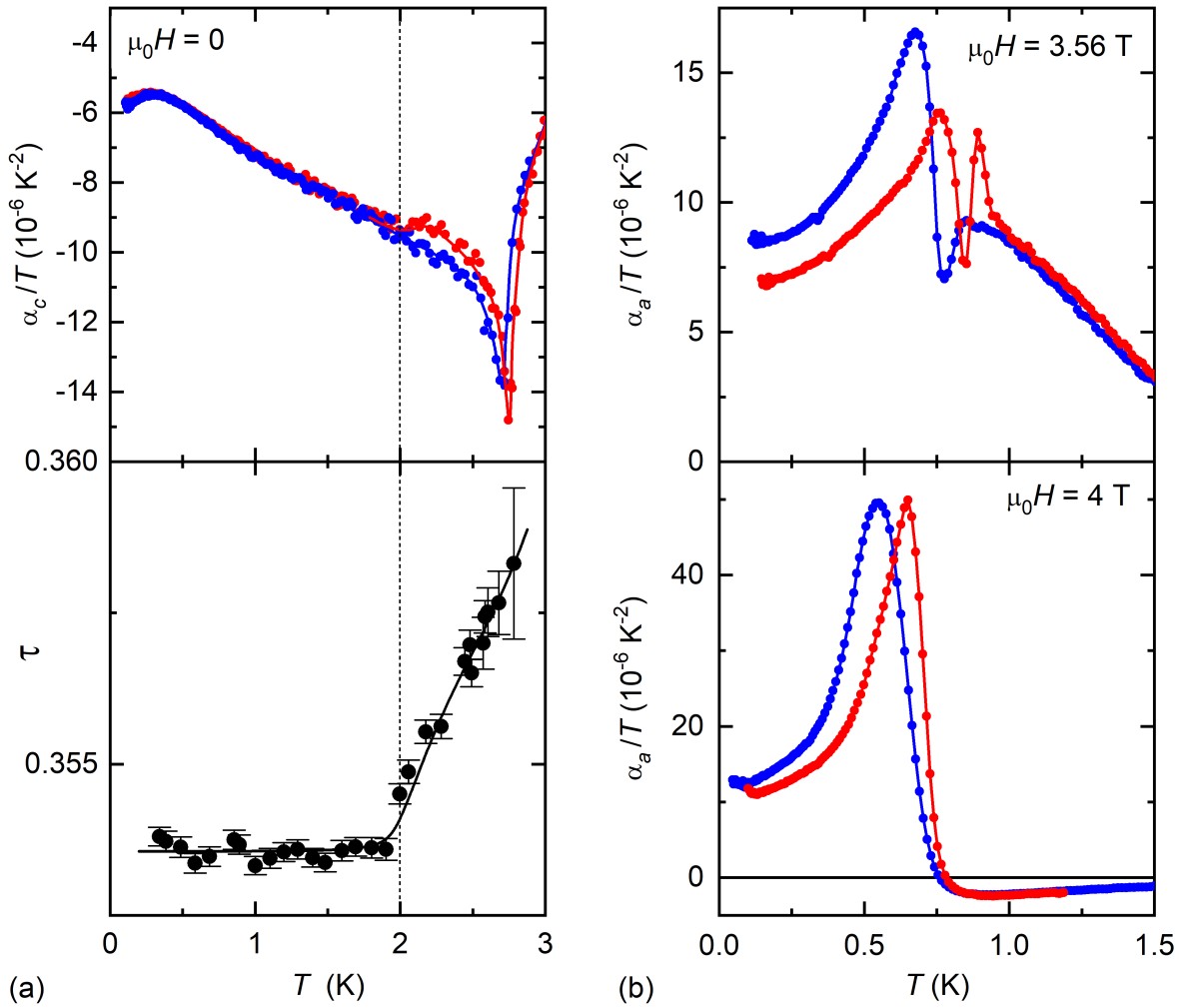

Figure 4.11: (a) The hysteresis of thermal expansion along the c direction α_c/T vs. temperature and the temperature dependence of τ, the component of the magnetic ordering vector $Q = (0.5\ 0\ \tau)$ in the reciprocal c axis direction. The data of τ were taken from [26].
(b) The hysteresis in the thermal expansion along the a direction α_a/T at $\mu_0 H = 3.56\,\mathrm{T}$ and $4\,\mathrm{T}$. The sharp peaks are the anomalies of the first-order transition to the AF_3 phase.
The red data points are measured during heating and the blue data points during cooling the sample at constant magnetic field. Lines are guides to the eye.

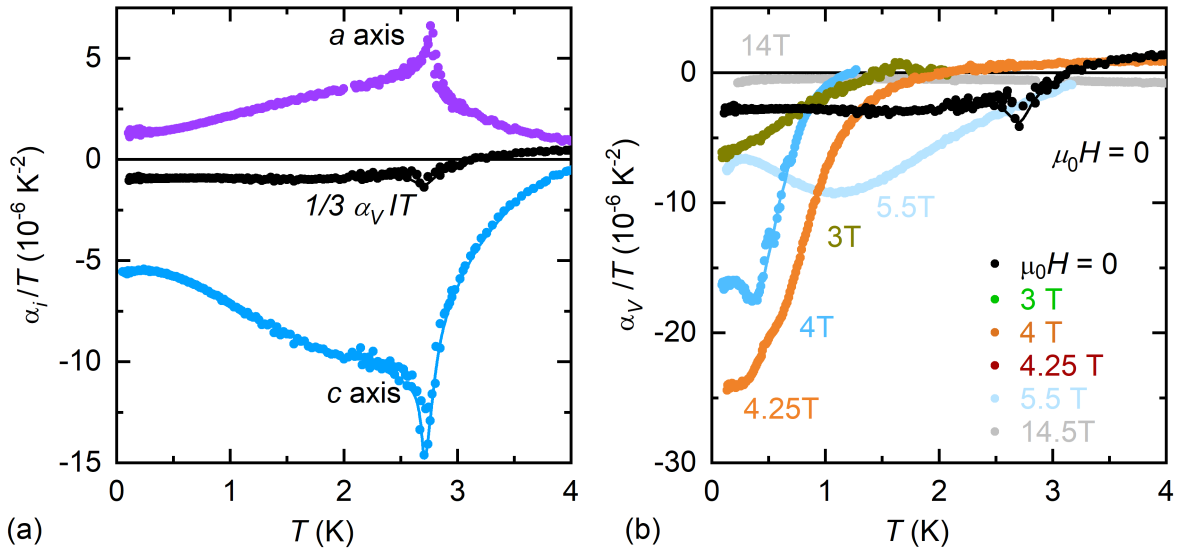

Figure 4.12: (a) The linear and volume thermal-expansion coefficients α_a/T (purple dots), α_c/T (blue dots) and $1/3 \cdot \alpha_V/T$ (black dots) as a function of the temperature at zero magnetic field.
(b) The volume thermal-expansion coefficient α_V/T vs. temperature at different magnetic fields up to $\mu_0 H = 14\,\mathrm{T}$.
Lines are guides to the eye.

So far, we mainly addressed the uniaxial stress dependences of the entropy and magnetization. To study the hydrostatic pressure dependence of S, we calculate the volume thermal expansion by $\alpha_V = 2\alpha_a + \alpha_c = -V_m \partial S/\partial p$. In fig. 4.12(a) the linear and volume thermal-expansion coefficients at $H = 0$ (the latter divided by $3 \cdot T$) are plotted against the temperature. As can be seen, α_V/T and, hence, the hydrostatic pressure dependence of S is in the AF phase significantly smaller than $|\partial S/\partial \sigma_a|$ and $|\partial S/\partial \sigma_c|$. Such a strong anisotropy is characteristic for antiferromagnetic interactions of nearly localized moments. Figure 4.12(b) shows the temperature dependence of α_V/T at different magnetic fields up to $\mu_0 H = 14\,\mathrm{T}$. $\partial S/\partial p$ is positive in the entire field and temperature range of the AF order. As the Kondo effect should produce a large, negative hydrostatic pressure dependence of S, it obviously hardly affects the partial magnetic order. In high fields, when the magnetic order and the Kondo effect are suppressed, the absolute value of α_V/T gets very small and constant in the whole temperature range shown here. The temperature independent small value of α_V/T points in this field range to a Fermi liquid of a weakly correlated metal with a typical diminutive pressure dependence of the Sommerfeld coefficient $\partial\gamma/\partial p = -V_m \alpha_V/T$.

4.4 CePdAl - Uniaxial Stress and Strain Dependences of T_N

The combination of thermal-expansion and specific-heat measurements allows to estimate the uniaxial and hydrostatic pressure dependences of the magnetic phase-transition temperature T_N with Pippard's extension to the Ehrenfest relation and the Clausius-Clapeyron equation. The obtained values are plotted in fig. 4.13(a) against the magnetic field. From $H = 0$ up to the beginning of the AF_2 phase at $\mu_0 H \approx 3\,T$, the pressure dependences remain for both directions nearly constant. Uniaxial pressure along the a axis enhances T_N and thus strengthens the magnetic order, whereas stress along the c axis weakens the order. This effect is about twice as strong as that of σ_a. The apparent divergences above 3 T are due to the pressure dependences of the metamagnetic critical field H_{c1}. At the onset of the AF_3 phase, both uniaxal stress dependences are negative and nearly isotropic. With further increased field, however, the difference between $dT_N/d\sigma_a$ and $dT_N/d\sigma_c$ grows again until at the upper critical field H_{c3}, $2dT_N/d\sigma_a = -dT_N/d\sigma_c$ and the isotropic, hydrostatic component reaches zero. In the entire field range of the magnetic order at $H < H_{c3}$, this hydrostatic pressure dependence is negative and, like $\partial S/\partial p$, comparatively small. In accordance to measurements under finite hydrostatic pressure, T_N decreases with increasing p [34, 35, 36].

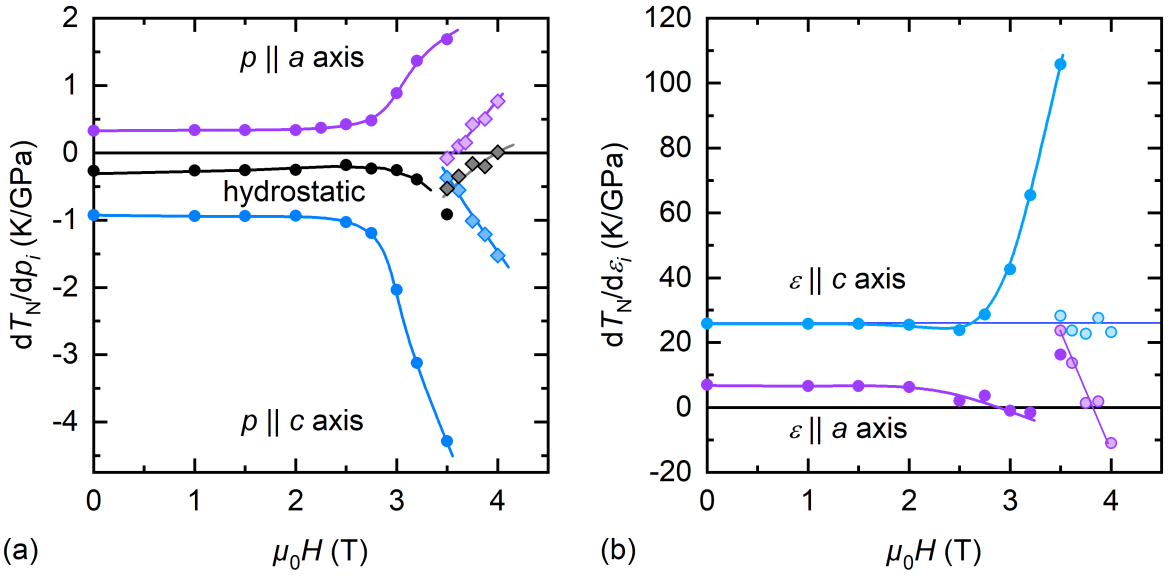

Figure 4.13: (a) The uniaxial and hydrostatic pressure dependences of the Néel temperature T_N as a function of the magnetic field applied parallel to the c direction. The dots represent the dependences of the AF_1 and AF_2 phases and the diamonds those of the AF_3 phase. Lines are guides to the eye.
(b) The uniaxial strain dependences of T_N vs. the magnetic field.

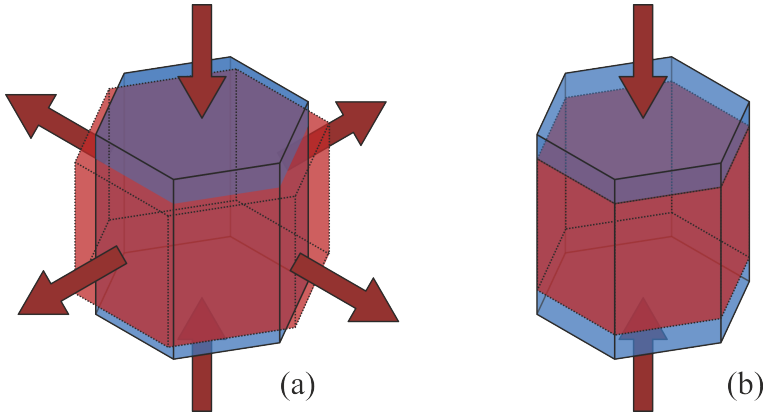

Figure 4.14: Schematic illustration of uniaxial pressure (a) and uniaxial strain (b) applied to a hexagonal lattice. Due to the Poisson effect uniaxial pressure is always accompanied by a dilatation perpendicular to the stress direction, whereas uniaxial strain affects the lattice only along one direction.

The effect of uniaxial pressure on a crystal lattice depends on its specific elastic behavior. Additionally, any application of stress generates a dilatation perpendicular to it, the so-called Poisson effect (see fig. 4.14). As a result, it is impossible to relate uniaxial pressure dependences directly to changes of the crystal structure. In order to do that, the stress dependences have to be converted into strain dependences. This requires the determination of the elastic constants c_{ij}. The hexagonal crystal structure of CePdAl is characterized by five independent constants [52]. As we consider only symmetry-conserving stress combinations we focus in the following on the four longitudinal constants c_{11}, c_{12}, c_{13}, and c_{33}.

So far, there exist only very few investigations of the elastic behavior of Ce-based heavy-fermion systems with ZrNiAl-type crystal structure. The only publication of CePdAl reports X-ray diffraction measurements under quasi-hydrostatic pressure up to 11 GPa with a solid pressure transmitting medium (1:4 amorphous boron and epoxy resin) [34]. Using the Birch equation the authors obtained a bulk modulus of 47.8 ± 1.7 GPa. An analysis of the pressure-dependent lattice parameters results in the linear compressibilities $k_a = 7.24 \cdot 10^{-3}\,\mathrm{GPa}^{-1}$ and $k_c = 6.44 \cdot 10^{-3}\,\mathrm{GPa}^{-1}$ along the a and c axis, respectively. The elastic constants c_{11}, c_{33}, c_{44} and c_{66} of the related, isostructural compound CeRhSn have been determined by ultrasonic-sound velocity measurements as a function of temperature [53, 54]. The temperature dependence of the c_{ij} clearly reveals the Kondo effect and the presence of a crystal-electric field that splits the $4f$ multiplet of the Ce^{3+} ions. Since for hexagonal crystal structures c_{66} is equivalent with $(c_{11} - c_{12})/2$, the only missing elastic constant is c_{13}. By assuming that the elastic bahavior of CeRhSn roughly equals that of CePdAl, we can use the bulk modulus of CePdAl to estimate the missing c_{13}. In addition, at our request, *the materials project*

calculated the elastic constants of CePdAl by using the density-functional theory [55]. As the calculations do not account for the hybridization the $4f$ electrons with the conduction band the obtained values exceed the measurements by a factor of ≈ 2. The calculated and measured c_{ij} exhibit, however, the same elastic anisotropy and should, hence, give the same qualitative behavior.

For the conversion we have used the following values which have been obtained from the measurements on CeRhSn and CePdAl, and extrapolated to zero temperature (in GPa):

$$c_{ij} = \begin{pmatrix} 79.9 & 19.9 & 43.0 & 0 & 0 & 0 \\ & 79.9 & 45.6 & 0 & 0 & 0 \\ & & 58.5 & 0 & 0 & 0 \\ & & & 49.0 & 0 & 0 \\ & & & & 49.0 & 0 \\ & & & & & 30.0 \end{pmatrix}. \tag{4.3}$$

The converted strain dependences of T_N are displayed in 4.13(b). The data demonstrate that the magnetic order of the AF_1 and AF_2 phase is mainly controlled by the length of the c-lattice parameter. In the AF_3 phase, $\mathrm{d}T_\mathrm{N}/\mathrm{d}\epsilon_c$ stays constant at a similar value than of the AF_1 phase. $\mathrm{d}T_\mathrm{N}/\mathrm{d}\epsilon_a$, on the other hand, changes from a positive to a negative strain dependence. Its sign change is close to the maximum of the dome-shaped AF_3 phase. Notably, T_N increases when the c axis is elongated, i.e., the Ce-Pd layers are pulled apart from each other. This clearly rules out a low dimensionality of the magnetic order as source for the strong critical fluctuations seen in the specific heat, magnetization and thermal expansion measurements and gives further evidence that the frustration has an essential impact on the magnetic order in CePdAl.

Chapter 5

$CePd_{1-x}Ni_xAl$

5.1 $CePd_{0.95}Ni_{0.05}Al$

5.1.1 $CePd_{0.95}Ni_{0.05}Al$ at Zero Magnetic Field

The specific heat and thermal expansion along the a axis of the $CePd_{5.95}Ni_{0.05}Al$ sample at $H = 0$ are plotted as a function of temperature in fig. 5.1(a). In both measurements, the antiferromagnetic transition is clearly visible, though not as sharp as in the parent compound CePdAl [see fig. 4.4]. As expected, the transition temperature is slightly reduced to $T_N \approx 1.9\,K$. At lower temperatures, α_a/T shows a distinct difference between cooling (open symbols) and heating (full symbols) the sample. As already indicated by fig. 5.1(a), the Grüneisen ratio increases down to the lowest measured temperature, even deep in the AF ordered phase, similar to $x = 0$ [see fig. 5.1(b)]. In contrast to CePdAl, the transition anomaly now appears in Γ_{σ_a} as a slight kink, but is still much smaller than the anomalies observed in α_a/T and C_{4f}/T.

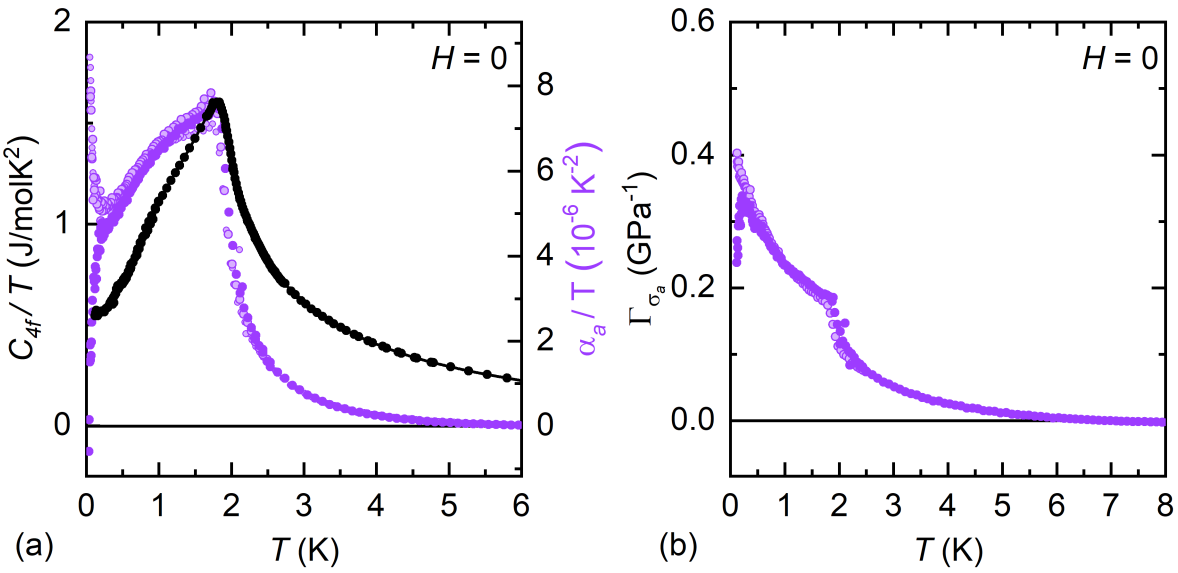

Figure 5.1: (a) Specific heat C_{4f}/T (black data points) and thermal expansion along the a axis α_a/T (purple data points) of $CePd_{0.95}Ni_{0.05}Al$ as a function of temperature in zero magnetic field.
(b) The corresponding Grüneisen ratio Γ_{σ_a} as a function of temperature calculated from the data of (a).
The specific heat data are taken from Ref. [37]. Full symbols represent measurements during heating and open symbols during cooling the sample. Lines are guides to the eye.

The c-axis thermal expansion α_c/T of $CePd_{5.95}Ni_{0.05}Al$ approximately follows that of the parent compound CePdAl with a reduced T_N [see fig. 5.2(a)]. With decreasing T, α_c/T reveals again a sign change well above T_N and reaches large negative values at $T \leq T_N$. Starting just above T_N, the data show for both directions a pronounced difference between cooling and heating. This hysteresis is much larger than that observed in CePdAl and covers a much more extended temperature range. The strongly enhanced up- and downturns of α_a/T and α_c/T at $T \to 0$ demonstrate that below T_N the system no longer reaches a thermal equilibrium. The calculated Grüneisen ratios are displayed in fig. 5.2(b). As already seen in the parent compound, the absolute values of Γ_{σ_a} and Γ_{σ_c} continuously increase below T_N with decreasing T.

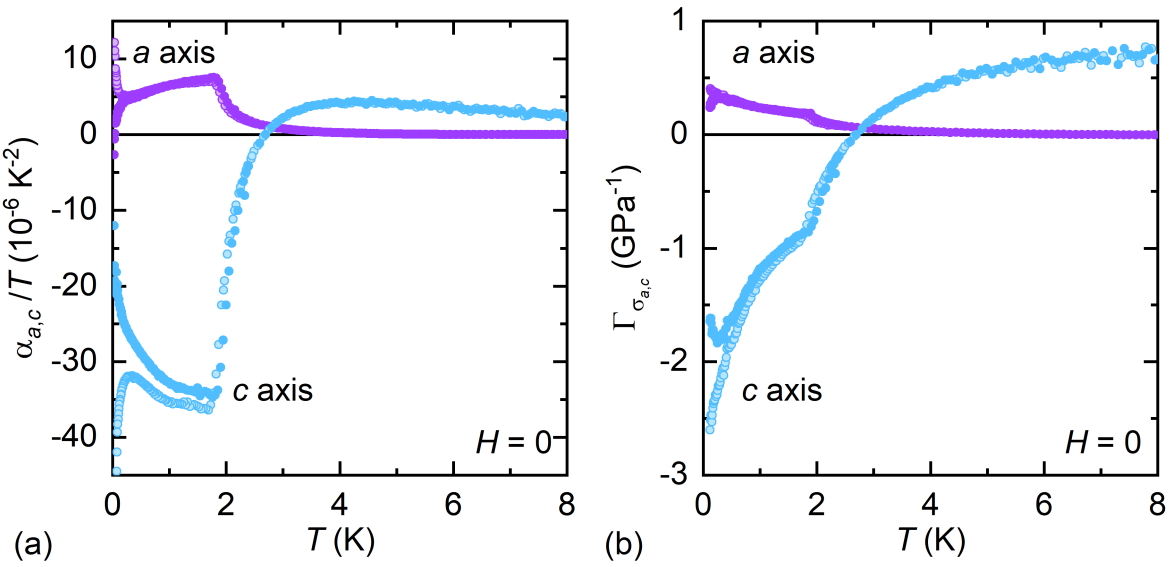

Figure 5.2: (a) Temperature dependence of the linear thermal expansion coefficients of $CePd_{0.95}Ni_{0.05}Al$ divided by T for both crystallographic directions in zero magnetic field.
(b) The corresponding Grüneisen ratios Γ_{σ_a} (purple) and Γ_{σ_c} (blue) as function of temperature at $H = 0$.
Full symbols represent measurements during heating and open symbols during cooling the sample.

5.1.2 $CePd_{0.95}Ni_{0.05}Al$ in Magnetic Field

As shown in fig. 5.3(a) with increasing magnetic field, the magnetic order in $CePd_{0.95}Ni_{0.05}Al$ is suppressed. At the critical field $\mu_0 H_c \approx 3.3\,\mathrm{T}$ (corresponds to the upper critical field of the AF_3 phase in pure CePdAl), α_a/T and α_c/T change their sign. The different anisotropy of $\partial S/\partial\sigma_i$ below and above H_c signals the change from a partially ordered to a field-polarized ground state. In contrast to the parent compound CePdAl, shown in fig. 4.9, the transition anomalies remain strongly broadened up to H_c and the sharp peaks of the AF_3 phase cannot be observed anymore. Similar to the zero-field data, the measurements in magnetic fields show extended hystereses with strong up- and downturns at low temperatures. These hystereses together with the broadening of the transition make it impossible to analyze the data near H_c with regard to a field-induced QCP.

Figure 5.3(b) shows a comparison of the linear to the volume thermal-expansion coefficients in zero field. As in CePdAl, the isotropic, hydrostatic pressure dependence of the entropy is significantly smaller than its uniaxial stress dependences. As for CePdAl, α_V/T is negative below T_N indicating that again hydrostatic pressure suppresses the magnetic order. At fields much larger than H_c [see fig. 5.3(c)], α_V/T finally approaches a small nearly constant value that is typical of a Fermi liquid.

To study the hysteretic behavior of $CePd_{0.95}Ni_{0.05}Al$ in more detail field-heated and field-cooled measurements at $H = 0$ and $\mu_0 H = 3\,\mathrm{T}$, near the critical field H_c, are shown in fig. 5.4. At $H = 0$ the hysteretic behavior seems to be more pronounced along the c axis than at $H = H_c$ where the data look like mirror images of each other. Although the hystereses appear at temperatures clearly beyond T_N, they might be related to the magnetic order. The hysteresis above T_N might be due to the pronounced short-range order probably associated with the frustration [18]. Furthermore, at fields higher than H_c the hysteretic behavior vanishes [see fig. 5.5(a)]. To illustrate this in 5.5(b) α_c/T measured at $T = 0.1\,\mathrm{K}$ during heating and cooling is plotted against the magnetic field. The difference between the field-cooled and field-heated measurements reaches its maximum just below the critical field where α_c/T changes its sign. Above $\approx 4\,\mathrm{T}$ the difference disappears nearly completely.

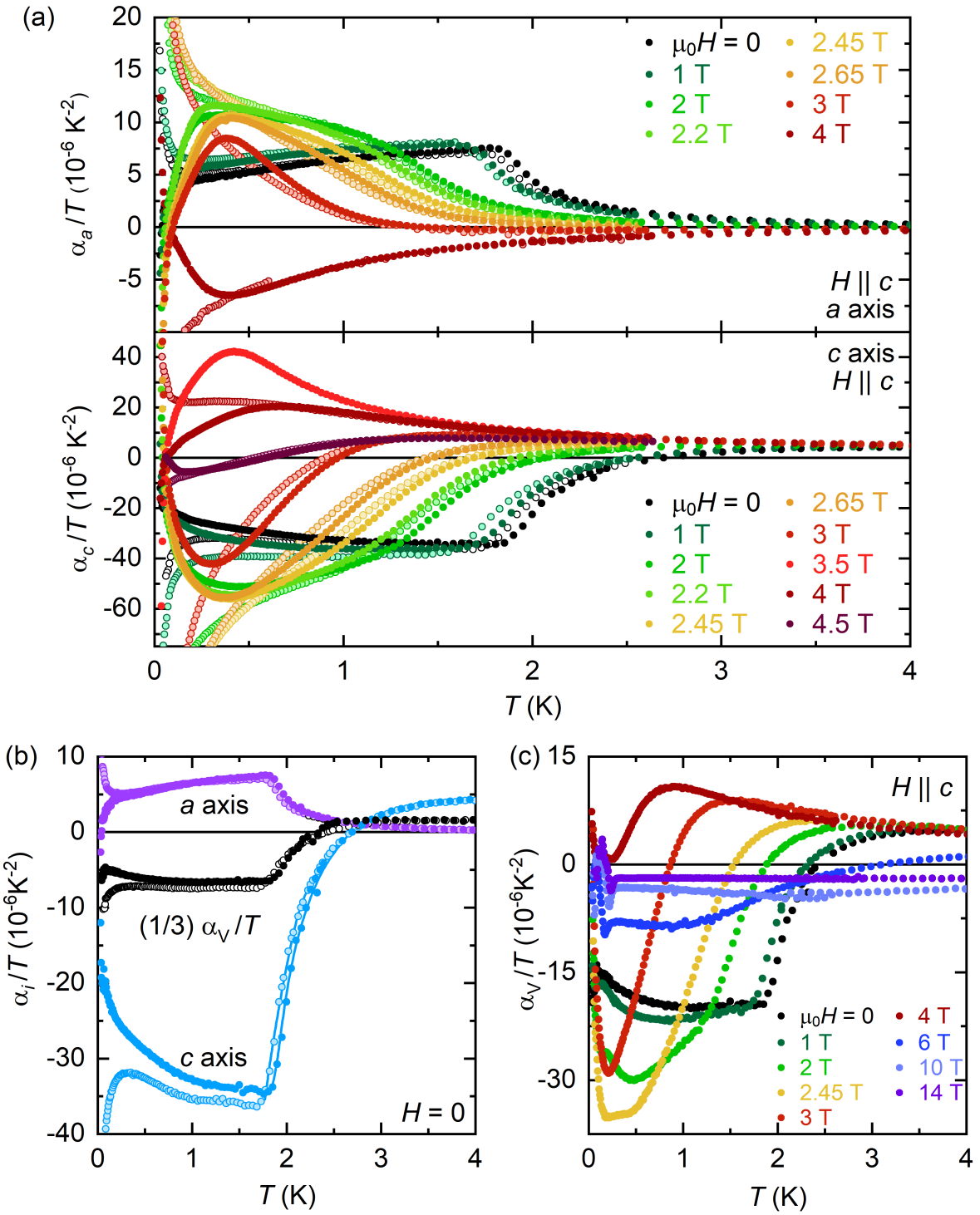

Figure 5.3: (a) Temperature dependence of the linear thermal-expansion coefficients of $CePd_{0.95}Ni_{0.05}Al$ divided by T, α_a/T and α_c/T, at different constant magnetic fields up to $\mu_0 H = 4\,\mathrm{T}$ applied along the c direction.
(b) Comparison of α_i/T with the volume thermal-expansion coefficient α_V divided by $3 \cdot T$ at $H = 0$.
(c) The volume thermal expansion α_V/T at different magnetic fields between $H = 0$ and $\mu_0 H = 14\,\mathrm{T}$ parallel to the c axis.
Full symbols represent measurements during heating and open symbols during cooling the sample. Lines are guides to the eye.

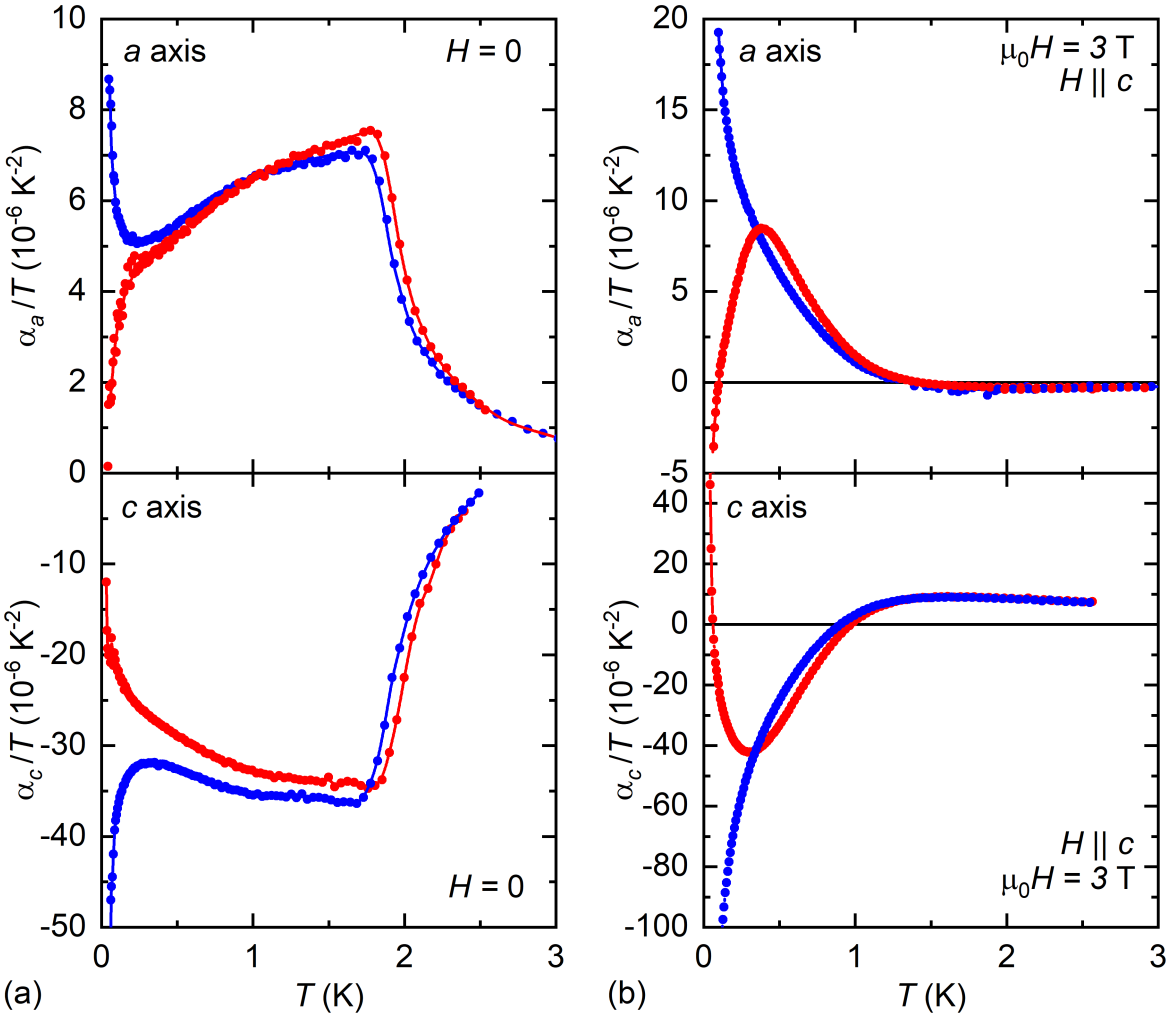

Figure 5.4: Comparison of the hysteresis of the thermal expansion coefficients $\alpha_{a,c}/T$ of $CePd_{0.95}Ni_{0.05}Al$ between cooling (blue data) and heating (red data) in zero field (a) and $\mu_0 H = 3\,\mathrm{T}$ (b).
Lines are guides to the eye.

A characteristic dependence of α_i typically develops when a pressure-dependent phase transition is crossed by varying a tuning parameter at low temperatures [22]. It is caused by the sign change of $\partial S/\partial p$ at the maximum of the accumulated entropy which arises at the phase transition. In our case H_c depends on pressure and thus the phase transition occurs at the field where α_c changes its sign if frustration effects are neglected. The latter can be assumed because at this field the magnetic order is suppressed by the field polarization of the magnetic moments just as in CePdAl.

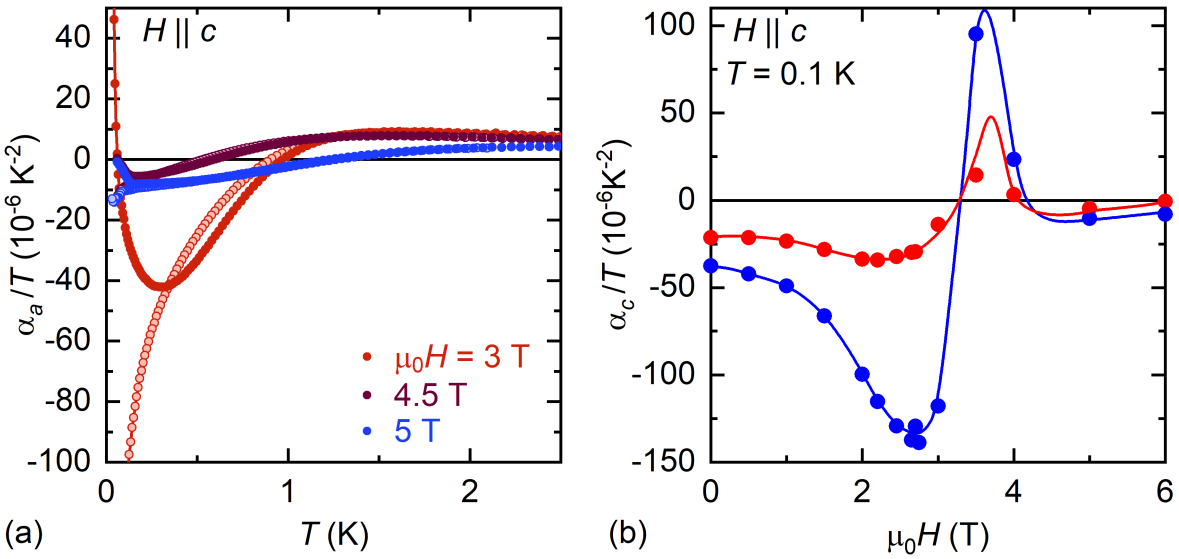

Figure 5.5: (a) Hysteresis in the thermal expansion coefficient α_a/T of $CePd_{0.95}Ni_{0.05}Al$ in different magnetic fields $\mu_0 H = 3\,\mathrm{T}$, $5.5\,\mathrm{T}$ and $6\,\mathrm{T}$. Full symbols indicate that the temperature was raised during the measurement, open symbol that it was lowered. (b) Field dependence of the thermal expansion coefficient α_c/T at $T = 0.1\,\mathrm{K}$. Red data indicates that the temperature was raised during the measurement, blue data that it was lowered. Lines are guides to the eye.

To look for additional phase transitions within the field range of the AF order as found in CePdAl [see chapter 4.1], magnetostriction measurements have been performed at low temperature [see fig. 5.6]. The data for increasing fields (red) were taken at $T = 100\,\mathrm{mK}$, the data for decreasing field (blue) was taken at $T = 30\,\mathrm{mK}$. Like the thermal expansion, the measurements show hystereses at $\mu_0 H < 4\,\mathrm{T}$ [see λ_c in fig. 5.6(a)] between measurements for increasing and decreasing magnetic field. Though the data shown here has been taken at different temperatures, this behavior has also been observed at different, but constant temperatures (not shown here) and therefore is not due to the temperature difference between 0.3 K and 0.3 K. For $T \leq 0.1\,\mathrm{K}$, as a function of H, two shallow peaks can be identified [see fig. 5.6(a) and (b)]. The peak at higher fields is close to H_c and is presumably related to the upper critical field of the AF order. The second peak at $\mu_0 H \approx 2.5\,\mathrm{T}$ might correspond to the transition between the AF_2 and AF_3 phase of CePdAl. Taking this resemblance to the parent compound seriously, these two peaks are generated by first-order transitions which have been smeared out due to the intrinsic Pd/Ni site disorder.

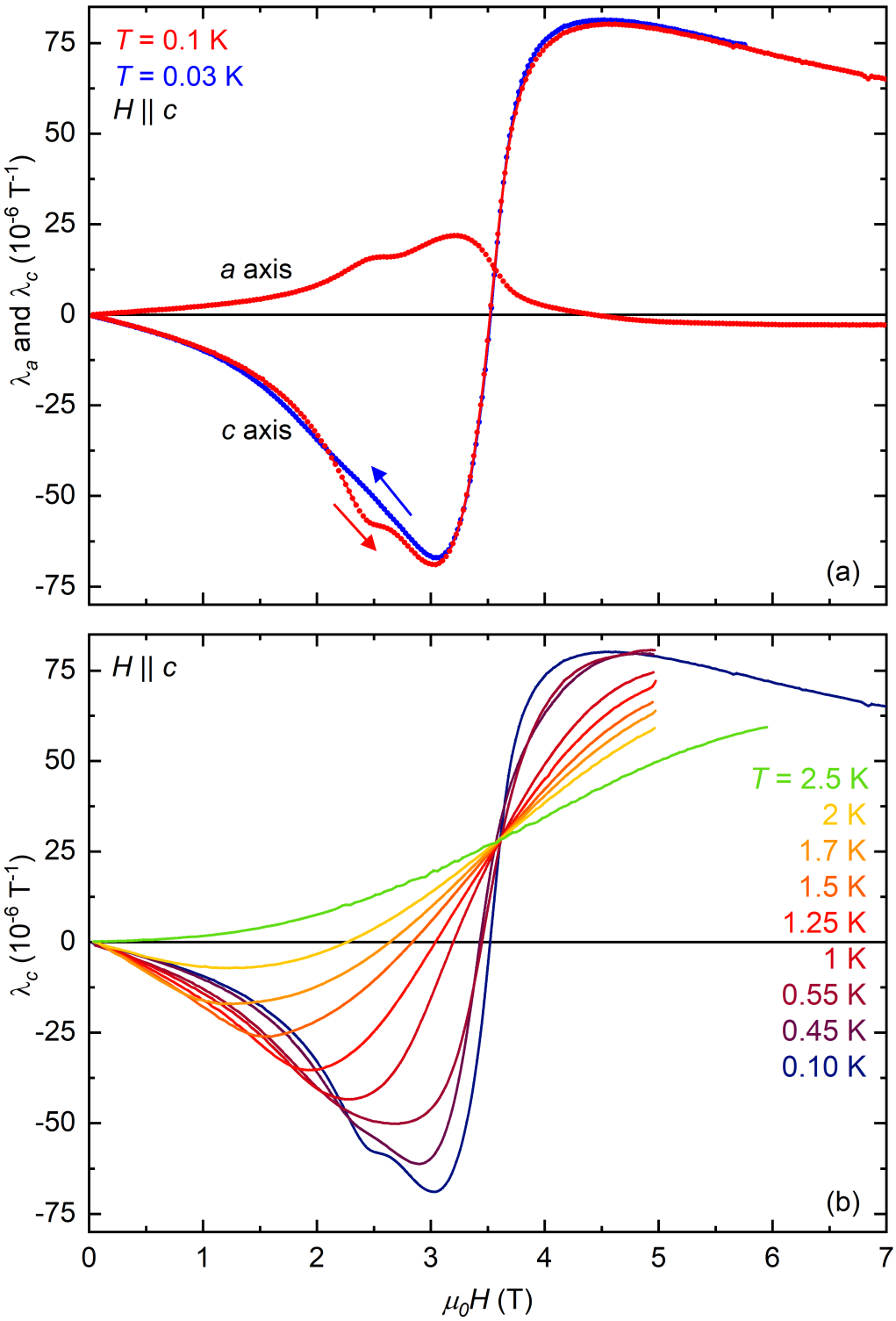

Figure 5.6: (a) The field dependent magnetostriction of $CePd_{0.95}Ni_{0.05}Al$ λ_a and λ_c, between $H = 0$ and $\mu_0 H = 7\,\mathrm{T}$ parallel to the c axis at $T = 0.1\,\mathrm{K}$ (red data) and $T = 0.03\,\mathrm{K}$ (blue data). The red lines also represent measurements during increasing the magnetic field, the blue lines during decreasing it.
(b) The magnetostriction along the c axis at different constant temperatures in the same field range. For clarity only the data for increasing fields are shown.

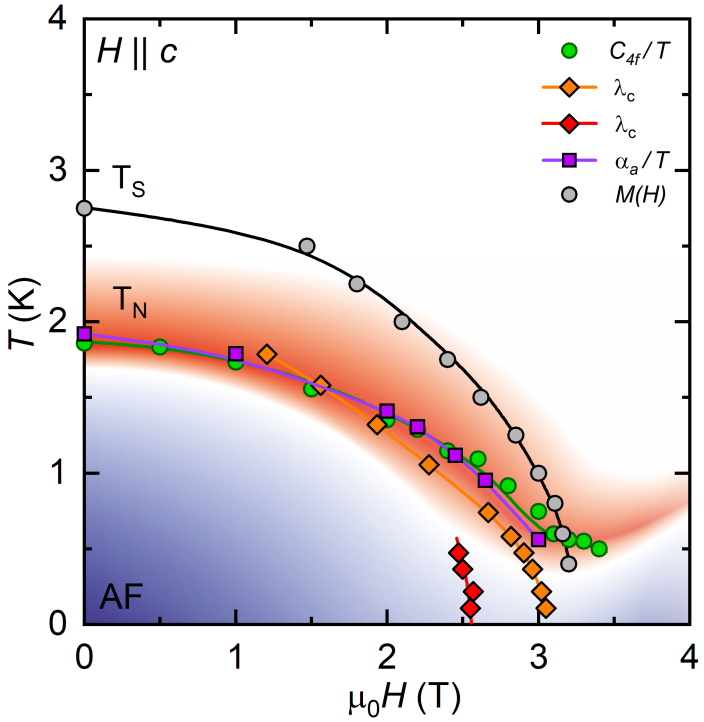

Figure 5.7: Magnetic phase diagram of $CePd_{0.95}Ni_{0.05}Al$ for fields along the c direction up to $\mu_0 H = 4\,\mathrm{T}$. Grey open circles (T_S) are derived from the maximum in the magnetization, green open circles (T_N) from the specific-heat transition anomaly (data taken from [37, 56]). The red and orange diamonds represent the shoulder and peak of λ_c, respectively. The purple squares are the steepest increase of α_a/T. The hysteretic behavior is illustrated by the shaded background: in the red shaded area the value of α_a/T is larger for heating the sample, in the blue shaded area for cooling. In areas with more intense colors the hysteresis is larger.

The thermal expansion and magnetostriction data of $CePd_{0.95}Ni_{0.05}Al$ can be summarized in a magnetic phase diagram depicted in fig. 5.7. As particularly at high fields the transitions are hardly distinguishable, the data points can only give a rough estimate of the phase boundaries. The position of the transition temperature was determined by the steepest increase of the slope of α_a/T, verified by differentiation, and is consistent with the peak position of the specific-heat data [37, 56]. The phase diagram resembles to some extent that of the stoichiometric parent compound. Clearly above T_N, the entropy exhibits likewise a maximum as a function of the magnetic field. The temperature of this maximum T_S seems to merge into the T_N line close to H_c. The position of the shallow peaks in $\lambda_a(H)$ and $\lambda_c(H)$ are marked by red and orange diamonds, respectively. The peak at higher fields closely reproduces the field dependence of T_N. The extended hysteresis is illustrated by the colored background.

The maximum of the hysteresis (red line) is observed close to T_N. Above $\mu_0 H \approx 4\,\mathrm{T}$, the magnetic order breaks down and the field-polarized ground state sets in.

To search for quantum-critical behavior the Grüneisen ratio has been calculated by using the specific-heat data from [37, 56]. The resulting values are plotted in fig. 5.8 as a function of T. The up- and downturns at the lowest temperatures due to the hystereses have been discussed above. At magnetic fields above $\mu_0 H = 2\,\mathrm{T}$ no transition signatures can be observed. The divergent temperature dependence and the sign change of Γ_{σ_a} and Γ_{σ_c} suggest the proximity to a field-induced QCP. In contrast, however, the divergences are apparently suppressed if the magnetic field is increased above $\approx 2\,\mathrm{T}$. This might be the result of a broadened high-field phase with first-order transitions, similar to CePdAl. Such discontinuous transitions would reduce the critical fluctuations even if chemical disorder lead to a slight broadening of the transitions.

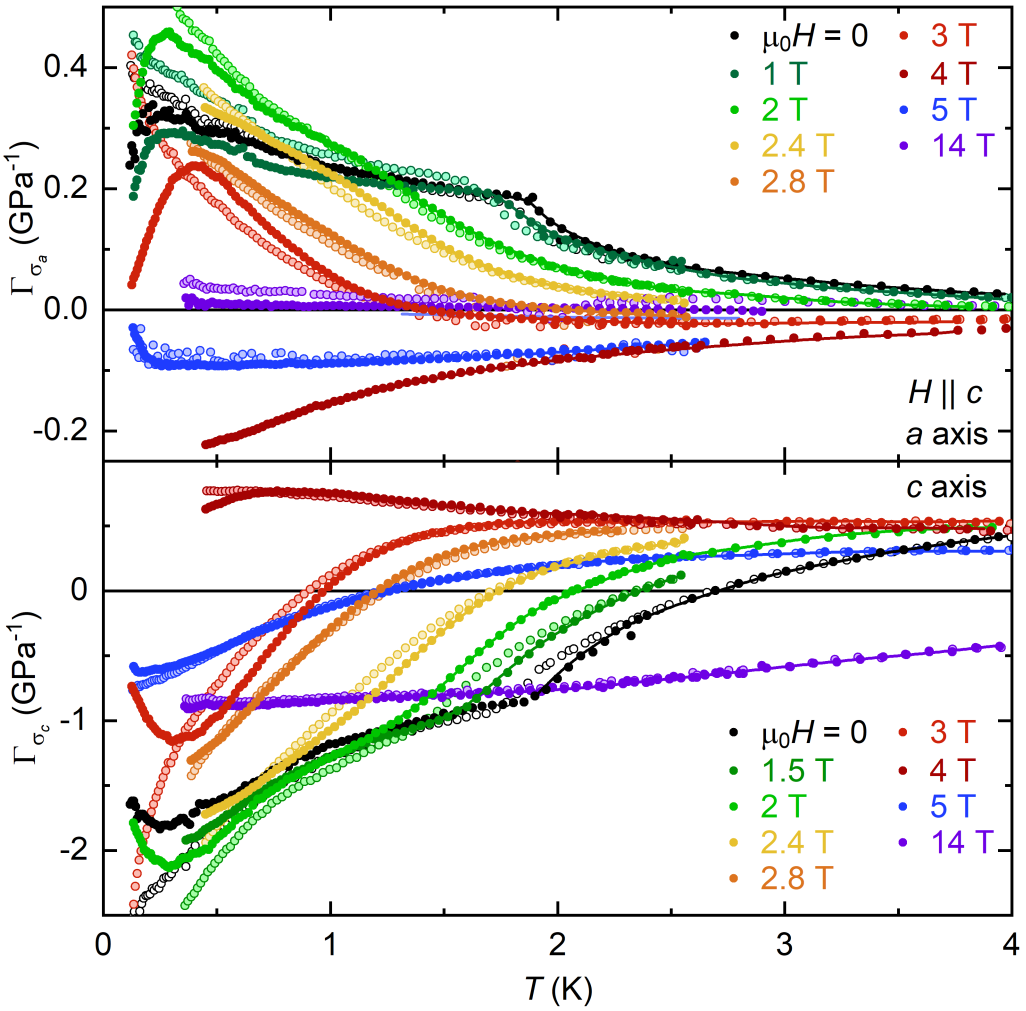

Figure 5.8: The Grüneisen ratios Γ_{σ_a} and Γ_{σ_c} of $CePd_{0.95}Ni_{0.05}Al$ as a function of temperature at various constant magnetic fields applied parallel to the c axis. Full symbols represent measurements during heating and open symbols during cooling the sample. Lines are guides to the eye.

5.2 $CePd_{0.90}Ni_{0.10}Al$

5.2.1 $CePd_{0.90}Ni_{0.10}Al$ at Zero Magnetic Field

Two different samples with a nominal Pd content of $x = 10\,\%$ were investigated. In the following they are named sample A or $x = 0.10\,\mathrm{A}$ and sample B or $x = 0.10\,\mathrm{B}$. Sample A was a bigger crystal than Sample B. Sample B was very brittle and broke during the measurement along the a axis, wherefore an exact determination of the sample length was not possible anymore. Hence, the absolute values of the thermal expansion of Sample B cannot directly be compared to those of Sample A. Moreover, as the remaining pieces of Sample B were to small after it broke, the c direction could not be measured. In the following most of the discussion will focus on sample A, with short comparisons to sample B when useful.

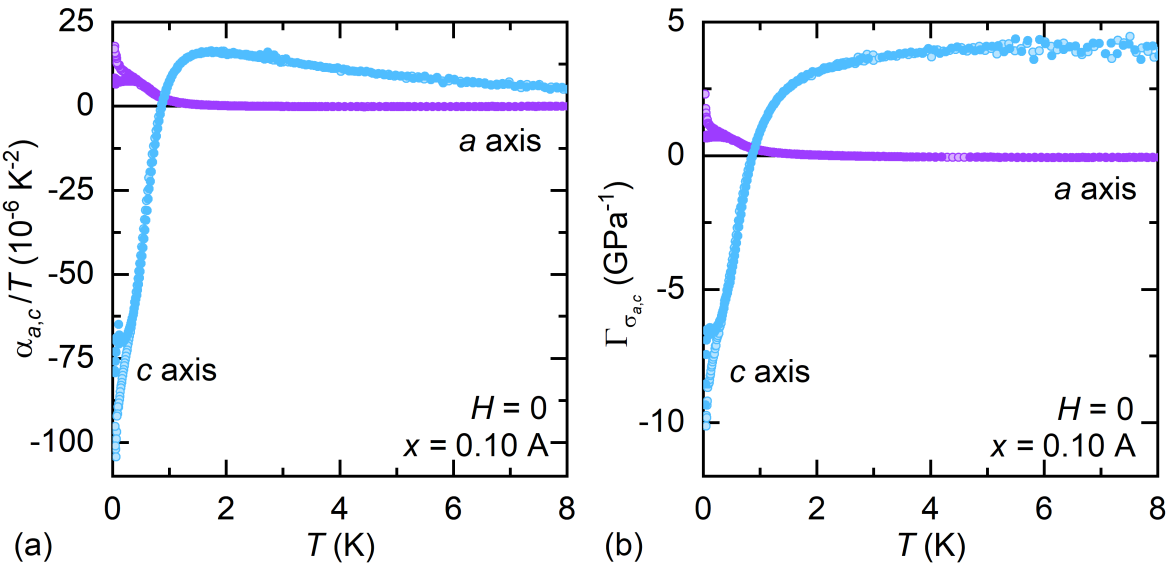

Figure 5.9: (a) Temperature dependence of the linear thermal expansion coefficients of $CePd_{0.90}Ni_{0.10}Al$ sample A divided by T for both crystallographic directions in zero magnetic field.
(b) The corresponding Grüneisen ratios Γ_{σ_a} (purple) and Γ_{σ_c} (blue) as function of temperature at $H = 0$.
Full symbols represent measurements during heating and open symbols during cooling the sample. The specific heat data to calculate the Grüneisen ratios are taken from Ref. [37].

The thermal-expansion coefficients along both axes, α_a/T and α_c/T, of $CePd_{0.90}Ni_{0.10}Al$ sample A at $H = 0$ are plotted in fig. 5.9(a). In neither case is a clear transition to the antiferromagnetic order visible, but the specific-heat coefficient C_{4f}/T [not shown here, see [37]] has a clear kink at $T \approx 0.6\,\mathrm{K}$ (comparable to the temperature of the steepest slope in α_C/T): At this temperatures α_a/T tends to a T-independent behavior and α_c/T shows a slight change in slope. At lower temperatures both α_a and α_c show again a distinct difference between cooling (open symbols) and heating (full symbols) the sample, though not as pronounced as in $CePd_{0.95}Ni_{0.05}Al$. The Grüneisen ratios at zero field $\Gamma_{\sigma_{a,c}}$ are plotted in fig. 5.9(b). In both cases the data is nearly constant at higher temperatures. Γ_{σ_a} increases only slightly towards low temperatures whereas Γ_{σ_c} exhibits a sign change and a steep decrease, similar to $CePd_{0.95}Ni_{0.05}Al$.

5.2.2 $CePd_{0.90}Ni_{0.10}Al$ in Magnetic Field

In $CePd_{0.90}Ni_{0.10}Al$ the magnetic order is suppressed with increasing magnetic field, as both linear thermal-expansion coefficients, α_a/T and α_c/T, exhibit a sign change at H_c between $\mu_0 H = 1.5\,\mathrm{T}$ and $\mu_0 H = 2\,\mathrm{T}$ at low temperatures as can be clearly seen in fig. 5.13. As for $CePd_{0.95}Ni_{0.05}Al$ the different anisotropies of $\partial S/\partial\sigma_i$ for low and high fields indicate the change from the partially ordered state to the field polarized state. The evolution of the hysteresis with increasing field is comparable to that in $CePd_{0.95}Ni_{0.05}Al$, rendering it impossible to identify a possible field-induced QCP. Fig. 5.10(a) shows the complete data set of the temperature dependence of α_a/T and α_c/T for different fixed magnetic fields up to 4 T, i.e. well above H_c.

Figure 5.10(b) shows a comparison of the volume and linear thermal-expansion coefficients in zero field. $CePd_{0.90}Ni_{0.10}Al$ continues the trend started at $CePd_{0.95}Ni_{0.05}Al$ as $(1/3) \cdot |\alpha_V/T|$ now exceeds $|\alpha_a/T|$ because of the large absolute value of α_c/T. Again, as α_V/T is negative, hydrostatic pressure suppresses the magnetic order and for $H > H_c$, α_V/T becomes constant at very small absolute values, typical of a Fermi-liquid [see fig. 5.10(c)].

Figure 5.11 shows α_c/T of sample B in magnetic fields between $H = 0$ and $\mu_0 H = 6\,\mathrm{T}$. The data is comparable to sample A with small differences in the magnetic-field behavior. The sign change in α_c/T due to the suppression of magnetic order is shifted to somewhat higher fields ($\mu_0 H_c \approx 2.1\,\mathrm{T}$) and at $\mu_0 H = 4\,\mathrm{T}$, α_c/T is not constant yet. Therefore we assume that sample B has a slightly lower Ni content than sample A.

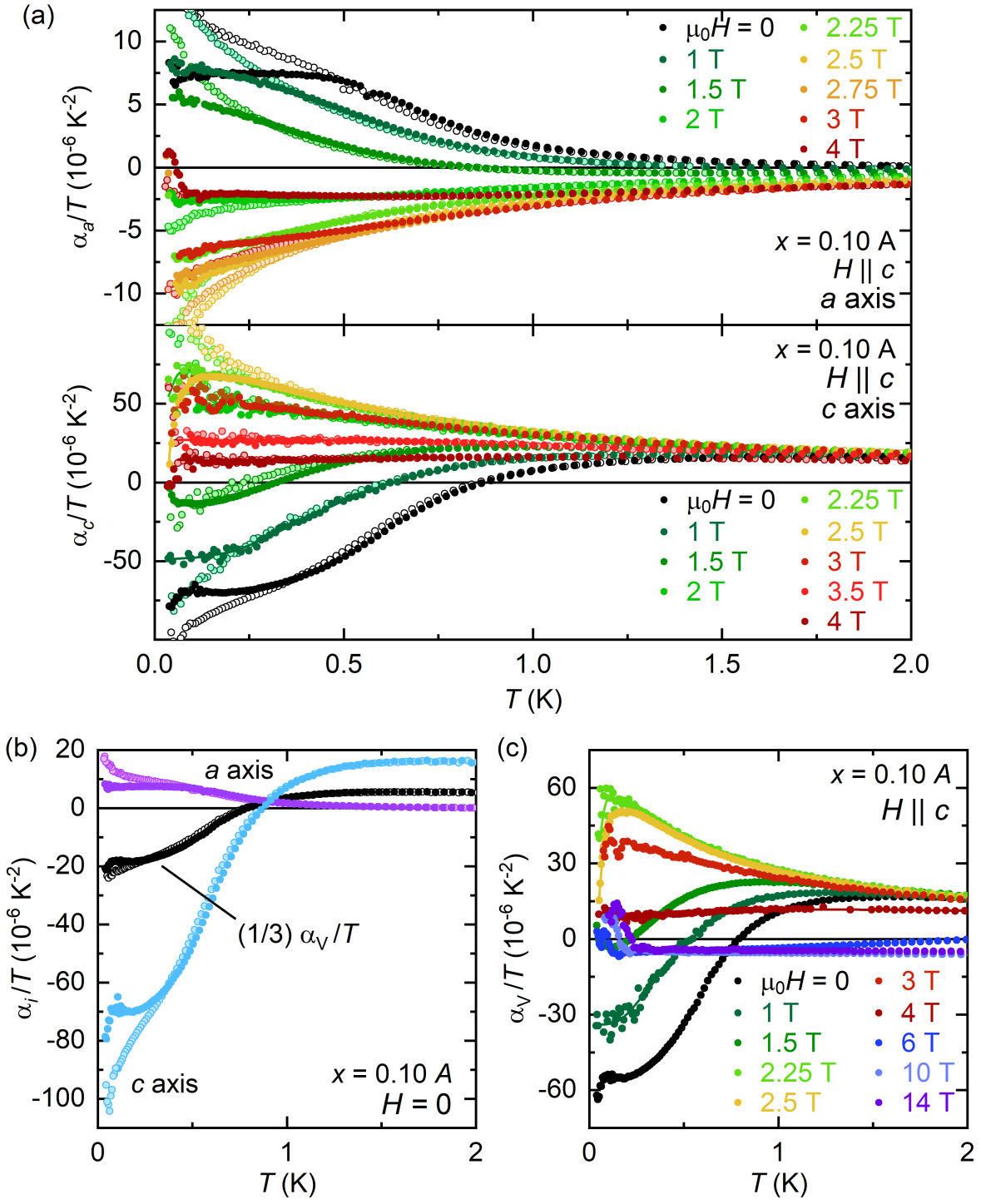

Figure 5.10: (a) Temperature dependence of the linear thermal-expansion coefficients of $CePd_{0.90}Ni_{0.10}Al$ sample A divided by T, α_a/T and α_c/T, at different constant magnetic fields up to $\mu_0 H = 4\,\mathrm{T}$ applied along the c direction.
(b) Comparison of α_i/T with the volume thermal-expansion coefficient α_V divided by $3 \cdot T$ at $H = 0$.
(c) The volume thermal expansion α_V/T at different magnetic fields between $H = 0$ and $\mu_0 H = 14\,\mathrm{T}$ parallel to the c axis.
Full symbols represent measurements during heating and open symbols during cooling the sample. Lines are guides to the eye.

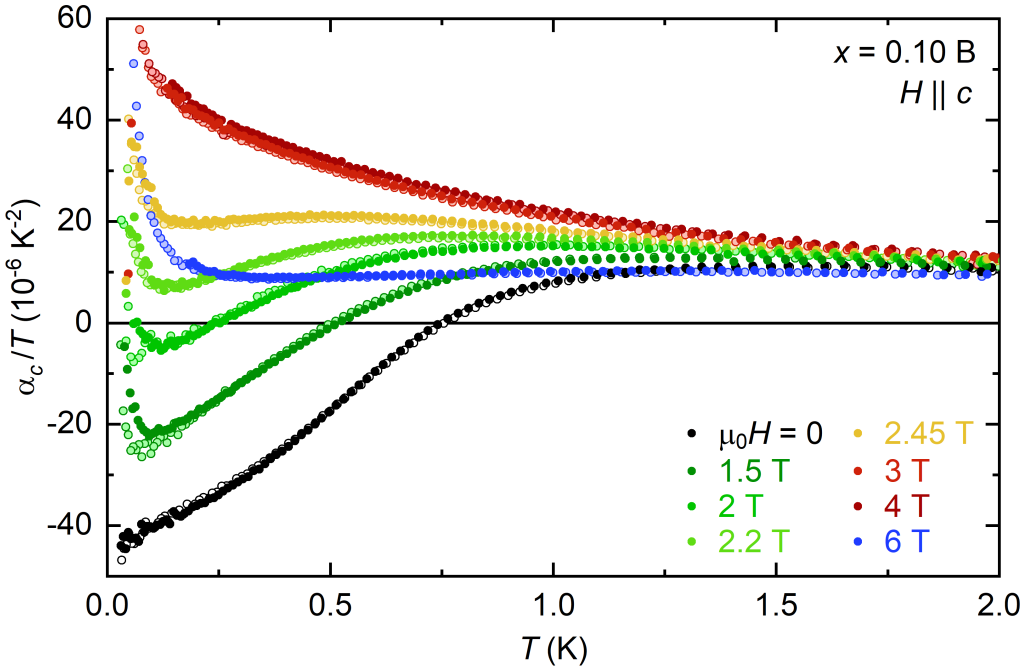

Figure 5.11: Temperature dependence of the linear thermal-expansion coefficient α_c/T of $CePd_{0.90}Ni_{0.10}Al$ sample B at different constant magnetic fields up to $\mu_0 H = 6\,\mathrm{T}$ applied along the c direction.
Full symbols represent measurements during heating and open symbols during cooling the sample. Lines are guides to the eye.

To compare the hysteretic behavior of $CePd_{0.90}Ni_{0.10}Al$ with $CePd_{0.95}Ni_{0.05}Al$, field-heated and field-cooled measurements at $H = 0$ and $\mu_0 H = 3.0$ or $2.5\,\mathrm{T}$ are shown in fig. 5.12. For sample A at zero field the hysteresis is more pronounced for α_a/T than for α_c/T [see fig. 5.12(a)]. Above the critical field H_c, i.e., at $\mu_0 H = 3\,\mathrm{T}$, the hysteresis is significantly smaller than at $H = 0$ [see fig. 5.12(b)]. The same behavior has been observed for $CePd_{0.95}Ni_{0.05}Al$. Suprisingly, sample B [see fig. 5.12(c) and (d)] does not show any sign of a hysteresis between heating and cooling. This results presumably from a different Ni distribution [Pd(1) and Pd(2) sites] in this specific sample, as it was a lot smaller than the other crystals and very brittle at room temperature.

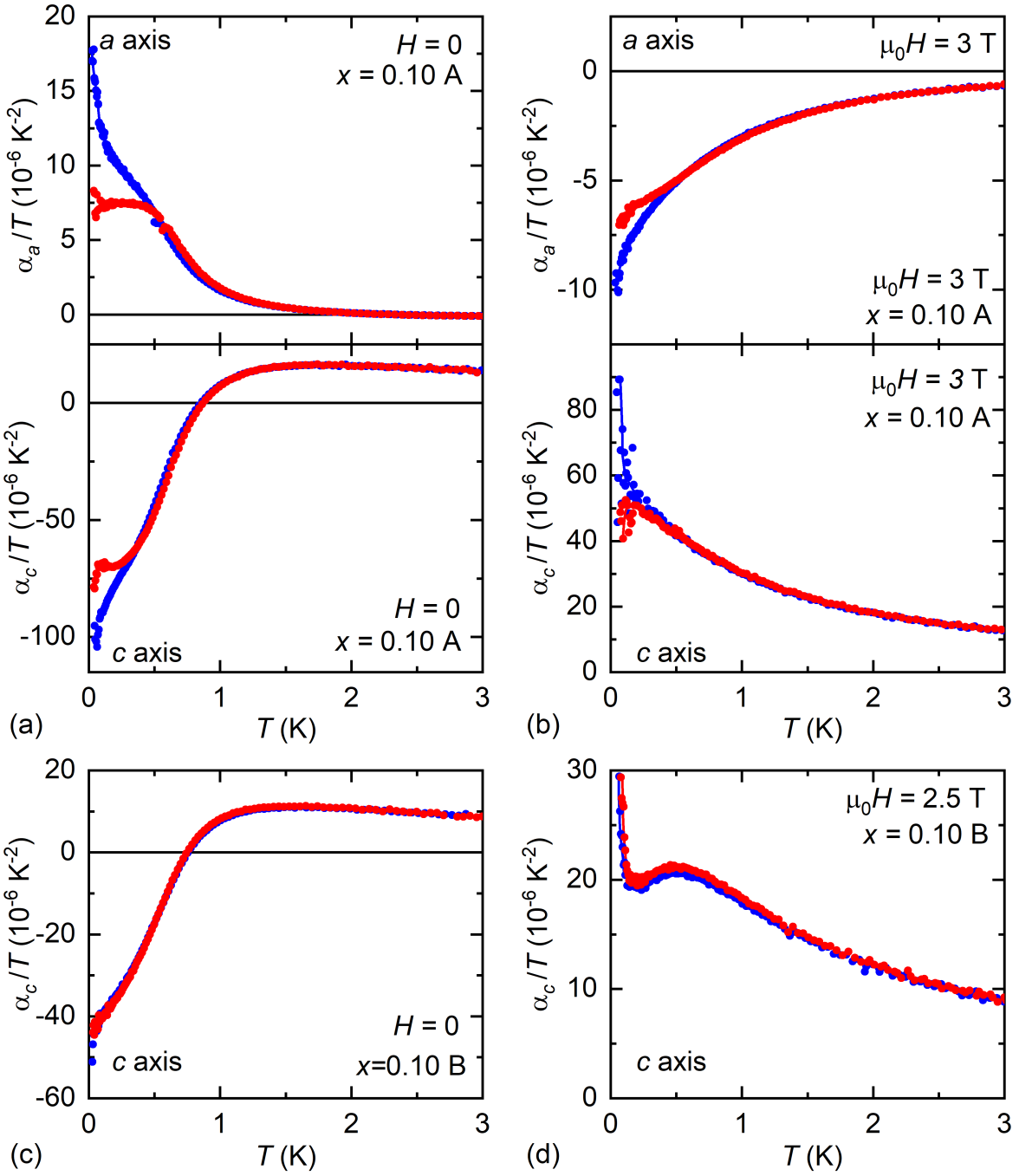

Figure 5.12: Comparison of the hysteresis of the thermal expansion coefficients $\alpha_{a,c}/T$ of $CePd_{0.90}Ni_{0.10}Al$ sample A ((a) and (b)) and B ((c) and (d)) between cooling (blue data) and heating (red data) in zero field ((a) and (c)) and $\mu_0 H = 3\,\mathrm{T}$ and $\mu_0 H = 2.5\,\mathrm{T}$ ((b) and (d)), respectively.
Lines are guides to the eye.

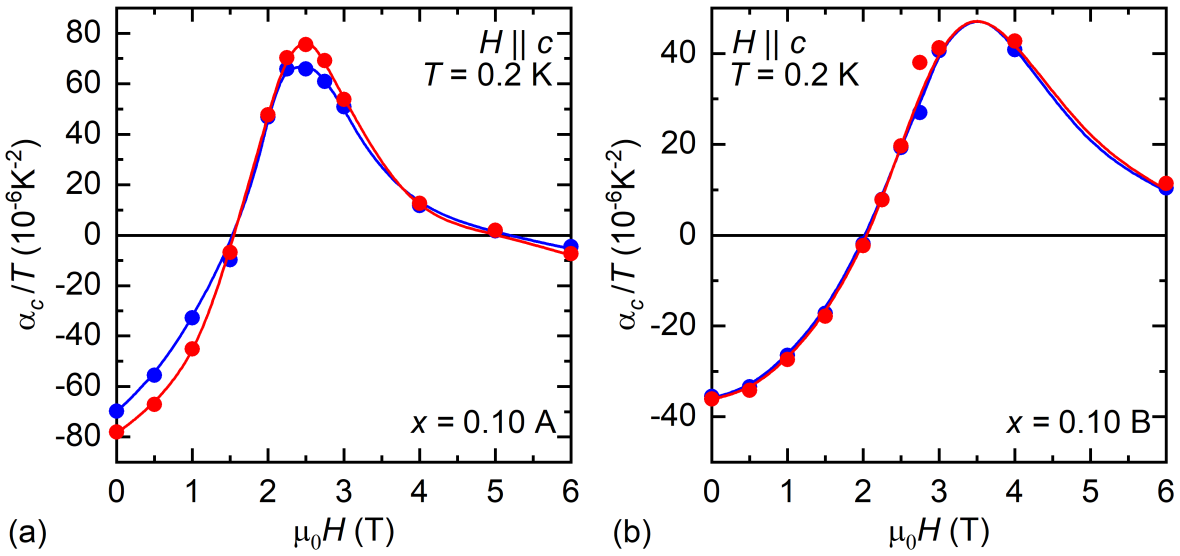

Figure 5.13: Field dependence of the thermal expansion coefficient α_c/T at $T = 0.1\,\mathrm{K}$ for $CePd_{0.90}Ni_{0.10}Al$ sample A and B. Red data indicates that the temperature was raised during the measurement, blue data that it was lowered. Lines are guides to the eye.

In figure 5.13 the field dependence of α_c/T of $CePd_{0.90}Ni_{0.10}Al$ A and B is plotted at $T = 0.2\,\mathrm{K}$ for heating and cooling. The same hysteretic behavior as above can be observed. More importantly the data resembles the S-shaped pressure dependence of $CePd_{0.95}Ni_{0.05}Al$ [see fig 5.5] albeit broadened and shifted to lower fields. It similarly indicates that H_c depends on pressure and that the phase transition occurs at the field where α_c/T changes its sign when the frustration effects are suppressed because of the field polarization.

To study the evolution of the metamagnetic phase transitions within the AF order with increasing Ni content, additional magnetostriction measurements have been performed for $CePd_{0.90}Ni_{0.10}Al$ A and B. Figure 5.14 shows λ_a and λ_c at $T = 0.1\,\mathrm{K}$ for sample A and sample B, respectively. The heating data (red line) for sample B was taken at $T = 0.2\,\mathrm{K}$. In contrast to $CePd_{0.95}Ni_{0.05}Al$, here only one peak can be identified in both directions, presumably related to the critical field of the AF order. The data show no signs of the metamagnetic transitions below H_c.

Due to the lack of clear signatures of transitions in the linear thermal-expansion coefficients $\alpha_{a,c}/T$ as well as in the magnetostriction coefficients $\lambda_{a,c}$ we refrain from constructing a magnetic phase diagram for $CePd_{0.90}Ni_{0.10}Al$.

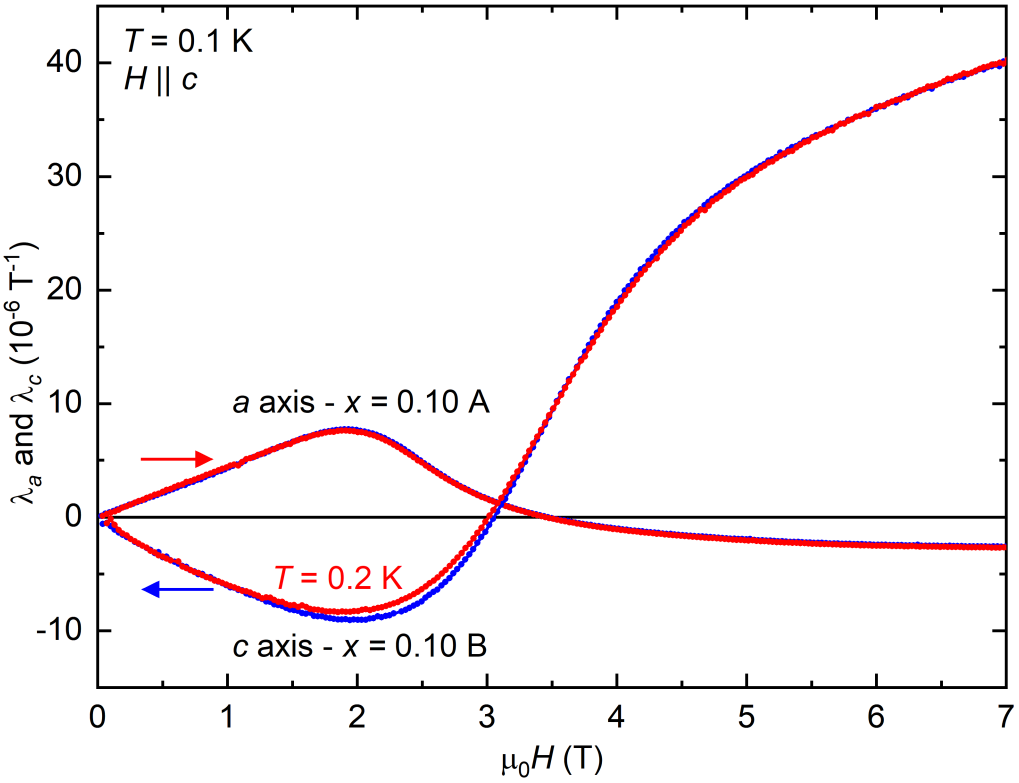

Figure 5.14: Field dependent magnetostriction $\lambda_{a,c}$ of $CePd_{0.90}Ni_{0.10}Al$ along the a axis for sample A and the c axis for sample B between $H = 0$ and $\mu_0 H = 7\,\mathrm{T}$ parallel to the c axis at $T = 0.1\,\mathrm{K}$ and $T = 0.2\,\mathrm{K}$ for the increasing field of sample B. The red lines represent measurements during increasing magnetic field, the blue lines during decreasing.

Figure 5.15 shows the Grüneisen ratios for $CePd_{0.90}Ni_{0.10}Al$ sample A as a function of T calculated by using the specific-heat data from [37, 56]. The effects of the hystereses have been discussed above. Similar to the linear thermal-expansion data, no transition signatures can be observed. Comparable to $CePd_{0.95}Ni_{0.05}Al$ the temperature dependence and the sign change of Γ_{σ_a} and Γ_{σ_c} suggest the proximity to a field-induced QCP. However, the divergences are suppressed when the magnetic field is increased to above $\approx 1\,\mathrm{T}$.

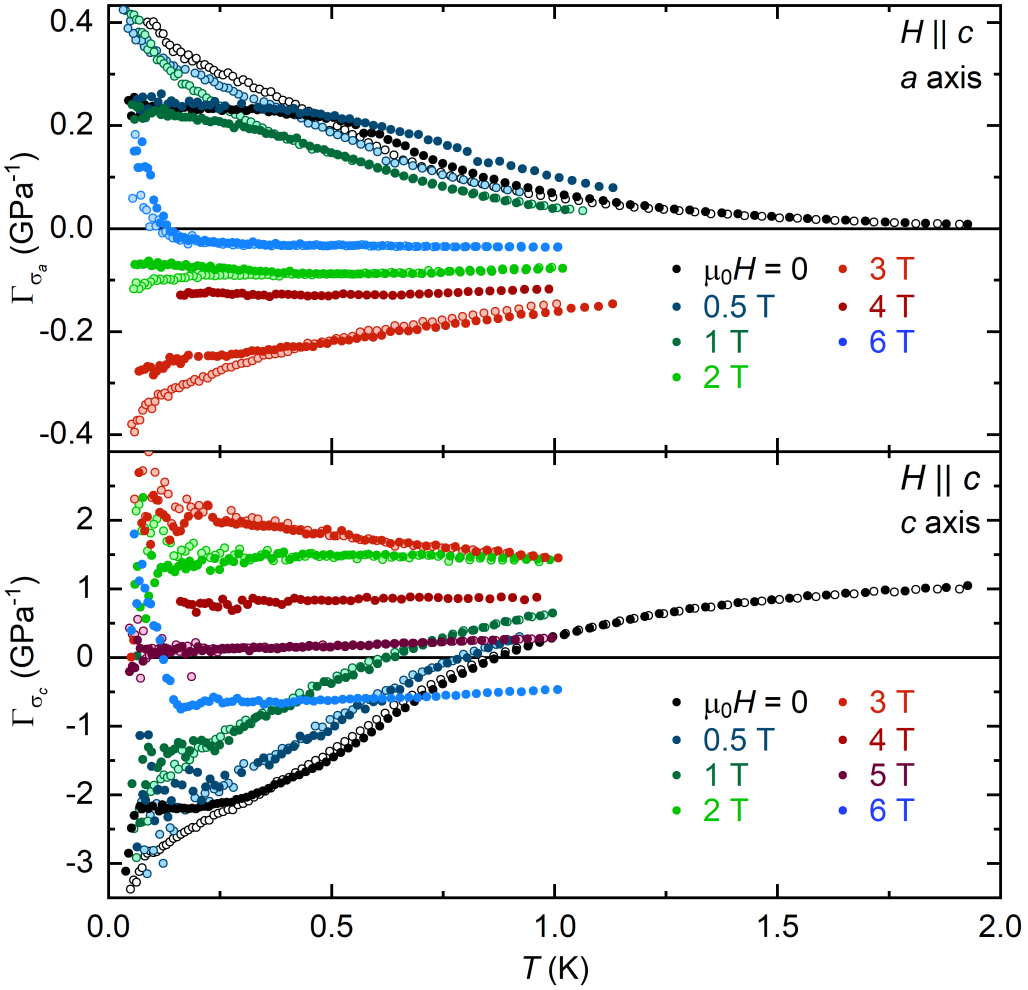

Figure 5.15: The Grüneisen ratios Γ_{σ_a} and Γ_{σ_c} of $CePd_{0.90}Ni_{0.10}Al$ sample A as a function of temperature at various constant magnetic fields applied parallel to the c axis.
Full symbols represent measurements during heating and open symbols during cooling the sample. Lines are guides to the eye.

5.3 $CePd_{0.86}Ni_{0.14}Al$

5.3.1 $CePd_{0.86}Ni_{0.14}Al$ at Zero Magnetic Field

The thermal-expansion coefficients along the a and c axes of $CePd_{0.86}Ni_{0.14}Al$ are plotted in fig. 5.16(a). In both cases no transition to the antiferromagnetic order is visible and also the specific heat coefficient C_{4f}/T [fig. 5.16(c)] does not show a transition anomaly. α_a/T as well as C_{4f}/T exhibit a strong increase to low temperatures, similar to the divergence expected for the approach to a QCP by temperature. On the other hand, α_c/T also increases strongly but still has a downturn with a (possible) sign change to lowest temperatures, right at the lower limit of our experimental temperature range. This can also be seen in the logarithmic representation of the specific heat coefficient [see inset of fig. 5.16(c)] by its deviation from linear behavior (dashed line) to lowest temperatures. Hence, we cannot rule out the possible onset of magnetic order at lowest temperatures.

In fig. 5.16(b) the Grüneisen ratios $\Gamma_{\sigma_{a,c}}$ at zero field for both directions are plotted. In both cases the data is mostly constant at higher temperatures, with a huge difference in the absolute values. Below $T = 1\,\mathrm{K}$, Γ_{σ_a} increases slightly whereas Γ_{σ_c} strongly decreases with the same possible sign change to lowest temperatures as α_c/T.

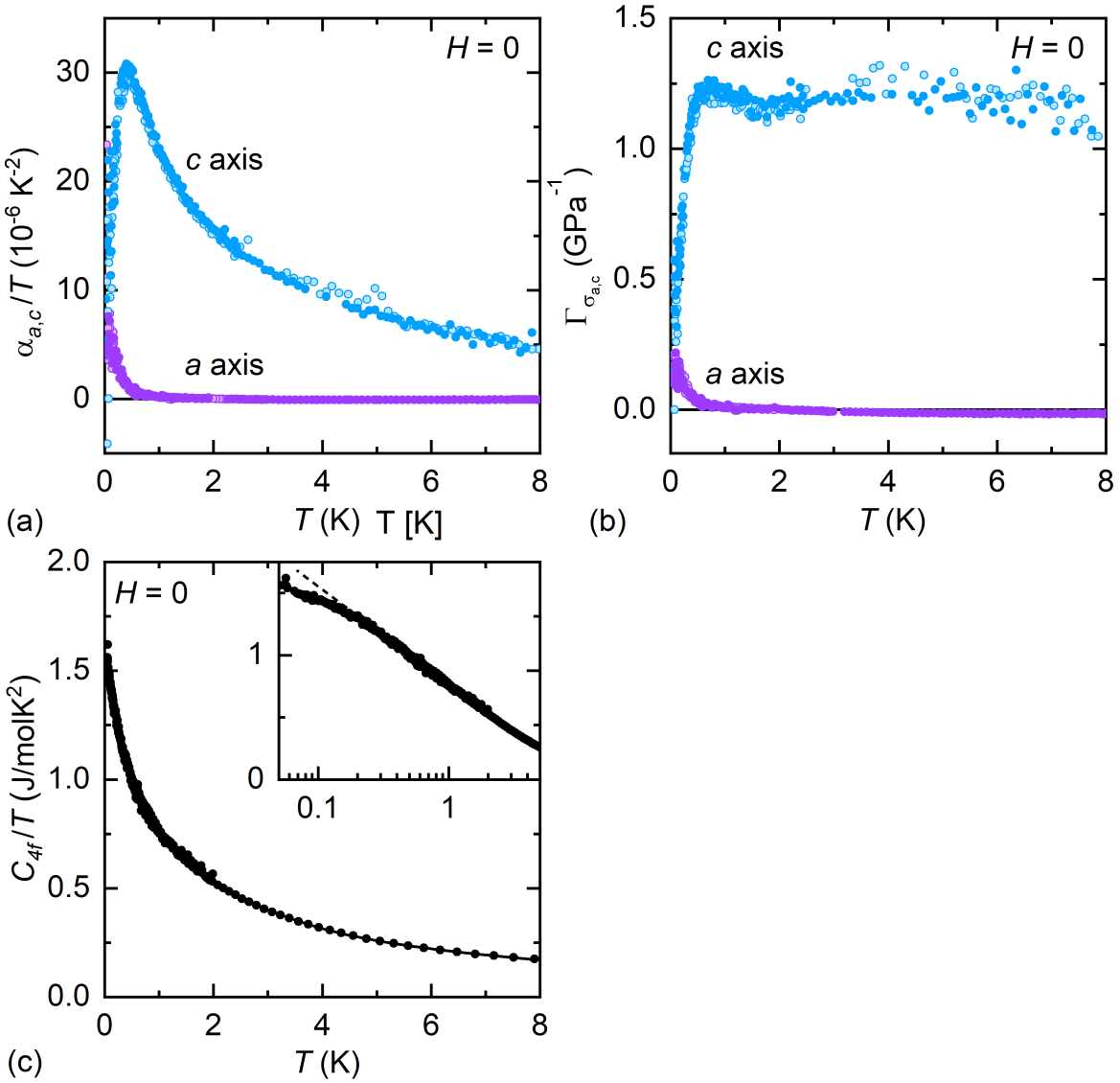

Figure 5.16: (a) Temperature dependence of the linear thermal expansion coefficients of $CePd_{0.86}Ni_{0.14}Al$ divided by T for both crystallographic directions in zero magnetic field.
(b) The corresponding Grüneisen ratios Γ_{σ_a} (purple) and Γ_{σ_c} (blue) as function of temperature at $H = 0$.
(c) The corresponding specific-heat coefficient C_{4f}/T as function of temperature at $H = 0$ (taken from Ref. [37]). The inset shows the same data plotted on a logarithmic scale. The dashed line represents the linear extension of the data to lowest temperatures.
Full symbols represent measurements during heating and open symbols during cooling the sample.

5.3.2 $CePd_{0.86}Ni_{0.14}Al$ in Magnetic Field

Figure 5.17(a) shows the linear thermal-expansion coefficients α_a/T and α_c/T in magnetic fields up to $\mu_0 H = 4\,\mathrm{T}$. While α_a/T exhibits a sign change just above $\mu_0 H = 1\,\mathrm{T}$ no such behavior can be observed in α_c/T. A possible explanation for this is that $CePd_{0.86}Ni_{0.14}Al$ is located just at the edge, but still in the AF ordered phase. Moreover, no hysteresis between cooling (open symbols) and heating (full symbols) is visible as observed in the behavior of CePdAl with smaller Ni content.

Figure 5.17(b) shows a comparison of the volume and linear thermal-expansion coefficients in zero field. $(1/3) \cdot |\alpha_V/T|$ now is by far larger than $|\alpha_a/T|$ as the latter has become close to zero for higher temperatures. Still α_c/T dominates the linear as well as the volume thermal expansion. With increasing magnetic field [see fig. 5.17(c)] α_V/T at first diverges to low temperatures and then falls down to constant, low absolute values in the Fermi-Liquid state at high fields.

Figure 5.18 shows the magnetostriction data for $CePd_{0.86}Ni_{0.14}Al$ at $T = 0.1\,\mathrm{K}$ for increasing field (red line) and at $T = 0.2\,\mathrm{K}$ for decreasing field (blue line). In contrast to $CePd_{0.90}Ni_{0.10}Al$, λ_c is positive in the whole field range and has no minimum. The behavior of λ_a, though, is comparable to $CePd_{0.90}Ni_{0.10}Al$ albeit shifted to lower fields and absolute values. Therefore, the difference in the critical behavior of α_a/T and α_c/T is also reflected in λ_a and λ_c.

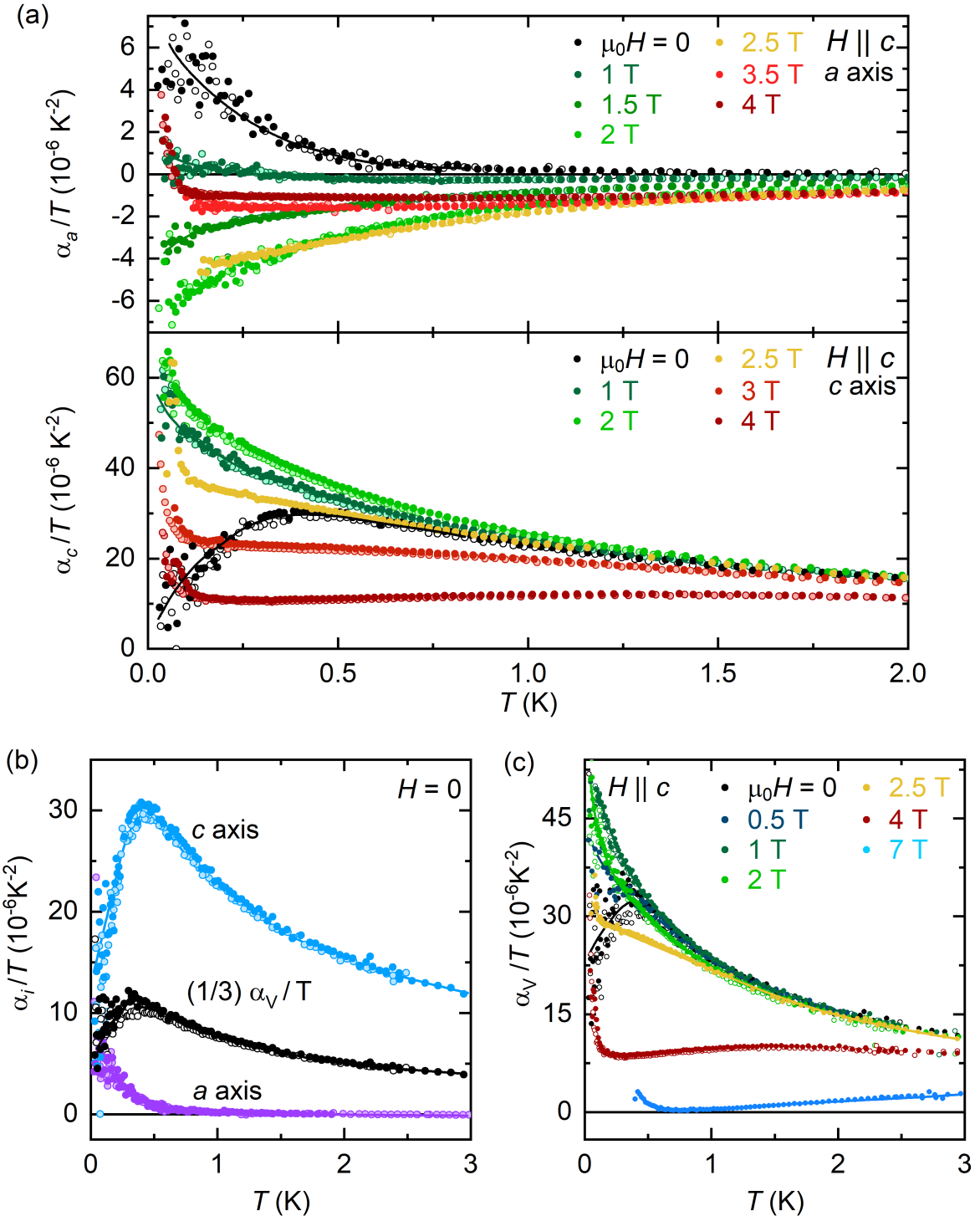

Figure 5.17: (a) Temperature dependence of the linear thermal-expansion coefficients of $CePd_{0.86}Ni_{0.14}Al$ divided by T, α_a/T and α_c/T, at different constant magnetic fields up to $\mu_0 H = 4\,\mathrm{T}$ applied along the c direction.
(b) Comparison of α_i/T with the volume thermal-expansion coefficient α_V divided by $3 \cdot T$ at $H = 0$.
(c) The volume thermal expansion α_V/T at different magnetic fields between $H = 0$ and $\mu_0 H = 7\,\mathrm{T}$ parallel to the c axis.
Full symbols represent measurements during heating and open symbols during cooling the sample. Lines are guides to the eye.

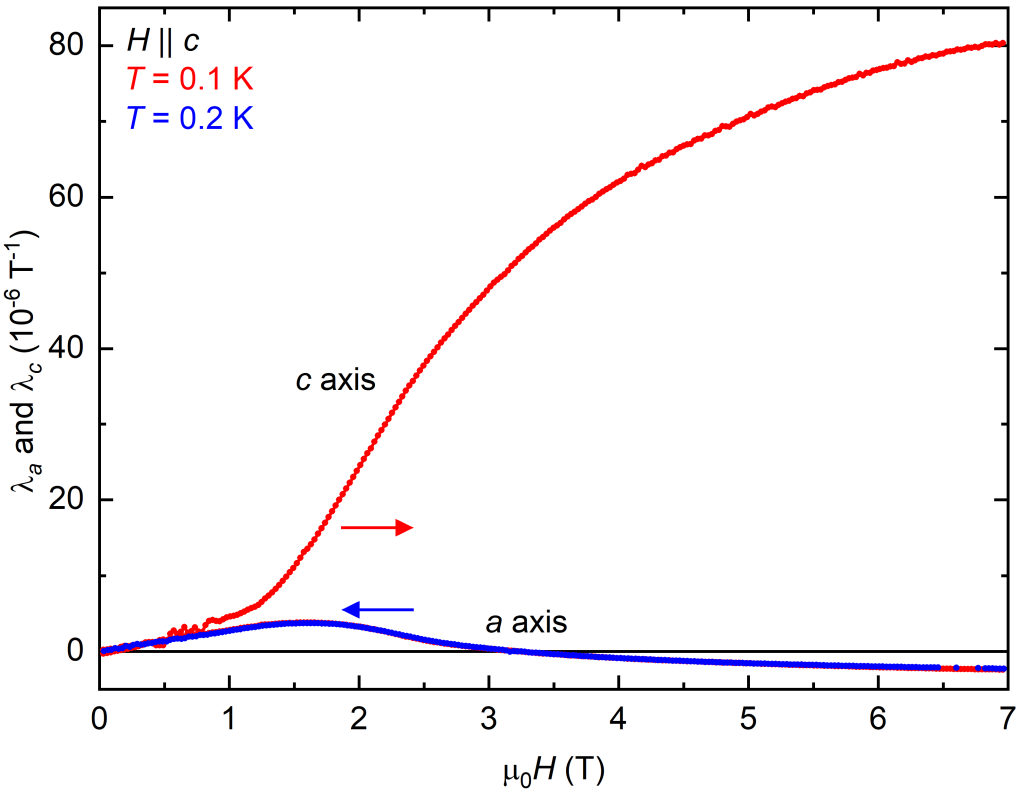

Figure 5.18: Field dependent magnetostriction of $CePd_{0.86}Ni_{0.14}Al$ along both crystallographic axes, λ_a and λ_c, between $H = 0$ and $\mu_0 H = 7\,\mathrm{T}$ parallel to the c axis at $T = 0.1\,\mathrm{K}$ (red data) and $T = 0.2\,\mathrm{K}$ (blue data). The red lines also represent measurements during increasing the magnetic field, the blue lines during decreasing.

Figure 5.19 shows the Grüneisen ratios for $CePd_{0.86}Ni_{0.14}Al$ as a function of T calculated by using the specific heat data from [37, 56]. Though no clear AF phase could be observed in $CePd_{0.86}Ni_{0.14}Al$, the divergence of Γ_{σ_a} and Γ_{σ_c} as well as the sign change of Γ_{σ_c} are typical signs for the proximity to a field-induced QCP. Again, a possible explanation for this behavior could be given by the chemical site disorder introduced by the Ni substitution leading to inhomogeneities in the sample.

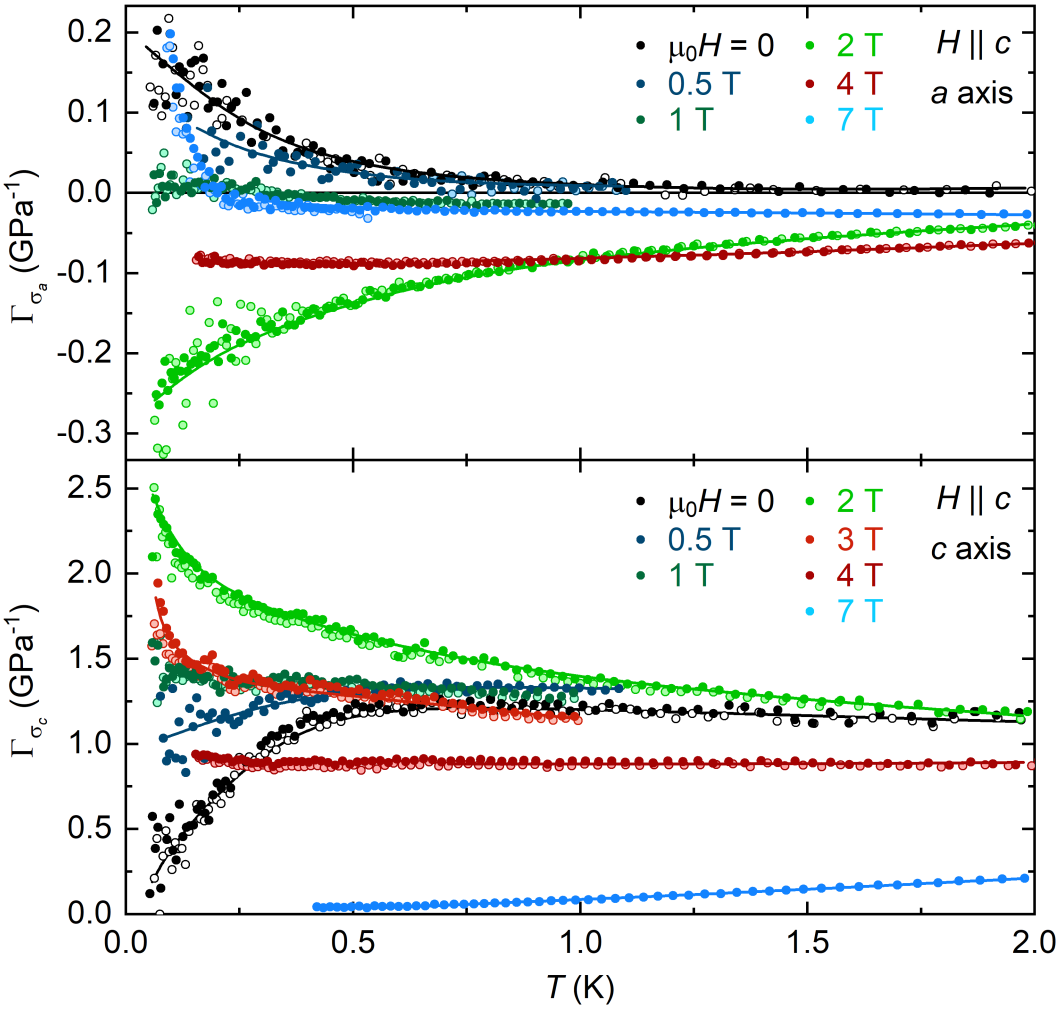

Figure 5.19: The Grüneisen ratios Γ_{σ_a} and Γ_{σ_c} of $CePd_{0.86}Ni_{0.14}Al$ as a function of temperature at various constant magnetic fields applied parallel to the c axis. Full symbols represent measurements during heating and open symbols during cooling the sample. Lines are guides to the eye.

Chapter 6

Discussion of the Results

The geometric frustration and partial magnetic order of CePdAl sensitively depend on the nonthermal control parameters pressure, disorder and magnetic field. Pressure can be either generated by applying an external, uniaxial or hydrostatic finite stress or by an isovalent substitution. As we have seen in $CePd_{1-x}Ni_xAl$, the latter can give rise to chemical site disorder that considerably affects the material properties in a wide temperature and field range where the frustrated antiferromagnetic correlations are present. This disorder hinders the system to reach a thermal equilibrium and should lead to the freezing of magnetic entropy at $T \to 0$. Even if a QCP could be reached in this case, the genuine quantum critical behavior would be compromised by strongly history-dependent effects. The constraints of geometric frustration, on the other hand, can be removed by applying a magnetic field. This is, however, inevitably accompanied by the simultaneous destruction of the magnetic order. In fact, the quantum phase transitions that can be reached in a partial frustrated system by pressure and field are conceptually different. Three principally different scenarios are conceivable:

1. The application of stress breaks the crystal symmetry and thereby lifts the frustration between the competing AF interactions. In this case the QCP would separate a magnetically ordered from a frustrated ground state.

2. If, during the application of pressure, the crystal symmetry is preserved, the pressure will mainly alter the balance between Kondo and RKKY interaction. The QCP would be located between a partially ordered and a paramagnetic ground state in which the magnetic moments have been "switched off" by the Kondo screening.

3. Finally, if a magnetic field is applied, the Kondo effect, AF order and frustration would ultimately be suppressed by forcing the moments to align parallel to the field direction. The QCP would then be between a magnetically ordered and a field-polarized ground state. This scenario can only happen if Kondo effect and frustration prevail in the field range where AF order is being suppressed.

In order to distinguish between these three possible scenarios we want to study the impact of the different control parameters on the low-temperature properties of CePdAl.

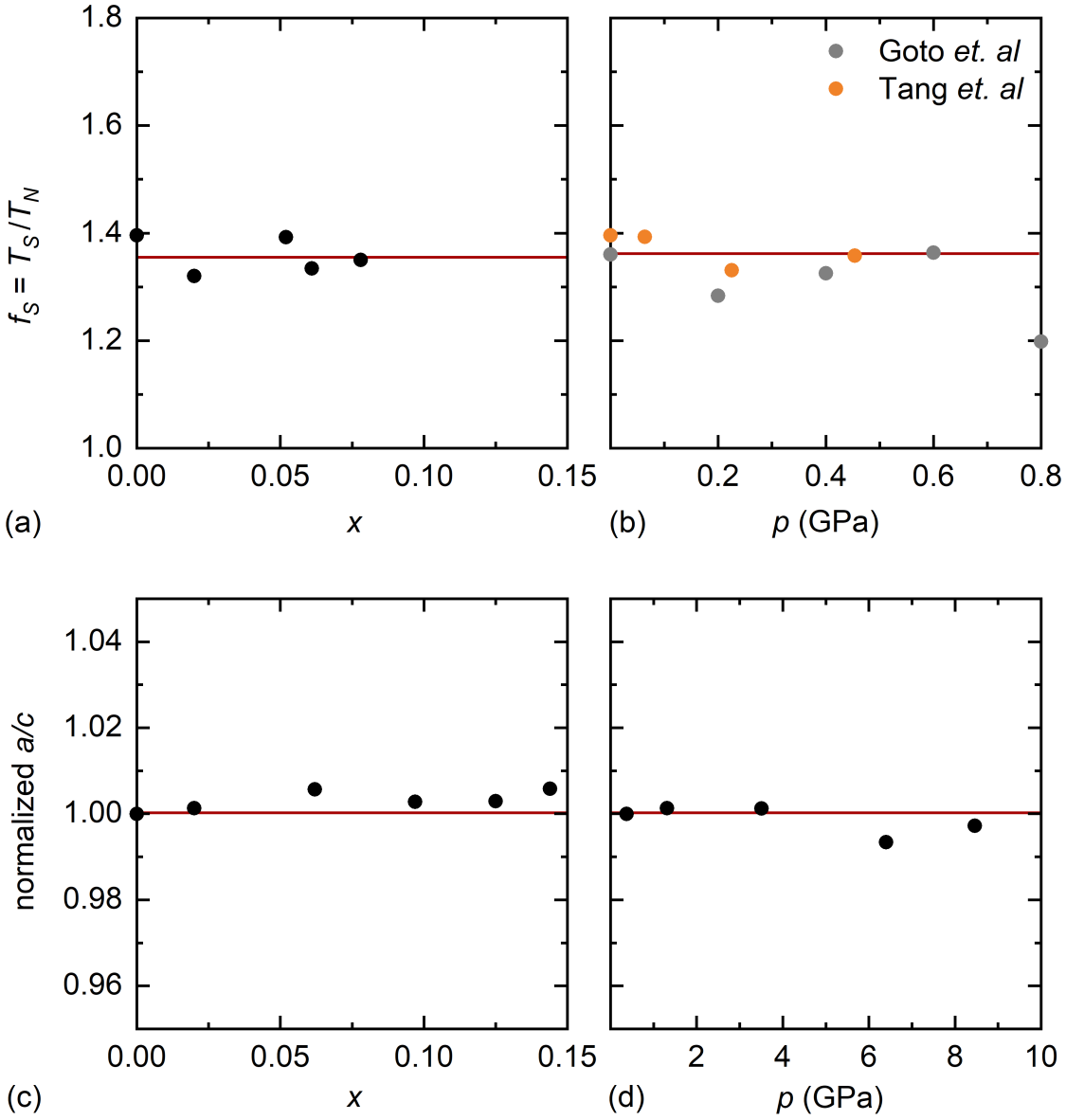

Figure 6.1: (a) and (b) show the evolution of the frustration parameter $f_S = T_S/T_N$ in dependence of chemical (a) and hydrostatic (b) pressure. The pressure data in (b) are taken from Goto *et. al* [35] (grey circles) and Tang *et. al* [34] (orange circles).
(c) and (d) show the evolution of the normalized ratio between the a and the c lattice parameter (data taken from [37, 38]).

6.1 Hydrostatic and Chemical Pressure Dependence of the Frustration

To clarify to which extent the partial geometric frustration is controlled by hydrostatic or chemical pressure we estimated the frustration parameter $f_S = T_S/T_N$ introduced above. For this we used former magnetization, specific heat and resistivity measurements on samples substituted with Ni [37] and under hydrostatic pressure [34, 35]. To complement the data additional magnetization measurements have been carried out under hydrostatic pressure by C.-L. Huang (Rice University, Houston) [57] and under ambient pressure on a $x = 0.05$ sample. In fig. 6.1(a) and (b), f_S is displayed as a function of the Ni concentration x and hydrostatic pressure p, respectively. Up to at least $x \approx 0.08$ and $p = 0.6\,\mathrm{GPa}$, f_S remains unchanged within the experimental error. This, indeed, might have been expected because neither hydrostatic pressure nor the substitution with Ni do change the crystal structure of CePdAl [see chapter 5 and [34]] and even the ratios between the c and a axes remain roughly constant [see fig. 6.1(c) and (d)]. As neither hydrostatic nor chemical pressure do lift the geometric frustration in CePdAl, the unconventional type of partial magnetic order in $CePd_{1-x}Ni_xAl$ persists up to $x = 0.14$ [27]. Consequently, the pressure-induced QCP that we might access in our experiments at zero magnetic field is that of the second scenario in which the Kondo screening suppresses the magnetic order. In fact, the presence of an increasingly strong Kondo effect in $CePd_{1-x}Ni_xAl$ was demonstrated by the diminishing size of the ordered moments for $x \to 0.14$ [27] and was suggested earlier by measurements on poly crystalline $CePd_{1-x}Ni_xAl$ [17]

6.2 The Pressure Dependent Accumulation of Entropy at $x = 0.14$

By tuning a system through a QCP with pressure, the p dependence of S should first increase and then change its sign when the entropy maximum at the QCP is passed. To look for such a behavior the linear thermal-expansion coefficients at zero-magnetic field of all investigated samples are plotted against the temperature in fig. 6.2. With increasing Ni concentration, the Néel temperature clearly moves to lower temperature and at low, constant T, the absolute values of α_a/T and α_c/T increase up to $x \approx 0.10$. At further increased x, α_c/T and consequently $\partial S/\partial \sigma_c$ change their sign between $x = 0.1$ and 0.14, as expected for a pressure-induced QCP. For the stress along the a direction, however, no such indication for a QCP can be found, α_a/T remains positive in the entire studied x range. A possible explanation for this behavior is that with $x = 0.14$ the QCP has not yet been reached and the low-temperature anomalies of α_a/T and α_c/T are due to the phase transition to the AF phase.

Independent of the exact position of the QCP, all measurements on Ni substituted samples reveal strongly broadened transitions. This broadening affects the entropy at constant T as a function of x. Usually, the maximum of S at a QCP should become sharper with decreasing T and the maxima and minima of α_i/T ($\propto -\partial S/\partial\sigma_i$ with $i = a,\ c$) as a function of x should therefore approach the critical x_c of the QCP at low T. In $CePd_{1-x}Ni_xAl$, however, $\alpha_a/T(\alpha_c/T)$ exhibits a maximum(minimum) at $x \approx 0.10$ and $T = 0.1\,\mathrm{K}$ clearly displaced from the QCP at $x_c \geq 0.14$. An obvious origin of the broadening might be found in the chemical site disorder and the sample inhomogeneities.

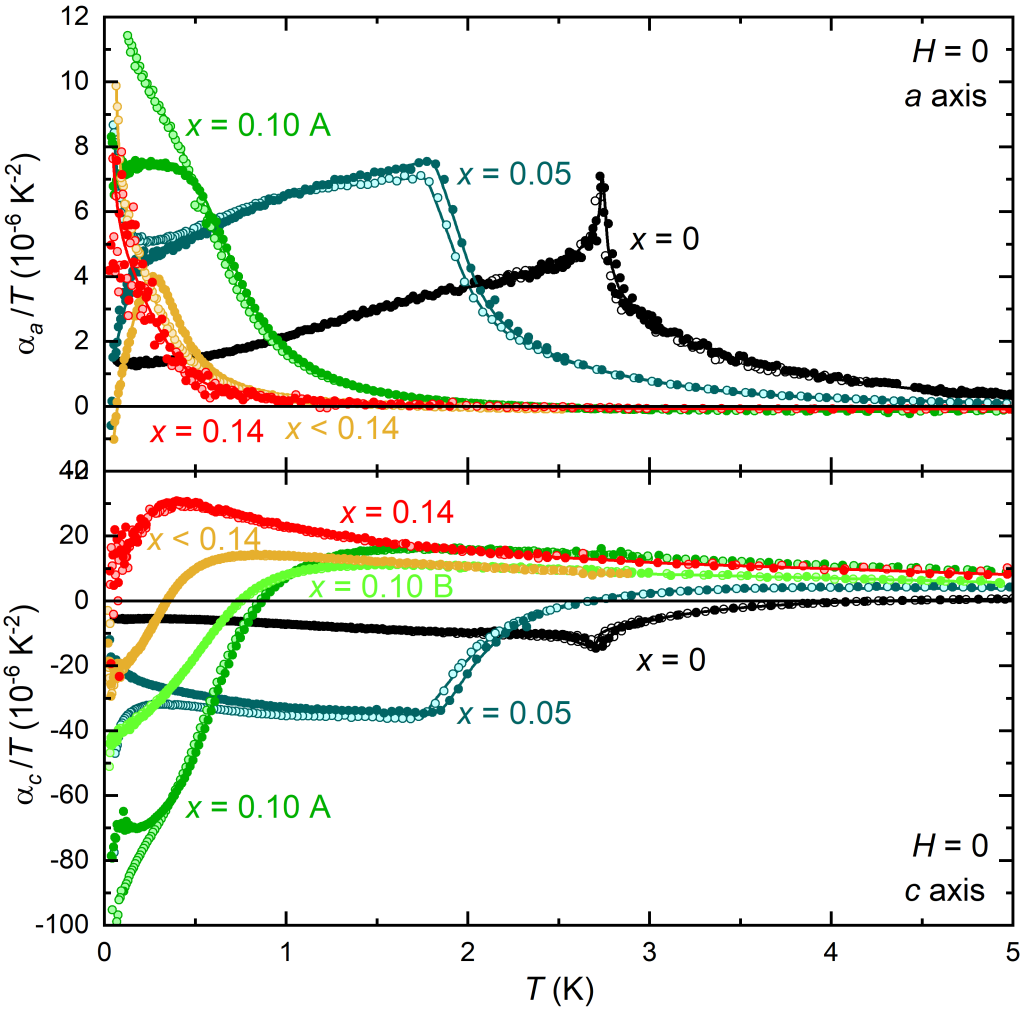

Figure 6.2: Comparison of the temperature dependence of α_a/T (upper panel) and α_c/T (lower panel) for all investigated samples in zero magnetic field.
Full symbols indicate that the temperature was raised during the measurement, open symbol that it was lowered. Lines are guides to the eye.

The volume thermal-expansion coefficients are shown in fig. 6.3. The isotropic, more Kondo-like contribution to the thermal expansion grows with increasing x. The highest values are yielded for the $x = 0.14$ sample. At this Ni concentration, α_V/T apparently diverges with decreasing T which might be interpreted as quantum-critical behavior. Such divergences typical appear when a QCP is approached by temperature. Together with the high, volume-dependent thermal-expansion values this would be inline with the scenario of a Kondo-driven QCP. The downturn below $T \approx 0.5\,\mathrm{K}$ observed for $x = 0.14$ is then a clear sign of the transition into the magnetically ordered state.

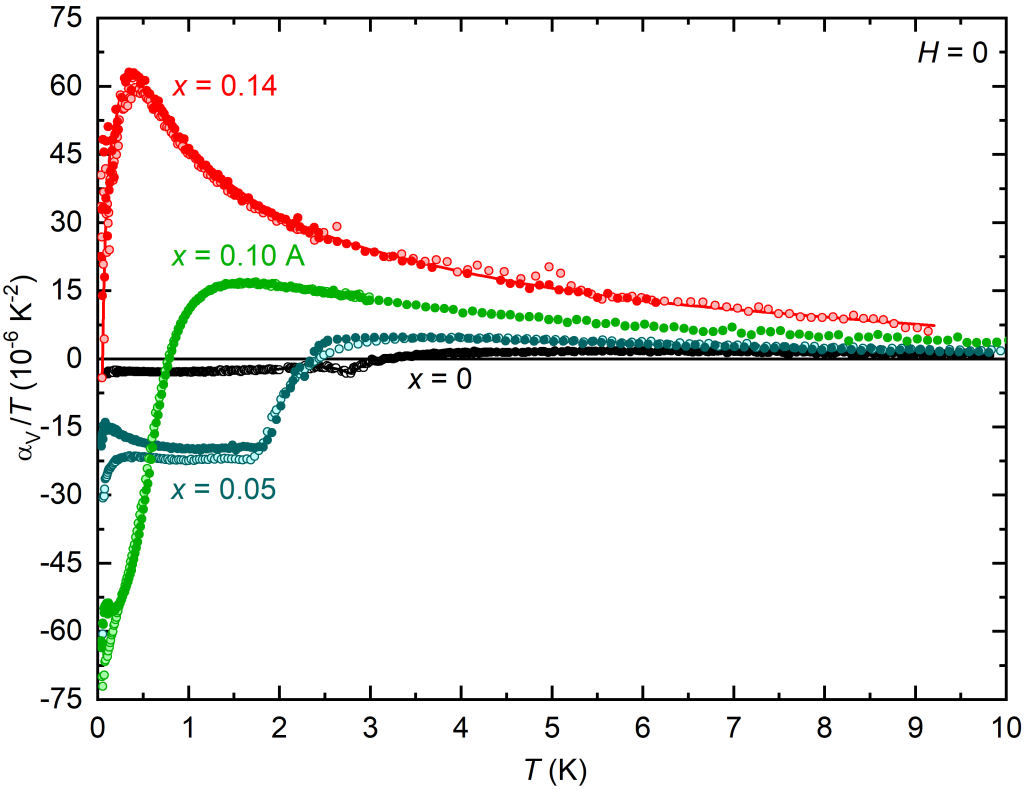

Figure 6.3: Comparison of the temperature dependence of α_V/T for all investigated samples (except $x = 0.10$ B) in zero magnetic field.
Full symbols indicate that the temperature was raised during the measurement, open symbol that it was lowered. Lines are guides to the eye.

6.3 Search for a Pressure-induced Quantum Critical Point

To verify our assumption of such a Kondo-related QCP we now want to compare the Grüneisen ratios of the different samples. In fig. 6.4, Γ_{σ_a} and Γ_{σ_c} are shown as a function of T for $0 \leq x \leq 0.14$, together with the used specific heat and thermal-expansion data. Above T_N, the specific heat exhibits the aforementioned, extended tail due to the critical fluctuations [see fig. 6.4(a)]. Surprisingly, neither the absolute values of C_{4f}/T nor the temperature range where the critical fluctuations are observed exhibit a considerable change with increasing x. The main difference between the measurements is just the shift of T_N to lower T with increasing x. While the thermal expansion is mainly determined by the length changes along the c axis, α_a/T becomes very small with increasing. We therefore focus on α_c/T.

The thermal expansion of $CePd_{1-x}Ni_xAl$ at $T > T_N$ shows for small x a behavior different from that of C_{4f}/T [see fig. 6.4(b)]: With increasing x, the absolute values of α_c/T and its temperature dependence strongly increase. At $x = 0.14$, α_c/T exhibits, like C_{4f}/T, an apparent divergence to $T \to 0$, which again points to the strong pressure dependence of a Kondo-driven QCP.

The critical behavior found in C_{4f}/T and α_c/T is in striking contrast to that of the Grüneisen ratios depicted in fig. 6.4(c). As mentioned above, a temperature dependence of the Grüneisen ratio only shows up if either another underlying interaction with a different E^* begins to dominate the system, or if the characteristic energy scale itself is going to zero because the system enters the quantum-critical regime of a QCP. Therefore, we would expect constant Γ_{σ_a} and Γ_{σ_c} values below T_N, since here long-range order is established, and strong divergences above T_N, because here the T dependence of C_{4f}/T and α_c/T point to a nearby QCP. In sharp contrast, we see, however, in the ordered phase a strong temperature dependence of Γ_{σ_a} and Γ_{σ_c}, which has some resemblance to quantum-critical behavior, and outside the antiferromagnetic order, above T_N, nearly constant Grüneisen ratios, typical for a Fermi liquid far away from a QCP. The contrasting behavior is especially well illustrated by the measurements close to the assumed QCP at $x = 0.14$: C_{4f}/T and α_i/T (with $i = a, b$) reveal both strong divergences while Γ_{σ_i} is temperature independent. In conclusion, both C_{4f}/T and α_i/T indicate the proximity to a QCP but according to Γ_{σ_i} the underlying energy scale does not vanish under pressure with $T \to 0$. The resolution of this apparent dichotom needs further investigation.

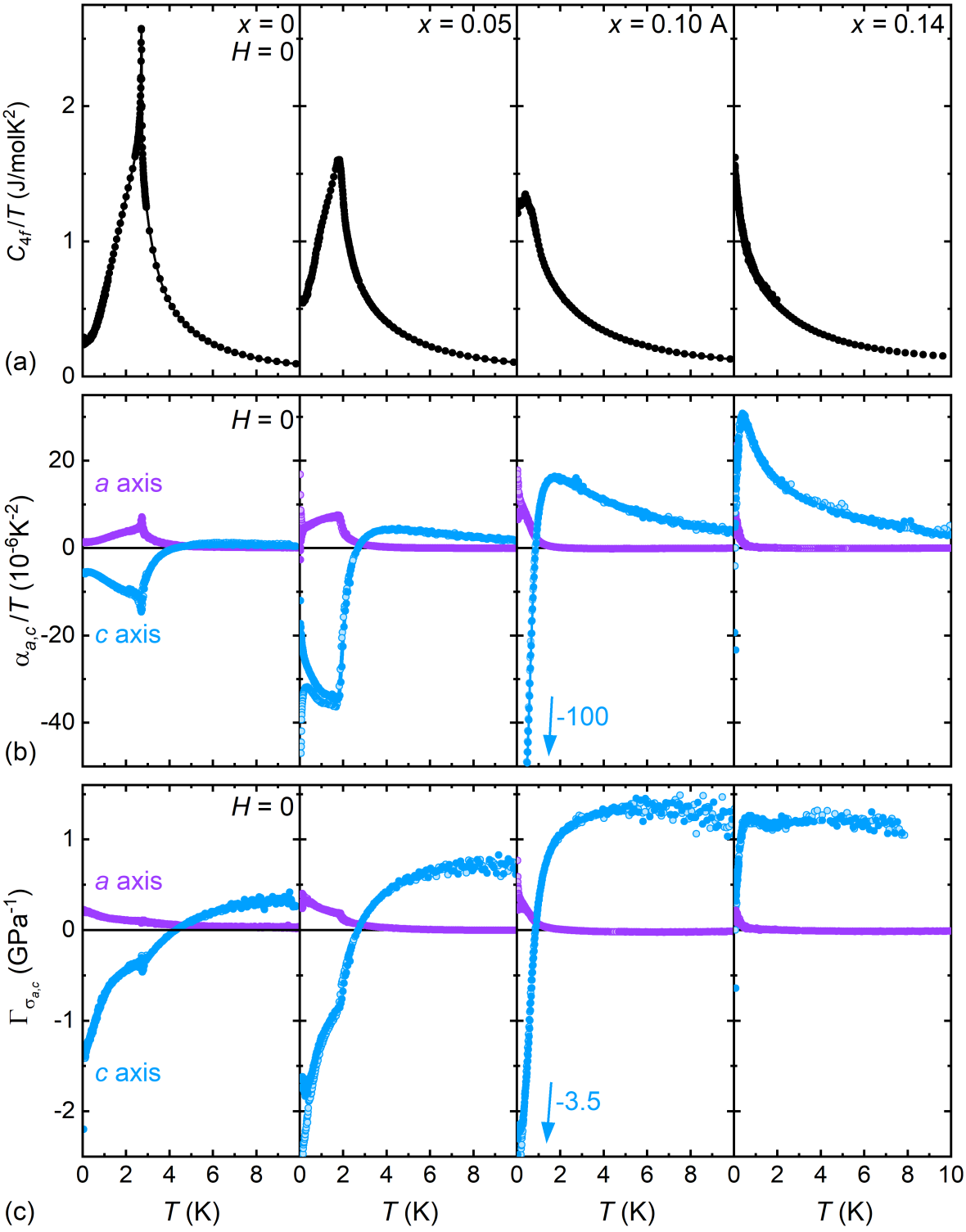

Figure 6.4: Comparison of the change in the criticality for increasing Ni content from left ($x = 0$) to right ($x = 0.14$) at zero field. Row (a) shows the evolution of the specific-heat coefficient C_{4f}/T, row (b) of the linear thermal-expansion coefficients $\alpha_{a,c}/T$ and row (c) of the respective Grüneisen ratios $\Gamma_{\sigma_{a,c}}$.
Full symbols indicate measurements during heating, open symbols during cooling the sample. Lines are guides to the eye.
The specific-heat data are taken from [37]

6.4 The Critical Fields

By suppressing the partial antiferromagnetic order upon applying a magnetic field we can reach the field-induced quantum phase transitions of the third scenario proposed above. We have, however, to account for the nature of the related phase transitions. In CePdAl, the discontinuous phase transition at the critical field H_{c3} will cut off the critical fluctuations. Consequently, hardly any quantum-critical behavior is to be expected. To identify the nature and position of the field-induced transitions at low temperature, the magnetostriction and thermal expansion along both axes are plotted against the magnetic field in fig. 6.5 and fig. 6.6, respectively. A first-order transition should result in a sharp peak. It can, however, be broadened due to disorder or sample inhomogeneities. The data show that low Ni concentrations of $x = 0.10$ are sufficient to completely wash out the peaks. From this one might conclude that the onset of magnetic order is continuous at H_c for $x > 0.05$.

If the frustration is neglected, the position of H_c can be extracted from the change of the anisotropic stress dependences of the entropy and magnetization because they are specific to the underlying characteristic energy scales. The magnetostriction of all samples apart from $x = 0.14$ reveal field-dependent sign changes of λ_c while λ_a remains positive. In the following we will take that feature as indication of a change of the anisotropy of $\partial M/\partial\sigma_i$ (with $i = a$, c). For $x = 0$ and 0.05, the fields of the sign changes of λ_c perfectly agree with those of α_c/T [see fig. 6.6] and with the critical fields found in magnetization and magnetoresistance measurements [18, 58]. At $x = 0.10$, however, the sign change of λ_c occurs with $\approx 2.5\,\mathrm{T}$ at clearly higher fields than that of α_c/T at $\approx 1.5\,\mathrm{T}$. At this low field, however, λ_a is still proportional to λ_c. This mismatch might either point to several, different characteristic energy scales or again to sample inhomogeneities. In the sample with $x = 0.14$ no sign change of λ_c shows up and that of λ_a occurs at too high fields. The smooth anisotropy changes at $\mu_0 H < 3\,\mathrm{T}$ can hardly be attributed to a phase transition, but a transition might occur below the temperature of the depicted magnetostriction measurements.

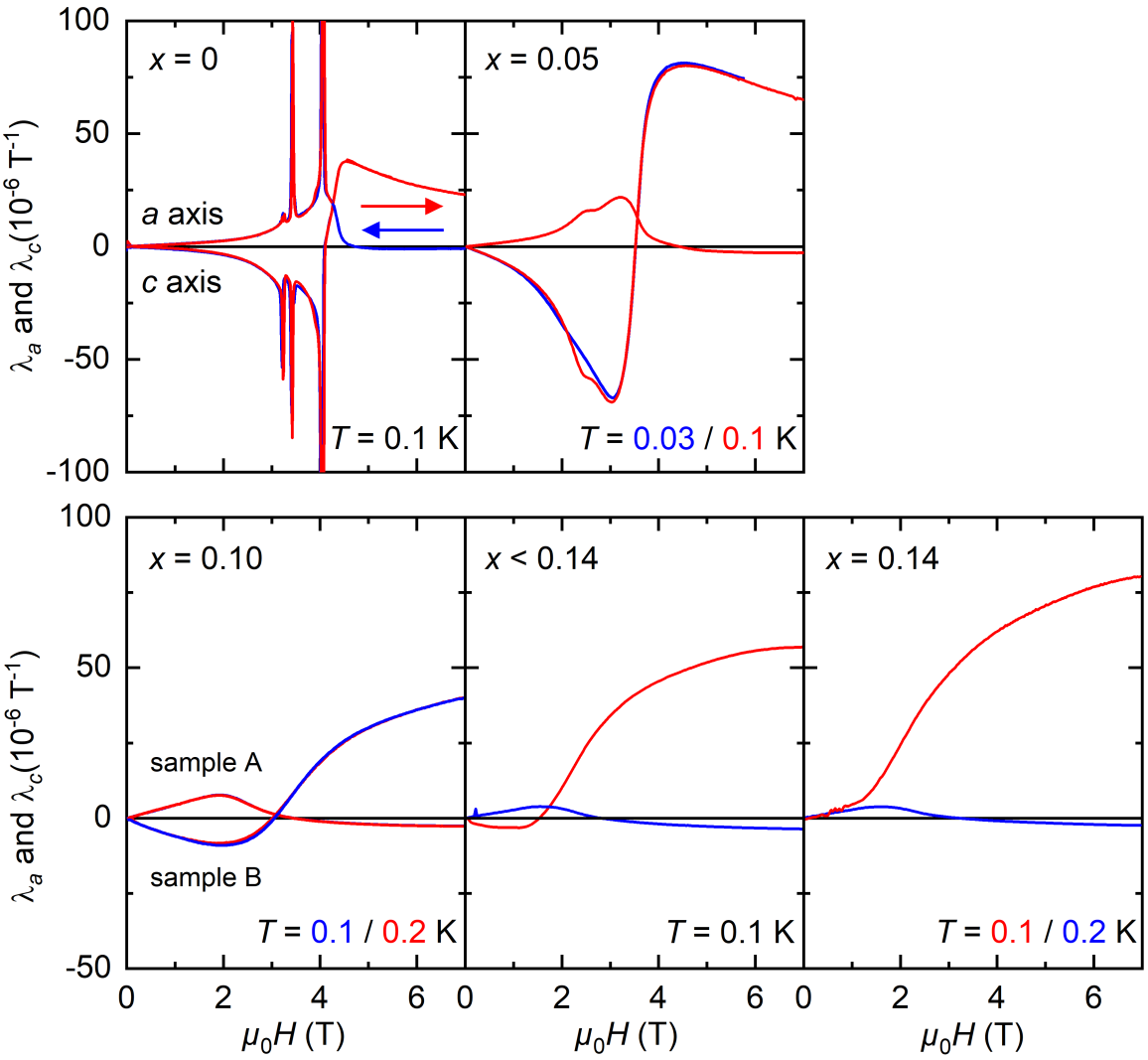

Figure 6.5: Evolution with increasing Ni content of the magnetic field dependence of the magnetostriction coefficients λ_a and λ_c along the a and c axis, respectively, for field applied in c direction at constant lowest temperatures. Red data are measured with increasing and blue data with decreasing magnetic field.

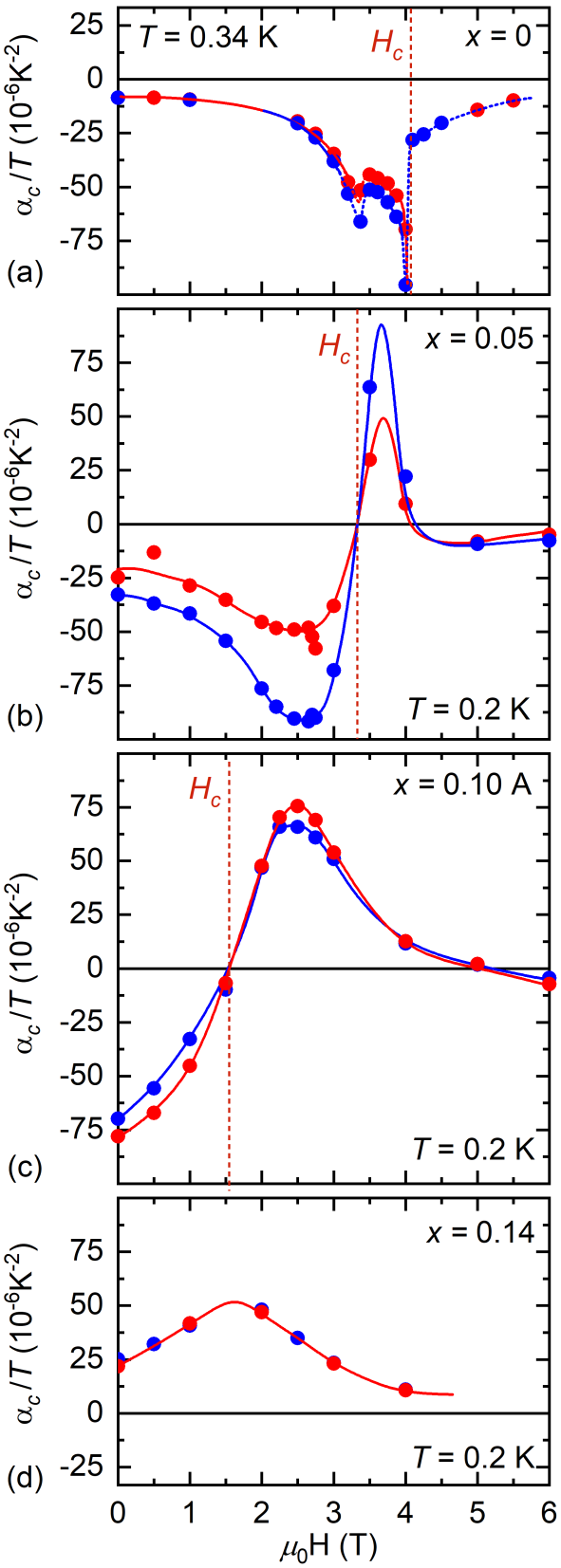

Figure 6.6: Field dependence of α_c/T in fields along the c direction up to $\mu_0 H = 6\,\mathrm{T}$. Data for $x = 0$ (in (a)) was taken at $T = 0.34\,\mathrm{K}$, data for $x = 0.05$, $x = 0.10$ A and $x = 0.14$ ((b), (c) and (d) respectively) at $T = 0.2\,\mathrm{K}$. The red dashed line gives the approximate critical field H_c. Red symbols indicate measurements during heating, blue symbols during cooling the sample. Lines are guides to the eye.

6.5 The Pressure-dependent Accumulation of Entropy at the Critical Fields

Similar to the thermal expansion at different x, α_a/T and α_c/T as a function of the magnetic field exhibit sign-changes due to the pressure dependence of the critical field H_c. Examples for this have been discussed above and are additionally given for α_c/T in fig. 6.6. They point to a field- and pressure-dependent maximum of S at $H \approx H_c$. From all measurements shown in fig. 6.6, only the $x = 0.05$ and 0.10 A samples show the S-shaped curves expected for quantum-critical behavior. In $x = 0$ the first-order transition at $H_c = H_{c3}$ presumably cuts off the critical fluctuations and in $x = 0.14$ the sign-change is not visible, probably, because the Néel temperature is below the temperature of the experiment. The measurements show that the critical fields decrease with growing x. The position of the minima at H_- ($< H_c$) and maxima at H_+ ($> H_c$) of α_c/T with respect to the sign change at $\approx H_c$ are related to the width of the field-dependent S accumulation [see also fig. 3 in reference [37]]. With increasing x, $|H_+ - H_c|$ and the broadening of the $S(H)$ peak grow considerably, most probably due to the increasing chemical site disorder. In addition, the differences between field-cooled and field-heated measurements are strongly enhanced at $x = 0.05$ but decline and vanish at $x \to 0.14$ [see fig. 6.6]. According to the X-ray structure investigation, however, an inhomogeneous Ni distribution is also present at high Ni concentrations. As the hystereses predominantly cover the temperature and field range of the AF phase, these history-dependent effects have to be related to the frustration in the partially ordered state. The magnetic unit cell of CePdAl consists of six crystallographic unit cells (neglecting the small deviation from commensurability of $\tau = 1/3$ along the c-direction) and contains 18 formula units. For the two extreme cases CePdAl and CeNiAl, with just a single element species at the Pd or Ni site, no hysteresis is expected. Experimentally we find the largest hysteresis effects in the $x = 0.05$ sample. For this x value the probability to find at least one Ni ion in the magnetic unit cell is $w \approx 60\,\%$. Indeed, this value is close to the theoretical probability of $w = 50\,\%$ of maximum disorder. As $x \to 0.14$ ($w \approx 93\,\%$) nearly each magnetic unit cell contains at least one Ni ion and large differences in the Ce environments will be averaged out. This explains the lack of hysteresis effects in the quantum critical system.

In conclusion, the field-induced quantum criticality of the $x = 0.05$ and $x = 0.10$ samples has to be taken with caution as their low-temperature behavior might be strongly affected by the hystereses.

6.6 Field-induced Quantum Critical Points

Figure 6.7 shows the evolution of the field-induced criticality in $CePd_{1-x}Ni_xAl$ with increasing x at the fields H_+ where $\alpha_c/T(H)$ becomes maximal, slightly above the respective critical H_c. Close to the critical field, the specific heat grows continuously with decreasing T for all Ni concentrations shown in fig. 6.7(a). In fact, the three displayed C_{4f}/T measurements have an apparent resemblance to each other. The only differences are a slight decrease of the absolute values with increasing x and a downturn of the $x = 0$ data at $T < 0.5\,\mathrm{K}$.

The linear thermal-expansion coefficients divided by T exhibit likewise a divergent increase to lower temperatures [see fig. 6.7(b)]. In contrast to C_{4f}/T, however, the increase is becoming more pronounced at higher Ni contents. Compared to the behavior at zero magnetic field, α_a/T has the opposite sign of α_c/T and no traces of the magnetic phase transitions can be observed. The deviations at very low T are attributed to the Schottky anomalies of the Zeeman-split ground-state doublet of the Ce ions [18].

At low T, the Grüneisen ratios of the a and c axis follow basically the evolution of α_a/T and α_c/T with an increase to $T \to 0$ [see fig. 6.7(c)]. Together with the divergent behavior observed in C_{4f}/T, α_a/T and α_c/T, this might be interpreted as quantum-critical behavior although the covered temperature range is comparatively small and Γ_{σ_a} and Γ_{σ_c} quickly reach the constant values observed at zero magnetic field. With regard to the three QCP scenarios introduced above, these field-induced QCPs seem to represent the third scenario where the partial order transits to field-polarized state. There are, however, some significant deviations from this scenario: Apart from the strong history-dependent effects, the critical behavior at H_c grows with x, although the magnetic order gets suppressed and H_c decreases. Even more striking, the $x = 0.14$ sample does not show the divergence at H_c. This would be at much smaller fields if the ordered state exists at all at this Ni content. At lower fields, on the other hand, no signature of quantum criticality shows up in $x = 0.14$.

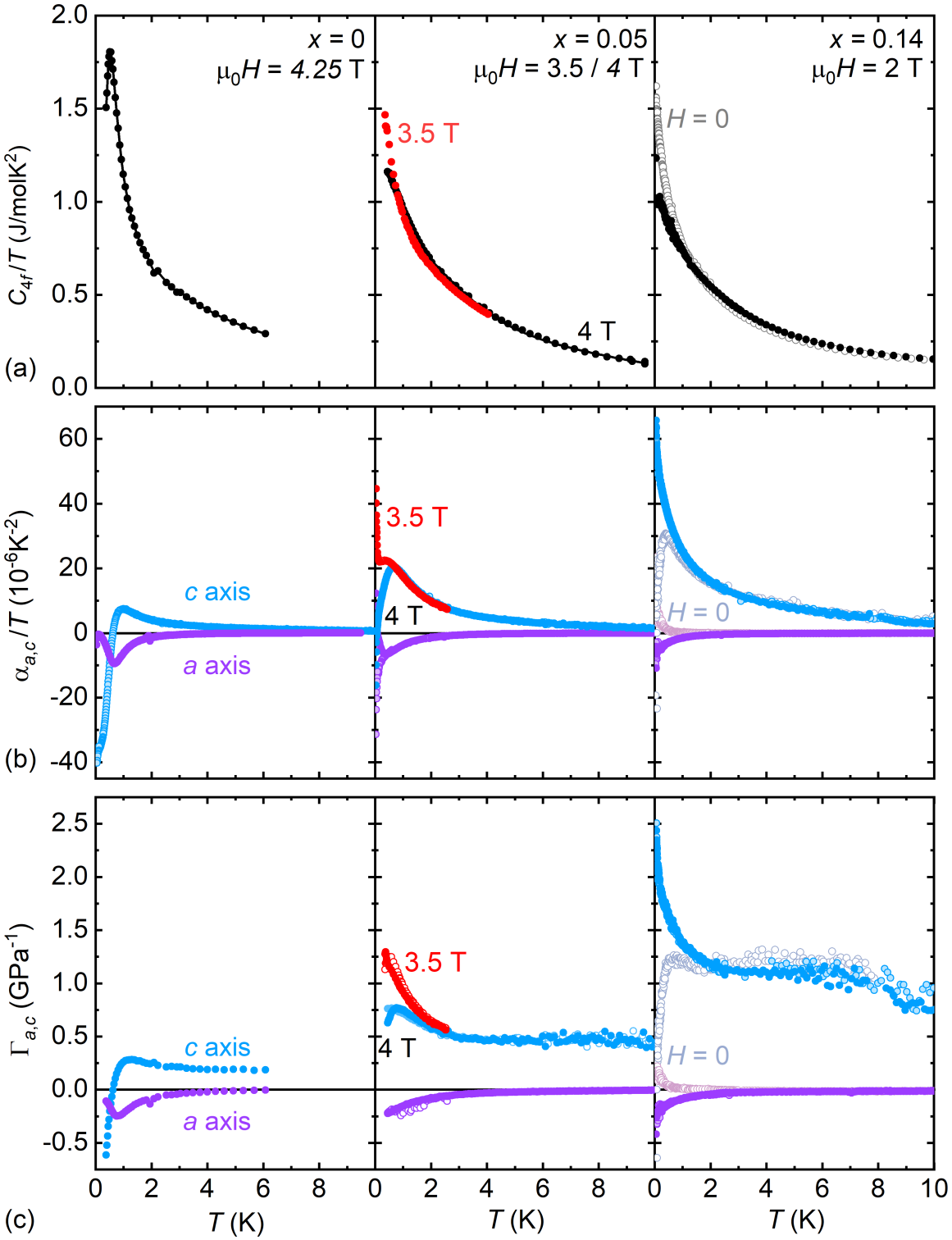

Figure 6.7: Comparsion of the change in the criticality for increasing Ni content ($x = 0$, $x = 0.05$ and $x = 0.14$) at the maximum of $\alpha_c/T(\mu_0 H)$ slightly above the respective critical field (bright, open symbols for $x = 0.14$ at $H = 0$ for comparison). Row (a) shows the evolution of the specific-heat coefficient C_{4f}/T, row (b) of the linear thermal-expansion coefficients $\alpha_{a,c}/T$ and row (c) of the respective Grüneisen ratios $\Gamma_{a,c}$.
Full symbols indicate measurements during heating, open symbols during cooling the sample. Lines are guides to the eye. The specific-heat data are taken from [37].

Chapter 7

Conclusions

The main theme of this work was to shed light and resolve the apparent contradictions between the critical behavior found in the thermal expansion, specific heat, and Grüneisen ratios of $CePd_{1-x}Ni_xAl$. The main issues concern the behavior of these basic thermodynamic properties at low temperatures and in magnetic fields, in particular the regions where the critical behavior could be found. While the specific heat and thermal expansion reveal critical fluctuations close to the onset of partial long-range order at $x = 0.14$, the Grüneisen ratio displays a non-critical standard Fermi-liquid state. On the other hand, within the magnetically ordered state, C_{4f}/T and α_i/T show an unremarkable T dependence while the Grüneisen ratio uncovers some criticality. In magnetic fields, finally, all quantities concomitantly exhibit quantum-critical behavior, but for $x = 0.14$ they do so in a field range that is far beyond the expected critical field.

Thermal expansion and specific heat are derivatives of the entropy. At $x = 0.14$ they indicate the typical accumulation of S expected in the vicinity of a QCP which is driven by pressure or magnetic field. The Grüneisen ratio, on the other hand, reveals the stress dependence of the characteristic energy scale of the system. The fact that it remains constant demonstrates that this energy scale cannot be altered by pressure in our experiment. As mentioned above, the thermal expansion is unable to break the crystal symmetry. It is therefore not surprising that in our experiment the frustration remains unaffected and therefore its characteristic energy scale does not change.

Within the antiferromagnetic order, on the other hand, the situation is quite different because, in contrast to the frustration, the AF order sensitively depends on pressure, even if that pressure does not break the crystal symmetry. Is is for this reason that, the Néel temperature can be suppressed by hydrostatic pressure or substitution with Ni. In the partially ordered state the AF order competes with the geometric frustration. The frustration is changed by the pressure dependent magnetic order and the critical behavior of the characteristic energy becomes visible. This criticality cannot be ob-

served in the specific heat and thermal expansion simply because the entropy vanishes due to the evolution of the long-range magnetic order.

Finally, at the field-induced QCPs (at $x \geq 0.05$), the thermal expansion and specific-heat data indicate a field- and pressure-dependent accumulation of entropy. Here, the frustration competes with the AF order, the Kondo effect, and the field polarization of the magnetic moments. The Kondo effect is particularly sensitive to isotropic stresses that does not break the crystal symmetry. As the Kondo effect and the field polarization suppress the partially frustrated AF order, the underlying characteristic energy scale E^* is tuned to zero in our experiment. Therefore, the quantum criticality appears not only in the specific heat and thermal expansion but also the corresponding pressure-dependent Grüneisen ratio.

In summary $CePd_{1-x}Ni_xAl$ is one of the rare examples of a heavy-fermion compound with geometrical frustration. The system is characterized by a number of unusual properties, in particular, a partially frustrated magnetic order with extended critical fluctuations. Our measurements shed light on the interplay between geometric frustration and the Kondo effect, two different routes to quantum criticality. The results demonstrate that the geometric frustration can only be lifted by stress combinations which break the crystal symmetry. As the thermal expansion does not affect the crystal symmetry, the characteristic energy scale of the frustration is not changed in our experiment. Therefore, the pressure dependence of this energy scale, the Grüneisen ratio, appears to be noncritical, although other thermodynamic quantities indicate the proximity to a quantum critical point. In the partially ordered state, on the other hand, frustration and long-range order compete with each other and the Grüneisen ratio shows the critical change of the frustration due to the pressure dependent antiferromagnetic order. The presented measurements show that a combination of thermodynamic quantities, such as specific heat and thermal expansion, can be used to distinguish between different types of critical behavior. Such combinations are especially suited to study materials which are in the vicinity of multiple quantum critical points.

List of Figures

Bibliography

[1] F.M. Grosche, S.R. Julian, N.D. Mathur, G.G. Lonzarich, *Magnetic and superconducting phases of $CePd_2Si_2$*, Physica B (Amsterdam, NL) **223-224**, 50 (1996).

[2] H.v. Löhneysen, C. Paschke, G. Portisch, M. Ruck, H.G. Schlager, M. Sieck, C. Speck, *Magnetization and specific heat of the new heavy-fermion compound $CeCu_5Au$*, Physica B (Amsterdam, NL) **199-200**, 85 (1994).

[3] J. Kondo, *Resistance Minimum in Dilute Magnetic Alloys*, Prog. Theor. Phys. **32**, 37 (1964).

[4] M. A. Ruderman, C. Kittel, *Indirect Exchange Coupling of Nuclear Magnetic Moments by Conduction Electrons*, Phys. Rev. **96**, 99 (1954).

[5] T. Kasuya, *A Theory of Metallic Ferro- and Antiferromagnetism on Zener's Model*, Prog. Theor. Phys. **16**, 45 (1956).

[6] Kei Yosida, *Magnetic Properties of Cu-Mn Alloys*, Phys. Rev. **106**, 893 (1957).

[7] J. G. Bednorz, K. A. Müller, *Possible high T_c superconductivity in the Ba-La-Cu-O system*, Z. Phys. B **64**, 189 (1986).

[8] Y. Kamihara, T. Watanabe, M. Hirano, H. Hosono, *Iron-Based Layered Superconductor $La[O_{1-x}F_x]FeAs$ (x = 0.05-0.12) with T_c = 26 K*, J. Am. Chem. Soc. **130**, 3296 (2008).

[9] K. Grube, L. Pintschovius, F. Weber, J.-P. Castellan, S. Zaum, S. Kuntz, P. Schweiss, O. Stockert, S. Bachus, Y. Shimura, V. Fritsch, H. v. Löhneysen, *Magnetic and Structural Quantum Phase Transitions in* $CeCu_{6-x}Au_x$ *are Independent*, Phys. Rev. Lett. **121**, 087203 (2018).

[10] L. Balents, *Spin liquids in frustrated magnets*, Nature **464**, 199 (2010).

[11] P. A. Lee, *An End to the Drought of Quantum Spin Liquids*, Science **321**, 1306 (2008).

[12] John A. Mydosh, *Spin glasses: an experimental introduction* (Taylor & Francis, London, 1993).

[13] S. T. Bramwell, M. J. P. Gingras, *Spin Ice State in Frustrated Magnetic Pyrochlore Materials*, Science **294**, 1495 (2001).

[14] C. Schank, F. Jährling, L. Luo, A. Grauel, C. Wassilew, R. Borth, G. Olesch, C. D. Bredl, C. Geibel, F. Steglich, *4f-conduction electron hybridization in ternary Ce-TM-Al compounds*, J. Alloys Compd. **207-208**, 329 (1994).

[15] H. Kitazawa, A. Matsushita, T. Matsumoto, T. Suzuki, *Electronic and thermal properties of CePdAl*, Physica B (Amsterdam, NL) **199–200**, 28 (1994).

[16] A. Dönni, G. Ehlers, H. Maletta, P. Fischer, H. Kitazawa, M. Zolliker, *Geometrically frustrated magnetic structures of the heavy-fermion compound CePdAl studied by powder neutron diffraction*, J. Phys.: Condens. Matter **8**, 11213 (1996).

[17] V. Fritsch, N. Bagrets, G. Goll, W. Kittler, M. J. Wolf, K. Grube, C.-L. Huang, H. v. Löhneysen, *Approaching quantum criticality in a partially geometrically frustrated heavy-fermion metal*, Phys. Rev. B **89**, 054416 (2014).

[18] S. Lucas, K. Grube, C.-L. Huang, A. Sakai, S. Wunderlich, E. L. Green, J. Wosnitza, V. Fritsch, P. Gegenwart, O. Stockert, H. v. Löhneysen, *Entropy Evolution in the Magnetic Phases of Partially Frustrated CePdAl*, Phys. Rev. Lett. **118**, 107204 (2017).

[19] M. Vojta, *Quantum phase transitions*, Rep. Prog. Phys. **66**, 2069 (2003).

[20] M. Vojta, *Frustration and quantum criticality*, Rep. Prog. Phys. **81**, 064501 (2018).

[21] L. Zhu, M. Garst, A. Rosch, Q. Si, *Universally Diverging Grüneisen Parameter and the Magnetocaloric Effect Close to Quantum Critical Points*, Phys. Rev. Lett. **91**, 066404 (2003).

[22] M. Garst, A. Rosch, *Sign change of the Grüneisen parameter and magnetocaloric effect near quantum critical points*, Phys. Rev. B **72**, 205129 (2005).

[23] A. E. Böhmer, *Competing Phases in Iron-Based Superconductors Studied by High-Resolution Thermal-Expansion and Shear-Modulus Measurements*, Dissertation, Karlsruher Institut für Technologie (KIT), 2014.

[24] S. Doniach, *The Kondo lattice and weak antiferromagnetism*, Physica B+C (Amsterdam) **91**, 231 (1977).

[25] G. H. Wannier, *Antiferromagnetism. The Triangular Ising Net*, Phys. Rev. **79**, 357 (1950).

[26] K. Prokeš, P. Manuel, D.T. Adroja, H. Kitazawa, T. Goto, Y. Isikawa, *Magnetic order in CePdAl single crystal: Effect of magnetic field*, Physica B (Amsterdam, NL) **385–386**, 359 (2006).

[27] Z. Huesges, S. Lucas, S. Wunderlich, F. Yokaichiya, K. Prokeš, K. Schmalzl, M.-H. Lemée-Cailleau, B. Pedersen, V. Fritsch, H. v. Löhneysen, O. Stockert, *Evolution of the partially frustrated magnetic order in* $CePd_{1-x}Ni_xAl$, Phys. Rev. B **96**, 144405 (2017).

[28] A. Oyamada, S. Maegawa, M. Nishiyama, H. Kitazawa, Y. Isikawa, *Ordering mechanism and spin fluctuations in a geometrically frustrated heavy-fermion antiferromagnet on the Kagome-like lattice CePdAl: A* ^{27}Al *NMR study*, Phys. Rev. B **77**, 064432 (2008).

[29] L. Keller, A. Dönni, H. Kitazawa, B. van den Brandt, *Geometrical frustration and incommensurate magnetic ordering in CePdAl: a low-temperature neutron-diffraction study*, Appl. Phys. A **74**, s686 (2002).

[30] Y. Isikawa, T. Mizushima, N. Fukushima, T. Kuwai, J. Sakurai, H. Kitazawa, *Magnetocrystalline Anisotropy of Magnetic Dense-Kondo Compound CePdAl*, J. Phys. Soc. Jpn. **65 Suppl. B**, 117 (1996).

[31] M. Dolore Núñez-Regueiro, C. Lacroix, B. Canals, *Magnetic ordering in the frustrated Kondo lattice compound CePdAl*, Physica C (Amsterdam, NL) **282–287**, 1885 (1997).

[32] H. Zhao, J. Zhang, S. Hu, Y. Isikawa, J. Luo, F. Steglich, P. Sun, *Temperature-field phase diagram of geometrically frustrated CePdAl*, Phys. Rev. B **94**, 235131 (2016).

[33] K. Mochidzuki, Y. Shimizu, A. Kondo, S. Nakamura, S. Kittaka, Y. Kono, T. Sakakibara, Y. Ikeda, Y. Isikawa, K. Kindo, *Thermodynamic Investigation of Metamagnetic Transitions and Partial Disorder in the Quasi-Kagome Kondo Lattice CePdAl*, J. Phys. Soc. Jpn. **86**, 034709 (2017).

[34] J. Tang, A. Matsushita, H. Kitazawa, T. Matsumoto, *High pressure effect on the magnetic transition in heavy fermion systems* $CePd_2Al_3$ *and CePdAl*, Physica B (Amsterdam, NL) **217**, 97 (1996).

[35] T. Goto, S. Hane, K. Umeo, T. Takabatake, Y. Isikawa, *Field-induced magnetic transitions and pressure-induced magnetic instability in CePdAl*, J. Phys. Chem. Solids **63**, 1159 (2002).

[36] K. Prokeš, P. Manuel, D.T. Adroja, H. Kitazawa, T. Goto, Y. Isikawa, *Magnetic order of CePdAl under pressure - neutron diffraction study*, J. Magn. Magn. Mater. **310**, e28 (2007).

[37] A. Sakai, S. Lucas, P. Gegenwart, O. Stockert, H. v. Löhneysen, V. Fritsch, *Signature of frustrated moments in quantum critical* $CePd_{1-x}Ni_xAl$, Phys. Rev. B **94**, 220405 (2016).

[38] V. Fritsch, C.-L. Huang, N. Bagrets, K. Grube, S. Schumann, H. v. Löhneysen, *Magnetization and specific heat of* $CePd_{1-x}Ni_xAl$, Phys. Stat. Soli. B **250**, 506 (2013).

[39] M. Vojta, *From itinerant to local-moment antiferromagnetism in Kondo lattices: Adiabatic continuity versus quantum phase transitions*, Phys. Rev. B **78**, 125109 (2008).

[40] Q. Si, *Quantum criticality and global phase diagram of magnetic heavy fermions*, Phys. Stat. Soli. B **247**, 476 (2010).

[41] P. Coleman, A. H. Nevidomskyy, *Frustration and the Kondo Effect in Heavy Fermion Materials*, J. Low Temp. Phys. **161**, 182 (2010).

[42] K.-S. Kim, C. Pépin, *Thermopower as a signature of quantum criticality in heavy fermions*, Phys. Rev. B **81**, 205108 (2010).

[43] J. F. Nye, *Physical properties of crystals: their representation by tensors and matrices*, *Oxford science publications* (Clarendon Pr., Oxford, 1985).

[44] *Concise encyclopedia of magnetic & superconducting materials*, Hrsg.: Kurt H. J. Buschow (Elsevier, Amsterdam, 2005).

[45] S. Zaum, *Thermische Ausdehnung, Magnetostriktion und Thermokraft von* $CeCoIn_5$ *und* $CeCu_{6-x}Au_x$ *bei sehr tiefen Temperaturen*, Dissertation, Karlsruher Institut für Technologie (KIT), 2011.

[46] E. Grüneisen, *Theorie des festen Zustandes einatomiger Elemente*, Ann. Phys. **344**, 257 (1912).

[47] E. Grüneisen, *Die thermische Ausdehnung regulär kristallisierender fester Körper*, Ann. Phys. **360**, 371 (1918).

[48] P. Gegenwart, *Grüneisen parameter studies on heavy fermion quantum criticality*, Rep. Prog. Phys. **79**, 114502 (2016).

[49] P. Ehrenfest, *Phasenumwandlungen im üblichen und erweiterten Sinn, classifiziert nach den entsprechenden Singularitäten des thermodynamischen Potentiales*, Proc. K. Ned. Akad. Wet. **36**, 153 (1933).

[50] A. B. Pippard, *Elements of classical thermodynamics for advanced students of physics*, repr. ed. (Cambridge Univ. Pr., Cambridge, 1966).

[51] V.Fritsch, S. Lucas, Z. Huesges, A. Sakai, W. Kittler, C. Taubenheim, S. Woitschach, B. Pedersen, K. Grube, B. Schmidt, P. Gegenwart, O. Stockert, H. v. Löhneysen, *CePdAl - a Kondo lattice with partial frustration*, J. Phys.: Conf. Ser. **807**, 032003 (2017).

[52] M. Levy, H. E. Bass, R. R. Stern, V. Keppens, *Handbook of elastic properties of solids, liquids and gases* (Academic Press, San Diego, 2001).

[53] T. Suzuki, H. Higaki, I. Ishii, M.S. Kim, T. Takabatake, *Anomalous temperature dependence of elastic moduli of CeRhSn*, J. Magn. Magn. Mater. **272-276**, E35 (2004).

[54] H. Higaki, I. Ishii, D. Hirata, M.-S. Kim, T. Takabatake, T. Suzuki, *Elastic, Thermal, Magnetic and Transport Properties of Kondo Compounds CeRhIn and CeRhSn*, J. Phys. Soc. Jpn. **75**, 024709 (2006).

[55] K. Persson, Materials Data on CePdAl (SG:189) by Materials Project, 2016, computed materials data using density functional theory calculations. These calculations determine the electronic structure of bulk materials by solving approximations to the Schrödinger equation. For more information, see https://materialsproject.org/docs/calculations.

[56] S. Lucas, private communication, 2018.

[57] C.-L. Huang, private communication, 2018.

[58] Christian Taubenheim, *Spezifischer Widerstand des partiell frustrierten Schwerfermionsystems* $CePd_{1-x}Ni_xAl$, Dissertation, Karlsruher Institut für Technologie (KIT), 2017.